2009

Gold Nanoparticles: Synthesis, Property Study and Applcications for Biomolecular Detection and Photothermal Therapy

Xiong Liu
University of Central Florida

GOLD NANOPARTICLES: SYNTHESIS, PROPERTY STUDY AND APPLCICATIONS FOR BIOMOLECULAR DETECTION AND PHOTOTHERMAL THERAPY

by

XIONG LIU
B.S. University of Science and Technology of China, 2004

A dissertation submitted in partial fulfillment of the requirements
for the degree of Doctor of Philosophy
in the Department of Chemistry
in the College of Science
at the University of Central Florida
Orlando, Florida

Fall Term
2009

Major Professor: Qun Huo

ABSTRACT

This dissertation presents a systematic study on gold nanoparticles: from their chemical synthesis, modification of surface functionalities, optical properties studies with emphasis on the absorption and scattering properties, to applications of gold nanoparticles in biomolecular detection, imaging and photothermal therapy. In chapter 2, we studied the kinetics of gold nanoparticle growth under Brust-Shiffrin reaction conditions. In chapter 3, we further examined the reaction mechanism and growth kinetics of gold nanoparticles using oleylamine as both a reducing reagent and particle growth passivation ligand. From these two projects, important understanding was revealed on gold nanoparticle formation and growth mechanism. Chapter 4 describes the synthesis of a monofunctional gold nanoparticle through a solid phase place exchange reaction. From Chapter 5, we moved to the optical property study of gold nanoparticles, particularly the absorption and scattering phenomenon. In this work a systematic analysis on the extinction coefficient of gold nanoparticles was performed, providing meaningful references for applications based on optical absorption properties of gold nanoparticles. In Chapter 6 and Chapter 7, we developed a one-step homogeneous immunoassay for protein detection and analysis based on the strong light scattering of gold nanoparticles and dynamic light scattering detection technique. In Chapter 8, we further improved the stability of gold nanoparticle bioconjugates using a poly(ethylene glycol)-coated gold nanoparticles and further tested this nanoparticle in the one-step homogeneous immunoassay. Finally in Chapter 9, we demonstrated the application of gold nanoparticles for in vitro bioimaging and photothermal therapy of a lung cancer cell. In summary, this dissertation presents a comprehensive study on the synthesis, surface

modification, property study of gold nanoparticles and their applications in biomolecular imaging and analysis.

ACKNOWLEDGEMENTS

I need to thank many people who helped me through my PhD studies. First, I would like to thank my advisor, Dr. Qun (Treen) Huo for the valuable opportunity to work on the exciting nanoscience and nanotechnology. Dr. Huo not only provided strong support and guidance for my projects, more importantly, she taught me how to become an independent scientist. Her patience, wisdom, and more importantly, her encouragements helped me to overcome many difficulties encountered throughout my study. I appreciate her support and advice from the bottom of my heart.

Second, I would like to express my sincere gratitude to Dr. Joseph P. Brennan and Dr. Lei Zhai, not only for the support they provided to me in our collaboration projects, but also their many insightful discussions and suggestions for my research. I am very lucky to have them as additional mentors throughout my study at UCF.

Next I need to thank many other professors and collaborates who have had an impact on this dissertation: Dr. Tatyana Zhukov for her kind explanation and advise in biochemistry and clinical chemistry; Dr. Stephen M. Kuebler and Dr. Florncio E. Hernandez for their helpful discussions on optical properties of nanoparticles and the Raman Spectroscopy; Dr. Helge Heinrich on the detailed explanation and training on TEM instrument; Dr. Stephen Lambert for his very helpful discussions on immunoassays and biology; and Dr. Andre J. Gesquiere for his kind help on instrument usage.

In the following I have to say thanks to my labmates, colleagues and friends at the North Dakota State University and the University of Central Florida. In particular, Dr. James Worden deserves praises for being a nice and helpful group member who taught me the synthesis of gold nanoparticles hand-by-hand and many other important lab skills. I appreciate the tremendous help from Dr. Jinhai Wang and Dr. Jianhua Zou on software,

data processing and analysis, as well as being lifetime friends of mine. Other labmates, including Dr. Hui Chen, Dr. Qiu Dai, Mr. Muthuraman Harish, Mark Atwater, Lauren Austin, Janelle Coutts, Genevieve Knowles, and Jackie are all acknowledged for their help and participation in my research. I also appreciate the help from my collaborators Dr. Mark C Lloyd, Inna V Fedorenko and Priya Bapat from the H. Lee Moffitt Cancer Center in Tampa on discussions of cell incubation and microscopy operation.

Finally, I would like to thank my dear wife, Shanshan Cao, and my family for all the love and support they have provided me. Shanshan loves and supports me all the time. My deceased great grandfather taught me invaluable lessons on how to be a good person. My grand parents and my parents gave me lessons about the world and my brother always encourages me to achieve more in science and technology. Only with their supports I can make this dissertation possible.

TABLE OF CONTENTS

LIST OF FIGURES

LIST OF TABLES

LIST OF SCHEMES

LIST OF ABBREVIATIONS

µM	micro molar (10^{-6} mol/L)
BSA	Bovine Serum Albumin
$_{Bt}GNP_{COOH}$	Mono carboxyl group functionalized butanthiol protected gold nanoparticle
$_{Bt}GNPs$	Butathiol protected gold nanoparticles
CA125	Cancer antigen 125
CAB	Capture antibody
C_{abs}	Absorption cross section
$_{Ci}GNPs$	Citrate protected gold nanoparticles
COOH-PEG-SH	Thiolated poly(ethylene glycol) with a single carboxyl group
C_{sca}	Scattering cross section
CTAB	Cetyltrimethyl ammonium bromide
CV	Coefficient of Variation
D	Diameter of nanoparticles
DAB	Detector antibody
DDA	Discrete Dipole Approximation
D_h	Hydrodynamic diameter
DI	Diionized
DLS	Dynamic Light Scattering
DMF	Dimethylformamide
DNA	Deoxynuleic Acids
$_{Dt}GNPs$	Decanethiol protected gold nanoparticles
EDA	Ethylenediamine
EDC	1-Ethyl-3-(3-Dimethylaminopropyl) Carbodiimide
EGFR	Epithelial Growth Factor Receptor
EGFR	Epithelial Growth Factor Receptor
ELISA	Enzyme Linked Immunosorbent Assay
Fab	Fragment antigen binding region
Fc	Fragment crystallizable region
FDA	United States Food and Drug Administration
fM	Femto molar (10^{-15} mol/L)
FMOC	Fluorenylmethyloxycarbonyl
f-PSA	Prostate Specific Antigen, unbound form
GFAAS	Graphite furnace atomic absorption spectroscopy
GNP	Gold nanoparticle
GNP-anti-IgG	Goat anti-mouse IgG (H+L) (AH) antibody conjugated gold nanoparticles
GNP-IgG	Mouse IgG conjugated gold nanoparticles
GNP-STV	Streptavidin conjugated gold nanoparticles
GNR	Gold nanorod
GPC	Gel Permission Chromatography
$HAuCl_4$	Hydrogen tetrachloroaurate(III) hydrate
HRTEM	High Resolution Transmission Electron Microscopy
IgG	Immunoglobulin

LIA	Laser light scattering immunoassay
LLOD	Lower Limit of Detection
MWCO	Molecular cutoff
N_A	Avogadro's constant
NaCl	Sodium chloride
ng/mL	Nano gram per milliliter
NHS	N-hydroxysulfosuccinimide
NIH	National Institutes of Health
NIR	Near infrared
nM	Nano molar (10^{-9} mol/L)
$_{OA}$GNPs	Oleylamine protected gold nanoparticles
^{o}C	Degree Celsius
PBS	Phosphate Buffer Saline
PCR	Polymerase Chain Reaction
PEG	Poly(ethylene glycol)
pM	Pico molar (10^{-12} mol/L)
ppb	Part per billion
PSA	Prostate Specific Antigen
SEM	Scanning Electron Microscopy
SPR	Surface Plasmon Resonance
ssDNA	Single strand dexylnucleic acid
STDEV	Standard deviation
TEM	Transmission Electron Microscopy
TLC	Thin Layer Chromatography
TOAB	Tetraoctylammonium bromide
UV	Ultraviolet
UV-Vis	Ultraviolet to visible
WHO	World Health Organization
XPS	X-Ray Photoelectron Spectroscopy
ε	Extinction coefficient

CHAPTER 1. INTRODUCTION TO GOLD NANOPARTICLES

1.1 Chemical Synthesis of Gold Nanoparticles

Gold nanoparticles (GNPs or AuNPs), also referred as gold colloids, are particles with sizes in nanometer scale, typically between 1 nm and 100 nm.[1] They have metallic gold (0) cores, can be capped by various types of surface ligands such as small molecules or macromolecules, and are different in their shapes. The history of GNPs could trace back to the 4th or 5th century B.C. in Egypt and China, when GNPs were referred to as "soluble gold" and used in antibiotic applications.[2] Around 4th century AD in Europe, the famous Lycurgus Cup, which has GNPs embedded in, was created. This cup appears as green color when irradiated by a white light from outside (reflected lights) but appears to be red when irradiated from inside (transmitted lights) (Figure 1-1).

Figure 1- 1. Lycurgus cup (4th century A.D.) (left: green color when viewed from scattered light; right: red color when viewed from transmitted light) (®Trustees of the British Museum)

In medieval Europe, GNPs were used as a panacea following the flourish of alchemy. Since then, chemical synthesis of GNPs was discussed and significant progresses were made. In 1685, a recipe invented by Andreas Cassius marked the first reliable method to prepare GNPs in solution. In this recipe, GNPs were prepared by dissolving gold in aqua regia followed by the addition of an aqua regia solution of tin. This colorant in glasses, "Purple of Cassius", became very famous in the 17th century. In 1856, Michael Faraday synthesized the first pure sample of colloidal gold by using phosphorous dispersed in ether or carbon disulfide as the reductant to reduce a solution of chloroaurate.[3]

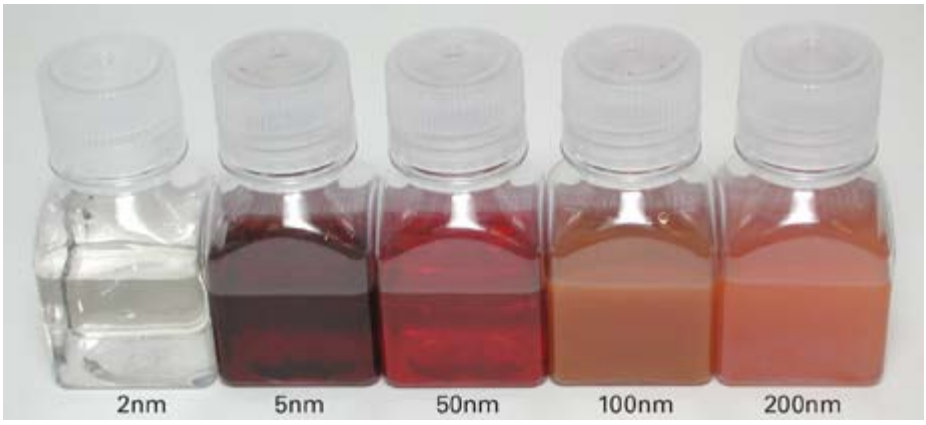

Figure 1- 2. GNPs with different sizes dispersed in water (Ted Pella, Inc.) (®Copyright Ted Pella, Inc.)

In 1951, J. Turkevich pioneered and in 1970s G. Frens refined a very simple method to conveniently synthesize aqueous GNPs.[4] This method uses tri-sodium citrate to reduce $HAuCl_4$ in boiling water and produces nearly mono-dispersed spherical GNPs. These GNPs are negatively charged with a loose layer of citrate anions on the surface. This method can be used to synthesize GNPs with pre-chosen sizes in a broad range from 16 nm up to 200 nm (Figure 1-2). The size versatility is achieved by tuning the relative

ratio of $HAuCl_4$ salt and the reducing agent in the reaction mixture, as well as with careful control over the reaction temperature and the orders of reagents being added to the solution.

Since 1980s, chemical synthesis of GNPs has experienced an exponential growth due to the development of nanoscience and nanotechnology. Novel gold chemistry was discovered such as phosphate-gold, thiol-gold, and amine-gold bonding and interactions. In 1981, Schmid et al. reported the small 1.4 nm $[Au_{55}(PPh_3)_{12}Cl_6]$ gold cluster with a cuboctahdral structure for the Au_{55} gold core. The structure and special quantum electronic properties of these gold culsters were studied extensively.[5] Later on, thiol ligands were found to have a strong affinity with metal gold surface and can help in stabilizing GNPs in both solution and dry states. In 1994, Brust and Schiffrin developed a two-phase reduction process for the synthesis of thiol ligands-protected GNPs. These GNPs were protected with a self-assembled monolayer of thiol molecules and soluble in organic solvents.[6] Since then, various modifications of this reaction were made to synthesize well-dispersed small GNPs in organic solvents.[7] In 1998, Murray et al. conducted a systematic study on this reaction and adapted the initial Brust-Schiffrin reaction to synthesize alkanethoil-protected GNPs with diameters between 1.5 to 5.2 nm. In this two phase synthesis, $AuCl_4^-$ is transferred from aqueous phase into organic phase (toluene) by using a phase transfer agent (tetraoctylammonium bromide). Thiol ligands were dissolved in the organic phase. Following the reduction of the gold anions with aqueous sodium borohydride solution, GNPs were formed in the organic phase. The organic phase changes color from orange to deep brown within a few seconds upon sodium borohydride addition. This approach allows for the convenient synthesis of well

dispersed stable GNPs in organic solvents. Seed-mediated growth method can be used to increase the GNP sizes up to 40 nm.[8] The narrow size distribution of GNPs could be improved by digestive ripening treatments, i.e. heating a colloidal suspension near the boiling point in the presence of excess alkanethiols.[9] Other ligands, such as amines which also have a high affinity with the GNP surface, were reported for the synthesis of GNPs typically with larger sizes than thiolated GNPs. The amine-stabilized GNPs can be either water soluble or organic solvents soluble, providing tunable solubilities for different applications.[10]

In addition to spherical GNPs, there have been tremendous progresses made in the synthesis of non-spherical GNPs. El-Sayed M.A. developed a method for the synthesis of gold nanorods.[11] Xia Y. et al. discovered hollow gold nano-cages.[12] Hallas N. et al. reported a silica-core and gold-shell nanostructure, while Ostafin A.E. et al. developed a gold-core with a silica-shell nanostructure.[13] More recently Hafner J. synthesized star shaped GNPs with interesting optical properties.[14] Although the formation mechanism of these novel structures is not well understood yet, GNPs with tunable size, shape, and surface chemistry can now be synthesized conveniently through a wide range of chemical methods.

1.2 Biomolecular Conjugation of GNPs

To use GNPs for biological applications, GNPs are often conjugated with biomolecules. It is expected that the biomolecule-GNP conjugates remain well dispersed in aqueous solutions, and maintain the intact activity and specificity of biomolecules. There are different approaches available for biomolecular conjugation of GNPs. According to the nature of binding chemistry between the GNP and biomolecules,

methods to prepare biomolecule-GNP conjugates can be classified to be three types: physical adsorption, covalent coupling reactions, and bio-recognition reactions.

The most frequently used method to conjugate antibodies or other type of proteins on GNPs is based on physical adsorption of proteins onto negatively charged citrate-protected GNP surface. This physisorption method was first discovered in 1940s and became widely used to prepare protein-GNP conjugates in biomedical therapies and cell imaging applications since then. Through non-covalent and non-specific interactions, proteins can adsorb onto many inorganic or organic surfaces. Such physisorption of molecules onto a solid support is a result of the combination of weak bonds between biomolecules and the substrate surface. These weak bonds include electrostatic interactions, van der Waals interactions, and/or hydrogen bondings. A classical example of this physisorption effect is the immobilization of proteins on plastic microtiter plate used for Enzyme-Linked ImmunoAbsorbant Assay (ELISA). Protein can absorb onto GNPs through similar interactions.[15]

The advantages of the physisorption method include its simplicity and applicability to almost any type of biomolecules. However, these are several limitations for the physical adsorption method. First, there is a concern about the colloidal stability of biomolecule-conjugated GNPs prepared through the physisorption method. Indeed, bare charged GNPs are not stable and tend to precipitate out in high ionic strength solutions. After GNPs are conjugated with a saturated number of proteins on the surface, the colloidal stability could be significantly improved in high ionic strength solutions such as biological fluids. However, non-specific interaction-induced GNP aggregation can still occur and result in shorter shelf-life and poor reproducibility of the experimental

results. This is the reason why stabilizing agents, such as bovine serum albumin (BSA) or surfactants, are present in most commercial products of GNP-protein conjugate suspensions. Second, there is no control on the orientation of biomolecules which are physically adsorbed onto the GNP surface. Third, the possible denaturation of proteins is also a concern for biomolecule-GNP conjugates prepared through the physisorption method. These limitations of non-covalent physisorption method justify the need of covalent conjugation method for preparing more robust biomolecule-GNP conjugates.

Covalent coupling through gold-thiol chemistry is one of the most extensively used methods for making biomolecule-GNP conjugates. Because thiol groups have high affinity to the GNP surface, when thiol ligands are added into a citrate-protected GNP solution, thiol ligands will replace the citrate molecules on GNPs and lead to thiol ligands-protected GNPs. Through this exchange reaction, thiolated deoxynucleic acid (DNA) molecules could be conjugated covalently onto GNPs. This method was demonstrated in making single strand DNA-conjugated GNPs by Mirkin C.A. et al. and Alivisatos A.P. et al. in 1996.

This thiol exchange reaction method was also used to covalently conjugate proteins or peptides onto GNPs. In this case, a thiolated bi-functional linker molecule is required. The linker molecule is used as the bridge molecule to covalently couple GNPs and biomolecules. The linker molecule has two end groups and a variable part in the middle. The thiol end group on the linker molecule is used to immobilize the linker molecule onto the GNP surface through the thiol exchange reaction. The second end group is used to covalently react with proteins or peptides. Commonly used functional groups are carboxylic acids and amines. The carboxylic acid groups can be activated

through the carbodiimide chemistry and conjugated to the amine groups exposed on the protein surface.[16] Through the linker molecule, proteins and peptides can thus be conjugated covalently to GNPs. As every protein could have several accessible amine groups from lysine residues, this covalent conjugation approach often results in a random and multiple orientation of proteins at the surface of GNPs.

Bioconjugated GNPs prepared through covalent coupling usually have much improved colloidal stability and resistance to non-specific interactions in biological fluids than noncovalently-conjugated GNPs. Another advantage of the covalent coupling method is that the middle part of the linker molecule can be varied to further improve the performance of protein-GNP conjugates. Thiolated poly(ethylene glycol) (PEG) polymers with end groups such as carboxylic groups are excellent linker molecules.[17] The PEG part could serve multiple functions. First, the polymer molecules form a shielding layer on the GNP surface and improve the colloidal dispersion and stability of the bioconjugated-GNPs. Second, the PEG spacer separates biomolecules from the GNP surface so as to avoid or reduce the possible denaturation of proteins. Third, PEG polymer can minimize non-specific interactions between GNPs and biomolecules in biological fluids.[18] Because of these advantages, PEG-protected GNPs have been studied and used extensively for GNP-bioconjugate preparation.[19]

Despite the several advantages of the covalent conjugation method, there are also some problems associated with this method. One problem is the lack of control over the orientation of biomolecules on the GNP surface. Another problem is the possible loss of bioactivity of the biomolecules after their amine groups are used for the covalent bond formation. The amine groups may be important for the bioactivity when they are present

in the active sites or ligand binding sites. These problems can limit the application of the covalent coupling method.

New methods based on bio-recognition reactions have been developed in order to prepare robust biomolecule-GNP conjugates while also to avoid or reduce the above mentioned problems associated with the covalent coupling method. The biotin-streptavidin coupling is an excellent example. Each streptavidin has four biotin binding sites positioned in pairs on opposite domains of the protein. The biotin-streptavidin coupling is known to be the strongest bio-interaction with a binding affinity as high as 10^{15} M^{-1}. To prepared streptavidin-GNP conjugates, thiolated biotin molecules are first covalently attached to GNPs through thiol-gold chemistry. Streptavidin is then added and coupled with biotins on the surface of the GNP through the highly specific and strong biotin-streptavidin interaction.[20]

The streptavidin-conjugated GNPs can be used as a general GNP platform to prepare other protein-GNP conjugates. In such cases, the streptavidin molecules on GNPs are used as anchors to conjugate biotinylated proteins to GNPs. A variety of proteins or peptides could be conjugated to GNPs by this way. Koh et al. prepared the streptavidin-coated GNPs and conjugate them with biotinylated antibodies or biotinylated actin. The conjugation process was monitored by TEM and the proteins around the GNP were imaged by using negative staining technique.[21] Other biomolecules, in addition to streptavidin molecules, could also be used for similar purpose. Brisson A. and Mornet S. used a modified protein of Annexin-A5 as the anchor molecule to conjugate antibodies to GNPs.[22] The modified Annexin-A5 proteins bind only to the crystallizable fragment (Fc region) of antibodies. As a result, antibodies may be conjugated to GNPs with controlled

orientation. The antigen-binding fragments, Fab regions, of the antibodies will be exposed on the GNP surface. The proper orientation of the Fab regions of the antibodies ensures a good bioactivity of the conjugates.

The methods to prepare biomolecule-GNP conjugates through bio-recognition reactions produce conjugates with good colloidal dispersity and stability as well as desired orientation and bioactivity for conjugated biomolecules. However, the process of bio-recognition methods is more complex than the physisorption method or the covalent-coupling method. The advantages as well as the limitations of each conjugation method should be considered in order to select the appropriate method for specific application.

1.3 Optical Properties of GNPs

When one or more dimensions of materials are reduced to the nanometer scale, properties of materials could change dramatically from their bulk states. In the nanometer size range, GNPs present many new interesting properties, especially optical properties.[23-25] When irradiated by lights, the coherent collective oscillation of electrons (6s electrons of the conduction band) on the GNP surface induces large electromagnetic fields, which will resonate with the incident electromagnetic waves at specific frequencies. Such effect has been defined as the well-known Surface Plasmon Resonance (SPR) effect (Figure 1-3).[25b]

The SPR effect results in much enhanced absorption and scattering for GNPs. The absorption and scattering cross sections of GNPs are orders of magnitudes larger than that of non-metallic materials such as polymer latex particles, fluorescent dyes or biomacromolecules. The absorption cross section of GNPs is 4 to 6 orders of magnitudes larger than the strongest absorbing small organic molecules.[23] The scattering cross

section is 4 to 9 orders of magnitudes larger than that of the fluorescence of many widely used organic dyes. These strong absorption and scattering properties make GNPs as ideal probes for biomolecular imaging and detections.[23] As GNPs are not luminescent or not strong luminescent materials, most of the absorbed photon energy will be dissipated into the local environment through heat. In other words, GNPs are excellent photon-thermal energy converters. This property has recently attracted much attention for photothermal therapy applications.

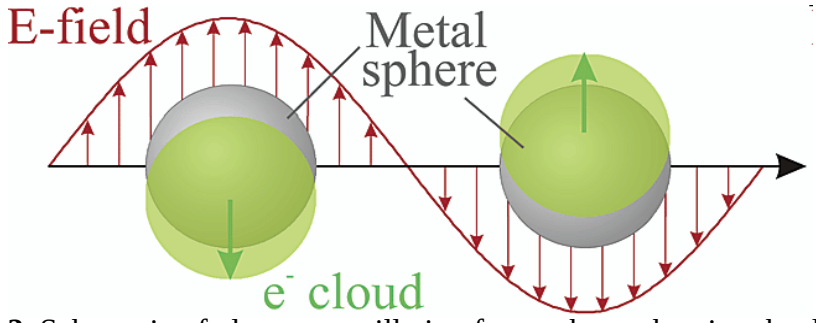

Figure 1- 3. Schematic of plasmon oscillation for a sphere, showing the displacement of the conduction electron charge cloud relative to the nuclei. (Copyrigh ® 2007, Springer New York)

1.3.1 SPR induced absorption property of GNPs

1.3.1.1 SPR absorption of spherical GNPs

Spherical GNPs have a strong SPR absorption band in the visible light region, typical around 520-600 nm (Figure 1-4).[25a] The SPR band of spherical GNPs was first explained by Mie in 1908 and had several derived versions.[24] For particles with sizes much smaller than the wavelength of the incident light (diameter <0.05λ), the absorption cross section (C_{abs}) may be expressed as the following according to Rayleigh scattering theory:

$$C_{abs} = \frac{\pi^2 D^3 n_{med}}{\lambda_0} \mathrm{Im}\left(\frac{m^2 - 1}{m^2 + 1}\right) \tag{1-1}$$

where D is the particle diameter, n_{med} is the refractive index of the surrounding media, λ_0 is the incident light wavelength, and m is the relative refractive index which is defined as the refractive index of the bulk gold at the incident light wavelength λ_0 divided by n_{med}. For visible light irradiation from 400 nm to 800 nm, the absorption of GNPs in sizes up to 20-40 nm in diameter can be described well with equation (1-1). For larger spherical GNPs (diameter >0.05λ), the absorption is dependent on dipole oscillations as well as higher-order multipole oscillations including quadrupole and octopole modes. As a result, the full expression of Mie equation should be used to calculate the absorption cross sections for these large spherical GNPs. [25]

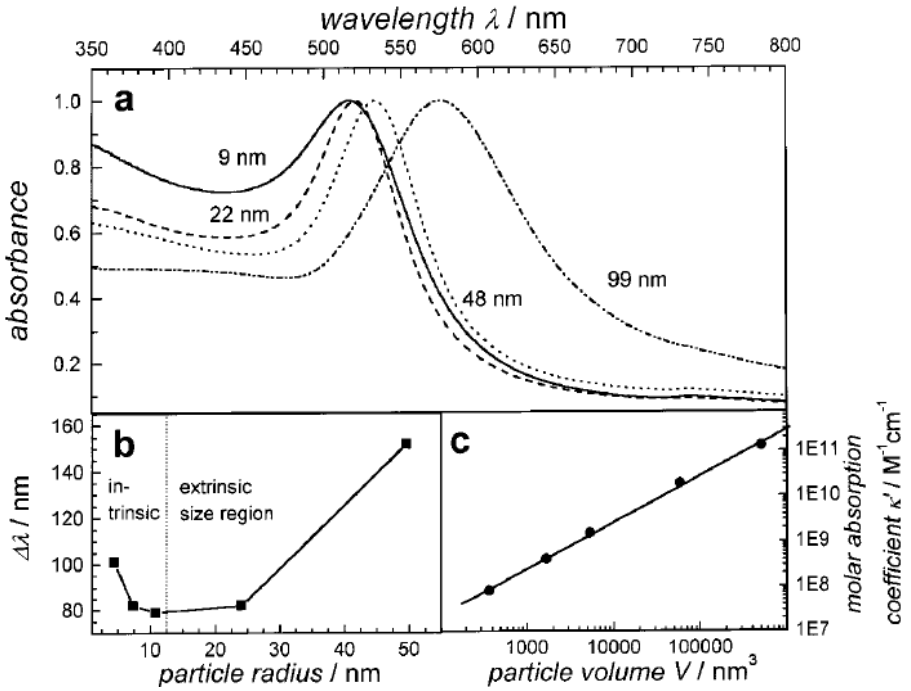

Figure 1- 4. Size effects on the SPR absorption of spherical GNPs. The UV-vis absorption spectra of colloidal GNPs with diameters varying between 9 and 99 nm show that the absorption maximum red-shifts with increasing particle size in part a, while the plasmon bandwidth follows the behavior illustrated in part b. In part c the absorption coefficients of these GNPs at their respective plasmon absorption maxima are plotted

against their volume on a double logarithmic scale. The solid line is a linear fit of the data points. (Copyright ® 1999 American Chemical Society)

According to Mie theory, the peak position, intensity and bandwidth of the SPR absorption band of GNPs are dependent on the size, shape and dielectric constant of GNPs as well as the dielectric constant of the surrounding media. El-Sayed et al. reported the experimental results of the size effect on the SPR absorption band of spherical GNPs (Figure 1-4). When the size of spherical GNPs increases from 9 to 99 nm, the peak wavelength of the absorption band shows a red-shift (Figure 1-4a). In addition, the bandwidth of the SPR band has the minimum at 20 nm and will increase for both smaller and larger GNP (up to 50 nm) (Figure 1-4b). [25,26] In Figure 1-4c, a linear correlation between the molar absorption coefficient and the particle volume is shown. Theses results are in agreement with theoretical calculations based on Mie theory.

Fernig D.G. et al. reported that the SPR absorption spectrum of a monodispersed spherical GNP solution could be used to calculate the size and concentration of the GNPs.[27] The average diameter of GNPs in aqueous solution can be calculated from their UV-Vis absorption spectra:

$$d = \exp(B_1 \frac{A_{spr}}{A_{450}} - B_2) \qquad (1\text{-}2)$$

where A_{spr} is the SPR peak absorbance value of the GNP solution; A_{450} is the absorbance value of the GNP solution at λ=450 nm; B_1=3.00, B_2=2.20 as determined by curve fitting. This equation provides a very convenient way to calculate the diameter of monodispersed GNPs in aqueous solution from 5 to 80 nm. They also derived the following equation to calculate the number density of the GNPs in aqueous solution:

$$N = \frac{A_{450} \times 10^{14}}{d^2[-0.295 + 1.36\exp(-(\frac{d-96.8}{78.2})^2)]} \quad (1\text{-}3)$$

where N is the number density (nanoparticles/mL), A_{450} is the absorbance at λ=450 nm, and d is the particle diameter in nanometer. Based on this equation, one can conveniently estimate the concentrations of GNPs in water.

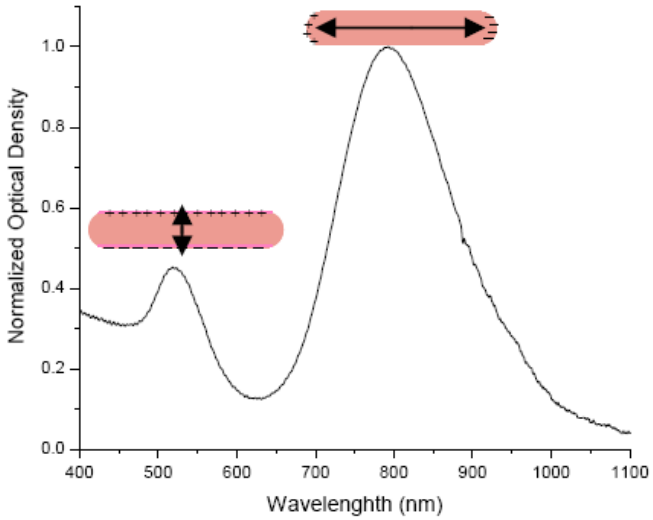

Figure 1- 5. A typical surface plasmon absorption spectrum of gold nanorods. The long wavelength band in the near infrared region around 800 nm is due to the longitudinal oscillation of electrons and the short wavelength band in the visible region around 520 nm is due to the transverse electronic oscillation.

1.3.1.2 SPR absorption of gold nanorods (GNRs)

Non-spherical GNPs have different SPR absorption bands from spherical GNPs. For gold nanorods (GNRs), they have two SPR bands: one weak band peaked at ~530 nm and another strong band peaked at a longer wavelength in the range from 630 to 1100 nm (Figure 1-5).[28] The weak band is due to the transverse electronic oscillation while the strong band is due to the longitudinal oscillation of electrons. The peak position of the longitude SPR band for GNRs is found to be very sensitive to the aspect ratio, which is

defined as the ratio of the length of the GNR over the width. When the aspect ratio increased from 2.4 to 7.4, the peak wavelength of the longitude SPR band can be red-shifted from 600 nm to 1000 nm (Figure 1-6).[28] Such tunability in the near-IR region is particularly attractive for biological applications as discussed later. [29]

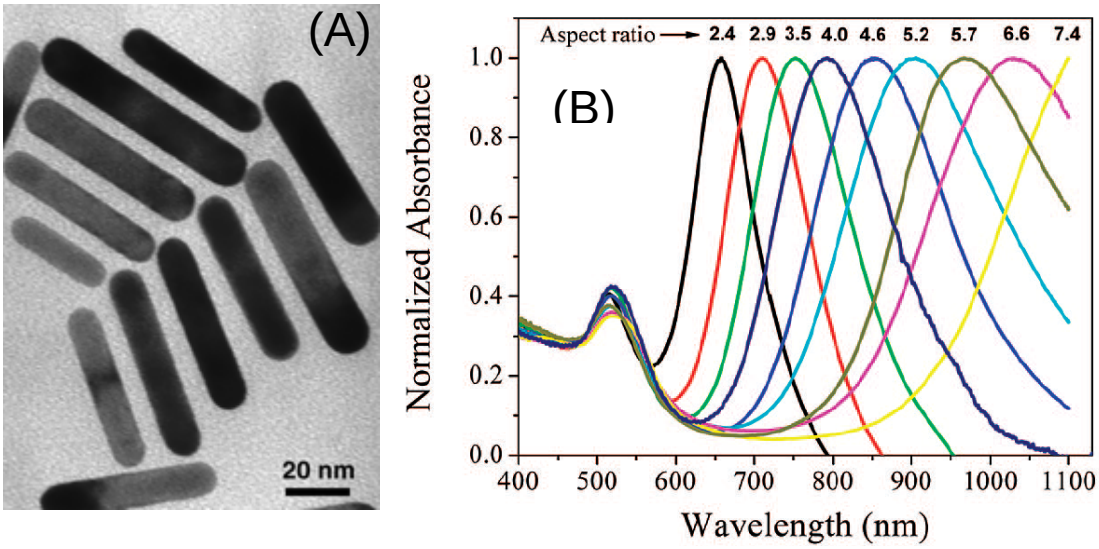

Figure 1- 6. (A) Gold nanorods mirograph obtained by Transmission Electron Microscopy (Copyright ® Royal Society of Chemistry 2001).[30] (B) Tuning the SPR bands of gold nanorods by synthetically controlling the aspect ratios. (Copyright ® 1999 American Chemical Society)

The optical absorption spectra of GNRs could be calculated with modified Mie theory. According to Gans treatment for the dipole approximation, the extinction cross section for elongated ellipsoids is given by:[31,32]

$$\sigma_{ext} = \frac{\omega}{3c}\varepsilon_m^{3/2} V \sum_i \frac{(1/P_j^2)\varepsilon_2}{\{\varepsilon_1 + [(1-P_j)/P_j]\varepsilon_m\}^2 + \varepsilon_2^2} \qquad (1\text{-}4)$$

Where P_j are the depolarization factors along the three *A*, *B* and *C* axis of the nanorod, with $A>B=C$, defined as:

$$P_A = \frac{1-e^2}{e^2}[\frac{1}{2e}\ln(\frac{1+e}{1-e}) - 1] \quad (1\text{-}5)$$

$$P_B = P_C = \frac{1-P_A}{2} \quad (1\text{-}6)$$

with the aspect ratio R included in the expression of *e* as:

$$e = \left[1-(\frac{B}{A})^2\right]^{1/2} = \left(1-1/R^2\right)^{1/2} \quad (1\text{-}7)$$

The tunable absorption spectra of GNRs in the near-IR (NIR) region provide a special advantage in using GNR for biological applications. In the NIR region, especially 650-900 nm, water and tissues (mainly hemoglobin and oxyhemoglobin in the tissue) have minimal absorption in this window (Figure 1-7).[33] By selectively delivering GNPs into target cells and tissues, photon irradiation at NIR wavelength will pose minimum effect on non-targeted cells and tissues. In addition, NIR light can penetrate tissue much deeper than visible light irradiation. A penetration depth of up to 10 cm could be reached using NIR laser irradiation.[33]

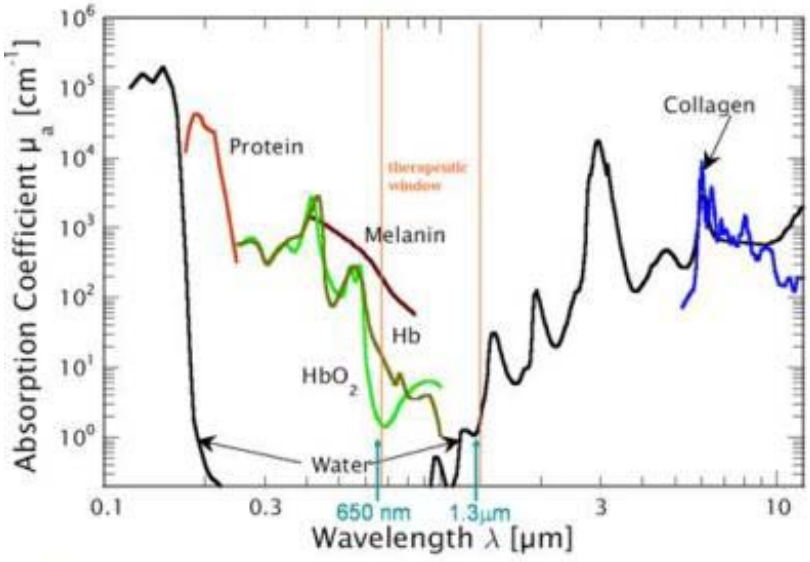

Figure 1- 7. Optical absorption spectra of tissue components in the ultraviolet to infrared range. (Hb: hemoglobin; HbO_2: oxyhemoglobin) (Copyright ® Duke University)

1.3.2 Light scattering property of GNPs

1.3.2.1 Light scattering property of spherical GNPs

GNPs have interesting light scattering properties. When GNPs are illuminated by a narrow beam of white light, GNPs scatter lights in various colors ranging from green, yellow to red as the GNP size increases (Figure 1-8A). [34] For example, Figure 1-8B shows the scattered green lights from 58 nm GNPs and Figure 1-C shows the scattered yellow lights from 78 nm GNPs. The light scattering property of GNPs and its potential applications were investigated by Yguerabide J. et al in 1998. Since then the scattering of GNPs have been studied intensively from both theoretical and experimental aspects.[34]

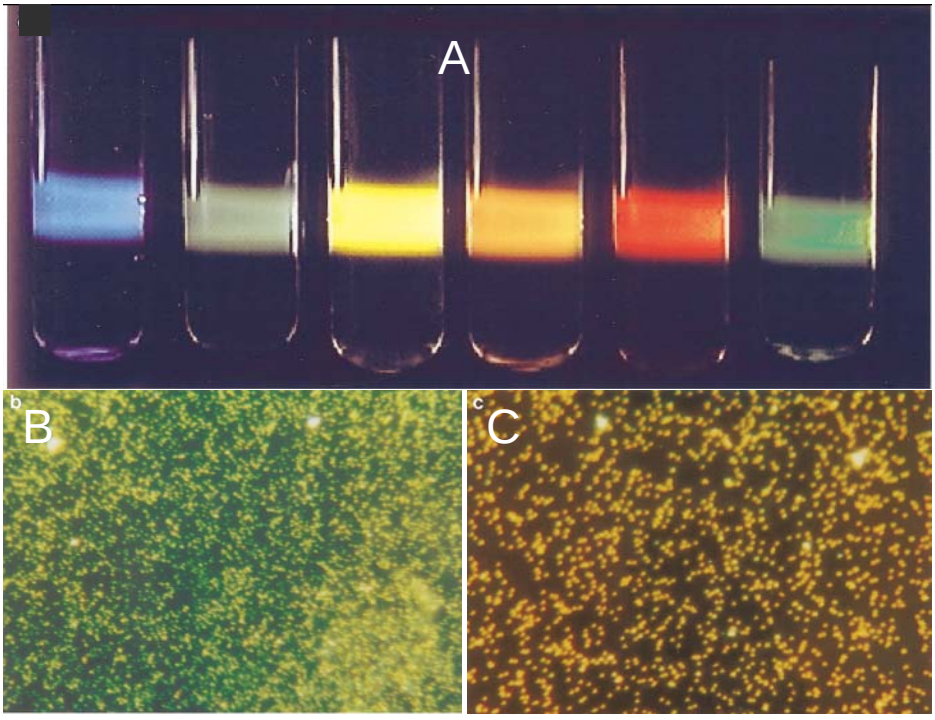

Figure 1- 8. (A) Photographs showing the appearance of light-scattering suspensions. Composition, particle diameter, and particle molar concentration are as follows from left to right: silver, 40 nm (2×10^{-12} M); gold, 40 nm (1.3×10^{-11} M), 78 nm (1.7×10^{-12} M), 118 nm (5×10^{-13} M), and 140 nm (3×10^{13} M); solution of fluorescein (2×10^{-6} M). Scattering photographs of the (B) 58-nm and (C) 78-nm diameter GNPs under an optical microscopy. (Copyright ® 1998 Springer New York)

Theories have been developed to explain the scattering property of GNPs. For small nanoparticles (diameter<0.05λ), in this case of GNPs, only dipole oscillations contribute significantly to the scattering. Rayleigh theory can be used to explain the scattering phenomena of GNPs and the scattering cross section of a GNP can be expressed as:

$$C_{sca} = \frac{2\pi D^6 n_{med}^4}{3\lambda_0^4} \mathrm{Im}\left|\frac{m^2-1}{m^2+1}\right|^2 \quad (1\text{-}8)$$

where D is the particle diameter, n_{med} is the refractive index of the surrounding media, λ_0 is the incident light wavelength, and m is the relative refractive index of the bulk gold at irradiation wavelength λ_0 divided by n_{med}.[34] For large GNPs (diameter>0.05λ), the scattering is considered to be the sum of dipole and higher order oscillations. In Mie theory, the scattering cross section for a GNP can be written as:

$$C_{sca} = \frac{2\pi}{k^2}\sum_{n=1}^{\infty}(2n+1)(|a_n|^2 + |b_n|^2) \quad (1\text{-}9)$$

where $k = 2\pi n_{med}/\lambda_0$. The different terms in the sum correspond to different dielectric and magnetic multipoles and n is the term index. The term index with n=1 corresponds to the electric dipole. The coefficients Bessel function a_n and Ricatti function b_n are generally complex numbers, which depends on the size- and incident light wavelength-related refractive index of the particle.[34]

In 1998, Yguerabide et al. calculated the scattering and absorption cross sections of spherical GNPs at different sizes from 20 to 300 nm according to the above theories and compared them with experimental results.[34] They calculated that the scattering peak

wavelength, intensity and the relative ratio of scattering to absorption were all related with the GNP size. The results are summarized in Table 1-1, Figure 1-9, and Table 1-2.

The SPR scattering peak wavelength (λ_{max}) has two separated trends when the GNP size increases. From size 20 to 160 nm, the λ_{max} shows a red-shift from 535 nm to 635 nm. From 160 to 300 nm, the λ_{max} illustrates a blue-shift from 635 nm to 565 nm when the GNP size increases (Table 1-1 and Figure 1-9).[34] Table 1-2 presents the experimental results of λ_{max} for 52, 78, 87 and 118 nm GNPs, which is in a relatively good agreement with the red-shift trend as predicted in the theoretical calculations. Thus by changing the size, the light scattering profile of GNPs can be tuned.[34]

Table 1- 1. Calculated light absorption and scattering properties of spherical GNPs from 380 to 700 nm

Dia (nm)	λ_{max} (nm)[a]	C_{sca} (cm^2)	$I_U(0)$	$I_U(90)$	ϵ (M^{-1} cm^{-1})	φ_s	Q_{sca}
20	535	8.36×10^{-14}	1.77	0.882	1.57×10^{9}	0.014	0.027
40	535	6.05×10^{-12}	129	63.9	1.63×10^{10}	0.1	0.482
60	545	6.33×10^{-11}	1.35×10^{3}	668	5.32×10^{10}	0.313	2.24
80	555	2.31×10^{-10}	4.97×10^{3}	2.44×10^{3}	1.14×10^{11}	0.546	4.6
100	575	4.56×10^{-10}	9.84×10^{3}	4.83×10^{3}	1.62×10^{11}	0.739	5.81
120	605	6.9×10^{-10}	1.48×10^{4}	7.32×10^{3}	2.07×10^{11}	0.876	6.1
140	635[b]	8.79×10^{-10}	1.89×10^{4}	9.4×10^{4}	2.46×10^{11}	0.94	5.71
160	665	1.02×10^{-9}	2.22×10^{4}	1.11×10^{4}	2.8×10^{11}	0.963	5.09
180	560	1.16×10^{-9}	2.5×10^{4}	1.27×10^{4}	3.14×10^{11}	0.974	4.56
200	565	1.38×10^{-9}	7.53×10^{4}	1.86×10^{4}	4.51×10^{11}	0.788	4.39
300	565	2.94×10^{-9}	1.7×10^{5}	3.82×10^{4}	7.98×10^{11}	0.968	4.16

*$I_U(0)$ and $I_U(90)$ is the scattering light intensities measured at 0 and 90° with respect to the direction of an unpolarized incident light beam. φ_s is the portion of light scattering in the whole extinction which is the sum of both scattering and absorption. ε is the extinction coefficient. (Copyright ® 1998 Springer New York)

The scattering cross section (C_{sca}) of GNPs depends dramatically on their diameter. From equation (1-8), the scattering cross section of a small GNP is proportional to the 6th power of its diameter. As a result, when the size of GNP increases, the

scattering intensity increases dramatically. The scattering cross section C_{sca} increases monotonically from 20 nm to 300 nm, as shown in Table 1-1. A 300 nm GNP has a cross section which is ~4×10^4 times larger than that of a 20 nm GNP. It needs to mention that this number is small than the 6th power of the relative diameter ratio (300 nm/20 nm)^6 because at large sizes the C_{sca} is not proportional to the 6th power of the size anymore. From these results, the light scattering color and power of GNPs can be tuned by varying the size.[34]

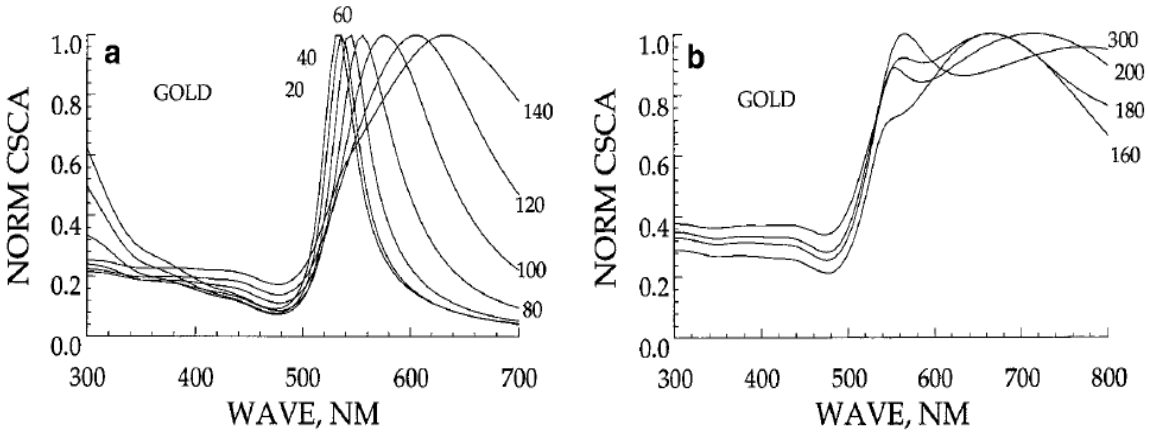

Figure 1- 9. Normalized calculated light scattering cross section versus wavelength for homogenous and spherical GNPs with different sizes according to Mie theory. (Copyright ® 1998 Springer New York)

Table 1- 2. Experimentally determined number of fluorescein molecules (NF) needed to produce the same intensity of light as a GNP at a given diameter (Copyright ® 1998 Springer New York)

Dia (nm)	Wave (nm)	NF[a]	$C_{sca}{}^{d}$ (cm^2)
52	535	6.6×10^4	1.4×10^{-11}
78	555	4.3×10^5	9.2×10^{-11}
87	585	1.1×10^6	2.3×10^{-10}
118	590	2.4×10^6	5×10^{-10}

*Dia: diameter of GNPs; $C_{sca}{}^{d}$ is the experimental scattering cross section of GNPs.

Increasing the size of a GNP not only results in a shift of its SPR scattering peak and an increase in its scattering cross section, but also increases the relative portion of scattering in the whole extinction. Comparing equation (1-8) with equation (1-1), the amplitude increases according to D^6 and D^3, respectively for the scattering cross section and the absorption cross section. As a result, when the GNP size increases, the scattering cross section increases much larger than the absorption cross section. In Table 1-1, the contribution of scattering to the extinction (φ_s) is only 1.4% at the scattering peak (λ=535 nm) for 20 nm GNPs, but increases to 54.6% at the scattering peak (λ=555 nm) for 50 nm GNPs.[34]

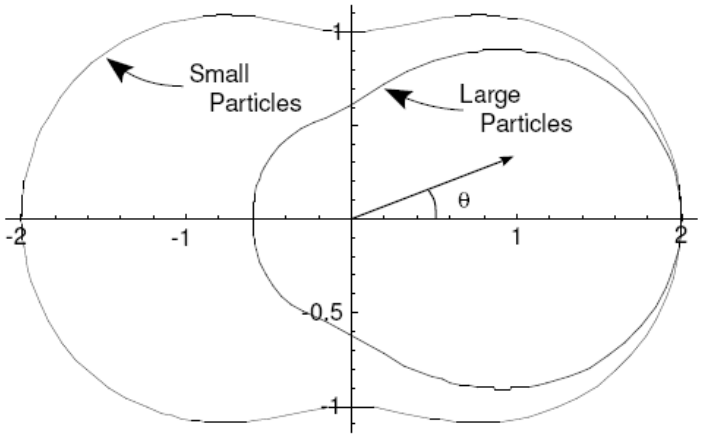

Figure 1- 10. Angular dependent scattering intensity diagrams for both small particles and large particles when irradiated with unpolarized light. (Copyright © 2009 Indian Academy of Sciences)

In the detection of scattered lights from GNPs, the scattering intensity is the sum of scattered lights that can be captured by the detector. The angular dependence of the scattering intensity is related with the polarization of the incident light as well as the GNP size. When a polarized light is irradiated on small GNPs (diameter<0.05λ), the scattering intensity *I* according to Rayleigh theory is:

$$I = \frac{16\pi^4 D^6 n_{med}^4 I_0}{r^2 \lambda_0^4} \left| \frac{m^2 - 1}{m^2 + 2} \right|^2 \sin^2(\alpha) \tag{1-10}$$

where I_0 is the intensity of the incident light, r is the distance of the detection point to the particle, and α is the angle between the detection direction $\boldsymbol{r}$ and the direction of polarization of the incident beam.[34] In the case of unpolarized light illumination, the scattering intensity can be derived according to equation (1-10) and written as:

$$I = \frac{8\pi^4 D^6 n_{med}^4 I_0}{r^2 \lambda_0^4} \left| \frac{m^2 - 1}{m^2 + 2} \right|^2 (1 + \cos^2 \theta) \tag{1-11}$$

where θ is the angle between the incident laser beam and the direction of detection. The shape of the scattering diagram is determined by the $(1+\cos^2\theta)$ term and plotted in Figure 1-10.[35] It can be seen that the scattered light intensity is two times great at θ=0 than that at θ =90^o and varies according to $(1+\cos^2 \theta)$ at intermediate angles.

For larger particles (diameter within *0.05λ-0.5λ*), under unpolarized light illumination, the scattering intensity can be calculated based on Mie theory:

$$I = \frac{\lambda_0^2}{8\pi^2 n_{med}^2 r^2} (|S_1|^2 + |S_2|^2) \tag{1-12}$$

where S_1 and S_2 are functions depending on the scattering angle and the Bessel functions a_n and Ricatti functions b_n (equation 1-9).[35] In this case, the scattered light from different parts of the particle will reach the detector by traveling different path lengths. The net effect is that the scattering diagram for large particles is reduced intensity at back scattering angles (Figure 1-10). The scattering intensity is not symmetric for back and forward scattering. As a result, larger GNPs can be more sensitively detected at forward angles than at 90^o or back scattering angles.

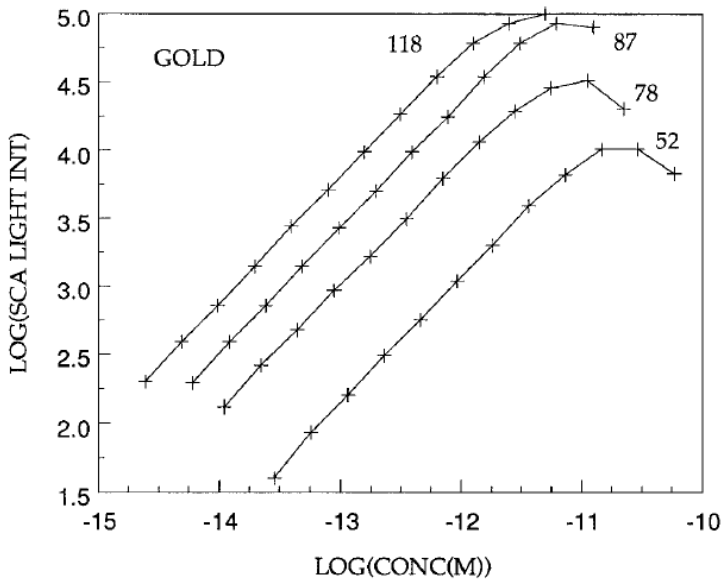

Figure 1- 11. Logarithmic plots showing the dependence of relative light scattering intensity on GNP concentration for GNPs with different sizes (in the unit of nm) (Copyright ® 1998 Springer New York)

The light scattering property of GNPs can be used to detect GNPs. In fact, the strong light scattering of GNPs comparing with other materials makes them to be detected very sensitively. The scattering cross sections of spherical GNPs is 4-6 orders of magnitude larger than that of small fluorescence molecules, polystyrene beads or biomacromolecules, as shown in Table 1-2.[34] For example, a 52 nm GNP produces the same light intensity from scattering as the luminescence light emitted by 4.4×10^{4} fluorescein molecules. GNPs can be detected at very low concentrations, as shown in Figure 1-11.[34] For mono-dispersed GNPs in solution, it was reported that their scattering intensity is linearly correlated to the GNP concentration in log scales with a dynamic range of ~3 orders. Detection limits for spherical GNPs as low as 10^{-14} M (52 nm), 2.5×10^{-15} M (78 nm), 1.6×10^{-16} M (87 nm) and 4×10^{-16} M (118 nm) were reported.

The very low detection limits of GNPs by light scattering make them advantageous to be used as ultra sensitive probes for biological applications. Another advantage of GNPs in these applications is the tunability of their scattering peak wavelengths by changing their size and shape.

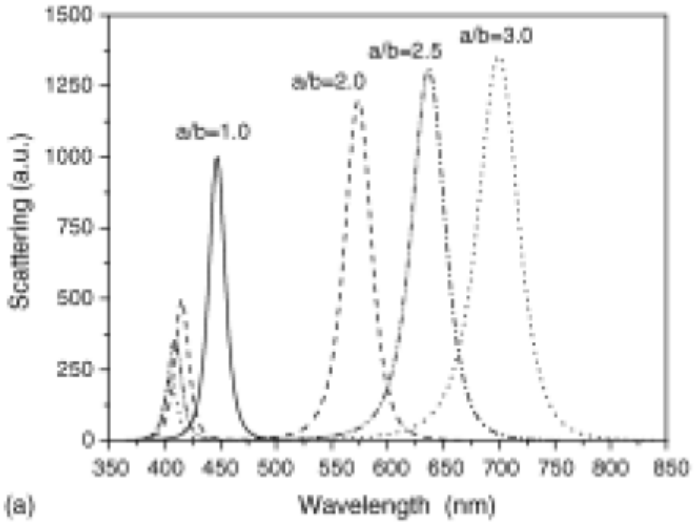

Figure 1- 12. Calculated SPR scattering spectra of GNRs at various aspect ratios. (Copyright ® 2005 Elsevier B.V.)

1.3.2.2 Scattering property of gold nanorods

Lu et al. calculated the theoretical resonant light scattering property of GNRs at various sizes and aspect ratios using the quasi-static theory.[36] The scattering cross section can be written as:

$$\sigma_{sca} = \frac{128\pi^5 a^2 b^4}{3\lambda^4}\left|A + iB\right| \tag{1-12}$$

where a is the half of the rod length, b is the half of the rod width, A and B are functions depending on the dielectric constants of the rod and the surrounding media as well as a and b. The numerical calculation results of the light scattering spectra of GNRs are

shown in Figure 1-12.[36] It can be seen that the SPR peak red-shifts with increased GNR aspect ratio.

El-Sayed et al. calculated the effects of GNR size and aspect ratio on the relative ratio of scattering to absorption by using the discrete dipole approximation (DDA) method. As shown in Figure 1-13, the relative ratio of scattering to absorption increases along the size increase of GNRs, but not changes much by varying the aspect ratio.[37] These results show that the scattering and absorption property of GNRs can be tuned by changing the size and/or the aspect ratio.

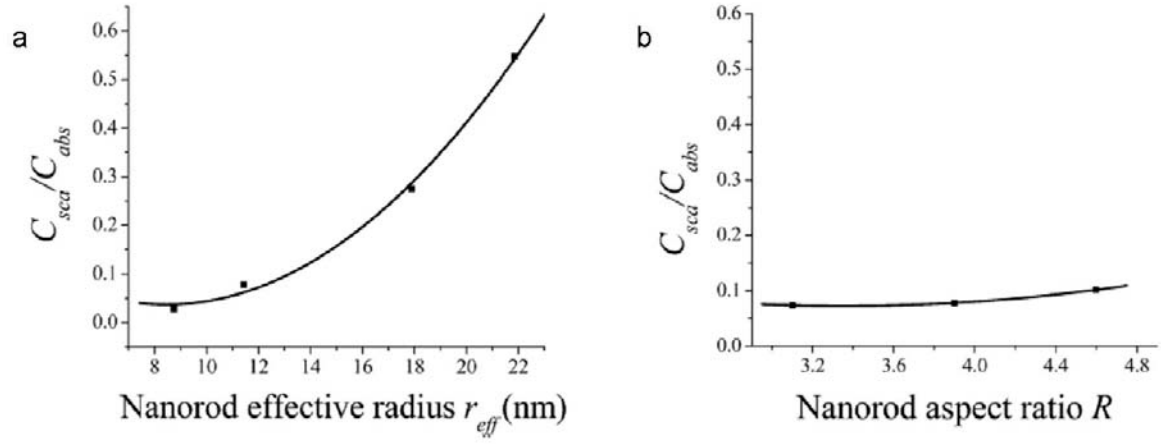

Figure 1- 13. Effects of GNR effective radius (a) and aspect ratio (b) on the relative ratio of scattering to absorption. (the effect radius r_{eff} for GNRs is defined by $r_{eff} = (3V/4\pi)^{1/3}$, where V is the volume of a GNR)

1.3.3 Photothermal energy conversion of GNPs under laser irradiation

When irradiated with a laser beam at a wavelength around the SPR band, GNPs absorb photon energy strongly due to their large absorption cross sections. Because GNPs are not strong luminescent materials, most of the absorbed energy will be released as heat to the local environment of GNPs. This energy dissipation process involves the initial

ultrafast electron-electron scattering (<20 fs), followed by the relative slower cooling due to electron-phonon (~2 ps) and phonon-phonon coupling (>50 ps).[38] According to Fermi liquid theory, for electrons with an initial energy E close to the Fermi energy E_F, the electron-electron scattering time (τ_{e-e}) is reversely related with the square of the energy difference:

$$\frac{1}{\tau_{e-e}} \propto (E - E_F)^2 \qquad (1\text{-}13)$$

For single scattering process, τ_{e-e} is usually on the order of 10 fs. However, the sum of all electron-electron scattering events before the formation of a Fermi electron distribution makes τ_{e-e} to be several hundreds of femtoseconds. As reported by El-Sayed et al, the internal electron-electron thermalization has a fast lifetime of 500 and 450 fs, respectively for 9 nm and 48 nm spherical GNPs. The following slower external electron thermalization (electron-phonon interactions) takes place in a time regime of 1.6 and 1.7 ps, respectively. These results are shown in Figure 1-14. [25]

Because the energy dissipation rate is much slower comparing with the energy absorption rate, as a consequence, the absorbed energy from the laser cannot be dissipated quickly enough from the GNP surface to the environment. This leads to a large increase of the temperature around the GNP surface as well as its vicinity environment. In the case of pulsed laser irradiations, the temperature on the GNP surface could reach as high as more than 1000 ^{o}C. In such a high temperature, GNPs may change their shapes, for example, from gold nanorods to spheres.[39]

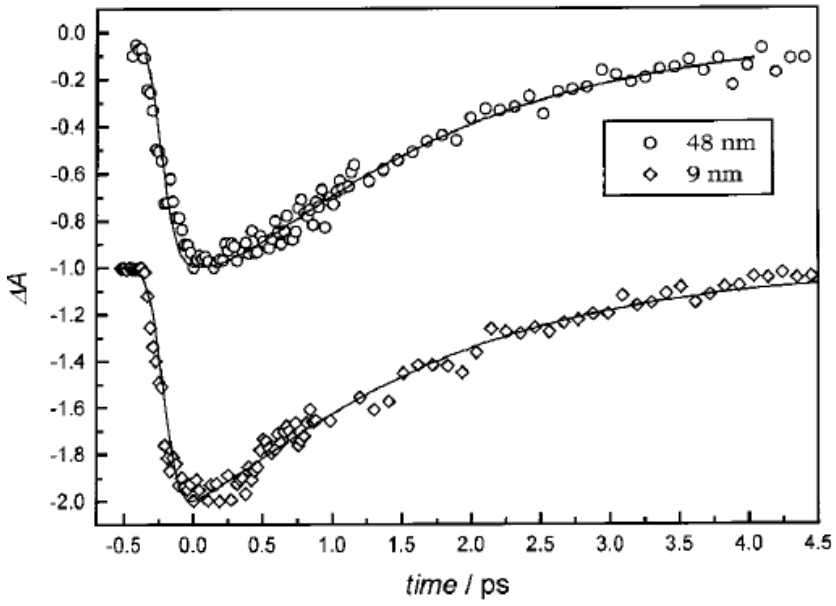

Figure 1- 14. Electron-electron and electron-phonon relaxation times for spherical GNPs at 530 nm after excitation with 630 nm femosecond pulses. (Copyright @ 1999 American Chemical Society)

In the case of continuous wave laser irradiations, the photothermal conversion of GNPs and the following thermal effect to their local environment have also been studied. Govorov et al. calculated the surface temperature increases of a spherical GNP as a function of the particle size and the illumination power according to the usual heat transfer equation:

$$\rho(\mathbf{r})c(\mathbf{r})\frac{\partial T(\mathbf{r},t)}{\partial t} = \nabla k(\mathbf{r})\nabla T(\mathbf{r},t) + Q(\mathbf{r},t) \qquad (1\text{-}14)$$

where $T(\mathbf{r}, t)$ is temperature as a function of coordinate $\mathbf{r}$ and time t, $\rho(\mathbf{r})$, $c(\mathbf{r})$, and $k(\mathbf{r})$ are the mass density, specific heat, and thermal conductivity, respectively. $Q(\mathbf{r}, t)$ is the local heat intensity function and partially depends on the dielectric constants of GNP and also the media. The effects of GNP size, laser wavelength and power to photothermal conversion reaction are shown in Figure 1-15.[40] The surface temperature of GNPs increases along with increased GNP size or laser power density. Following the

temperature increases on the GNP surface, the surrounding media can be heated up due to heat transfer. Water around a GNP can be heated up within a distance of 10s nm to the GNP surface (Figure 1-15a, insert). In another example, Huang et al. calculated that cells loaded with GNPs will be affected by the photothermal conversation reaction of GNPs.[40] This results in an elevated temperature around 70-80^{o}C for cells. These theoretical calculations agree with experimental results obtained from cells which loaded with GNPs, GNRs or gold nanoshells.[41]

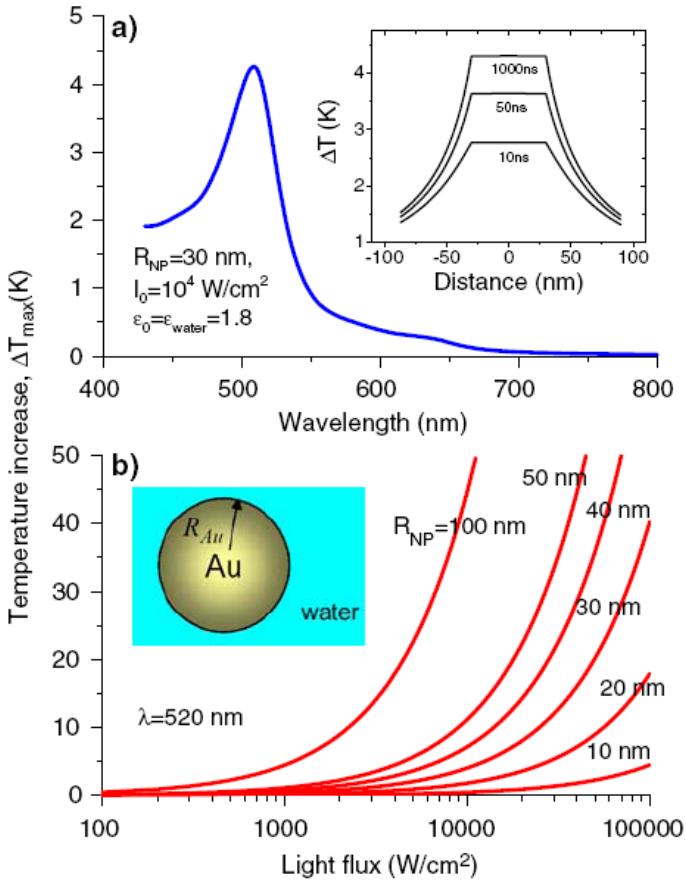

Figure 1- 15. Calculated temperature increase at the surface of a single GNP in water as a function of the irradiation wavelength (a) and the illumination power at the plasmon resonance (b). (insert: spatial distribution of temperature at different time) (Copyright ® 2007 Elsevier B.V.)

1.4 Applications of GNPs in Biological Systems

Advances in the synthesis, modification, biomolecular conjugation, and further understanding of the properties of GNPs have enabled many important applications of GNPs in biological systems. This is a fast growing field since last decade. In addition to biomolecular detection, GNPs are also used in bio-imaging and photothermal therapy. GNPs have been shown to be very promising to help in the diagnostic and treatment of diabetes, cancer, Alzheimer's diseases, and rheumatoid arthritis.[42] The following is a brief review on examples of GNPs applied in biological systems.

1.4.1 Applications of GNPs in biomolecular detection and assays

Biomolecular detection in biofluids or tissue samples is very important for early detection, diagnosis and prognosis of diseases, as well as in drug development. Proteins are one type of biomolecules produced by human body and can be within or located on the cell surface or released into body fluids. An abnormal change of protein levels is often a sign of disease occurrence. For example, a large increase on the level of protstate specific antigen (PSA) in human serum from the normal range (<4 ng/mL) may be associated with the occurrence and progression of prostate cancer. DNAs are another type of important biomolecules which has a significant role in diagnosis and therapy. For example, screening the gene sequences of a patient is necessary to determine the position of mutated genes. This process requires analytical methods with ultra-sensitivity, fast procedure, and using small volumes of samples. Traditional methods such as Enzyme Linked Immunosorbent Assay (ELISA) and Polymerase Chain Reaction (PCR) techniques have been used for decades for protein or DNA detection. Since 1990s, new

analytical have been investigated and developed by introducing GNPs as novel optical probes with better sensitivity, simpler procedure and less cost than traditional methods.

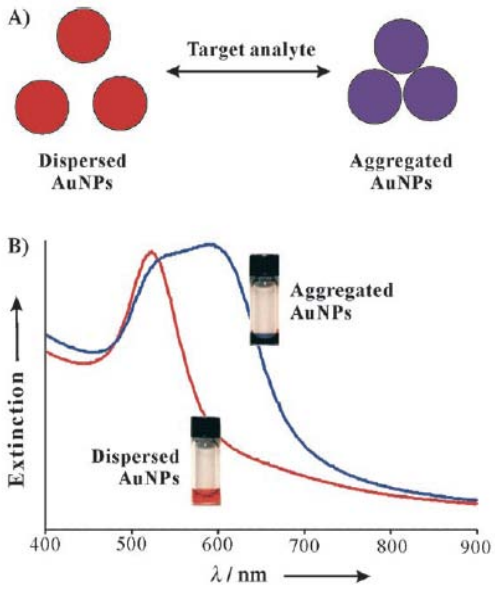

Figure 1- 16. (A) Schematic representation of GNP aggregation reactions (B) SPR band shows a red-shift when GNPs form aggregates in a colorimetric assay. (Copyright ® 2008 John Wiley & Sons, Inc.)

1.4.1.1 Biomolecular assays based on the light absorption property of GNPs

Aggregation of individual GNPs in solution usually introduces a red-shift and broadening of the SPR band. This is a result of surface plasmon coupling between neighboring GNPs when the distance between them is reduced to be within 2-3 times of the particle size. An example is shown in Figure 1-16.[43] The aggregation of GNPs is introduced by bimolecular recognition reactions between the receptor molecules on the GNP surface and the analyte molecules in solution. As a consequence, the SPR peak of the GNP solution shifts from ~520 nm to a higher wavelength around 600 nm. This change is also visible as the solution color changes from purplish to blue. The extent of

the aggregation reaction, and thus the spectrum shift, is associated to the available analyte molecules in the solution. In 1996, Mirkin et al. showed that thiolated ssDNA conjugated 13 nm GNPs could form aggregates through hybridization of ssDNA on GNPs surface with target DNA molecules in solution.[44] Since then, bimolecular assays based on detecting the SPR absorption spectra changes after the aggregation reaction of GNP probes have been applied for a large variety of biomolecules, including nucleic acids, proteins, saccharides.[45]

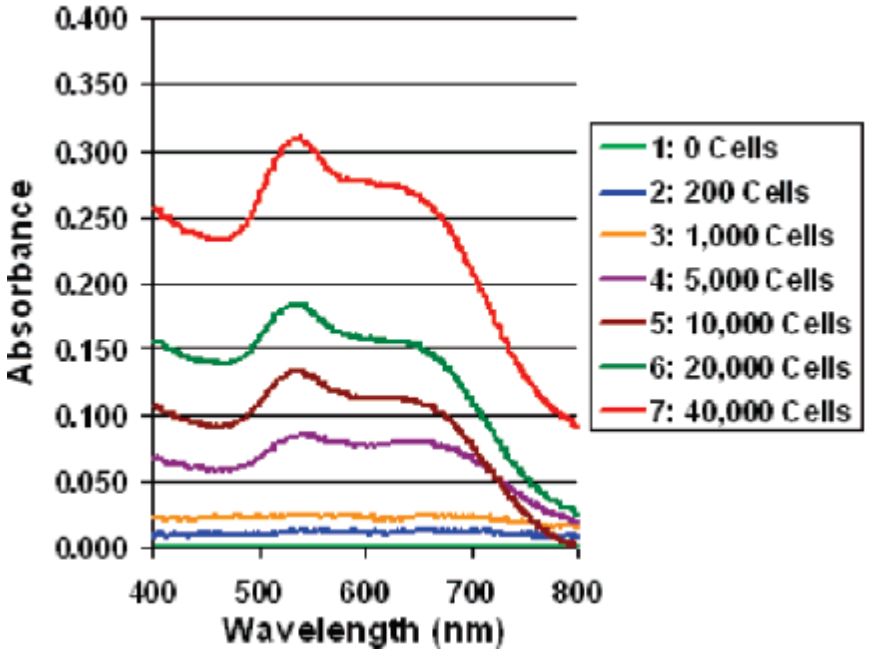

Figure 1- 17. Absorption spectra enhancement effect of aptamer-conjugated GNPs with CCRF-CEM cells (CCL-119 T-cell, human acute lymphoblastic leukemia) at various cell concentrations. (data presented were subtracted from the pure GNP absorption spectrum) (Copyright ® 2008 American Chemical Society)

In addition to the detection of small biomolecules, GNPs are also applied in cell detection. Tan et al. recently applied the spherical GNPs for cancerous cell detection using aptamers-coated GNPs. The aptamers bound specifically to cancer cell surface and bring GNPs to form aggregates on cell surface. As shown in Figure 1-17, this local

aggregation resulted in two effects on the SPR band: a red-shift of the SPR band and an intensity enhancement of the SPR band intensity. Such GNP probes based assay had very high sensitivity for cell detection as few as 90 cells in 300 µL sample solution.[46]

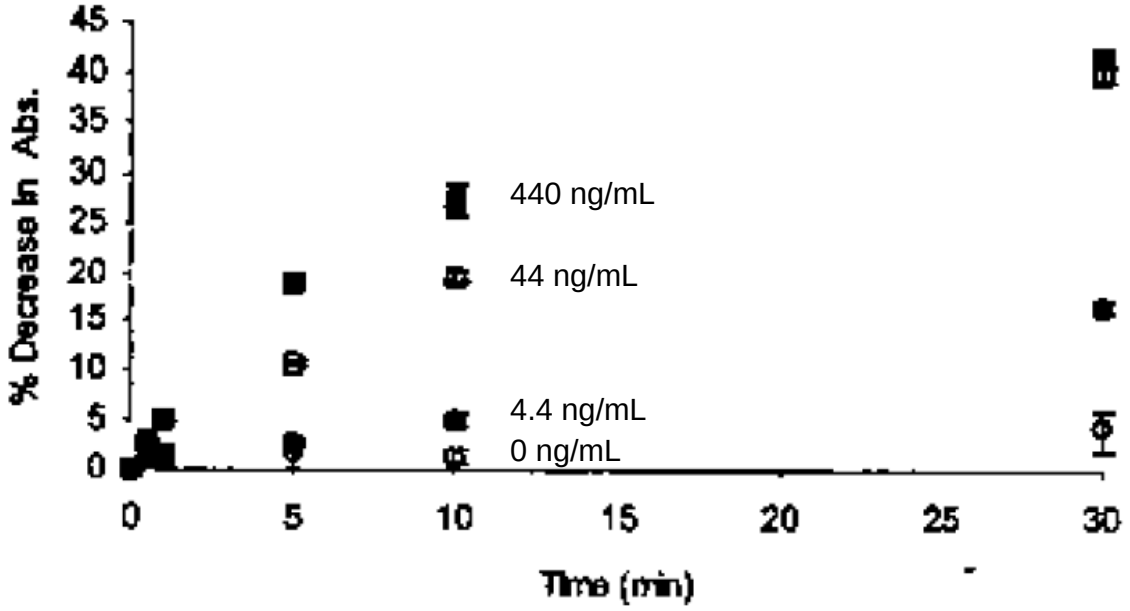

Figure 1- 18. Whole blood tests for rabbit IgG using gold nanoshells (106 nm core diameter with a 25 nm thick gold shell) (Copyright ® 2003 American Chemical Society)

Besides spherical GNPs, nanoshells and nanorods are also used in biomolecular assays. As discussed in 1.3.1.2, these non-spherical GNP probes have a unique advantage because they have SPR band in the NIR region. Figure 1-18 shows an example of using gold nanoshells for the detection of rabbit IgG in whole blood by Hafner et al. Antibody conjugated gold nanoshells formed aggregates through crosslinking with rabbit IgG molecules in the blood sample. This introduced a decrease of the SPR peak absorbance at 720 nm. After 10 minutes of incubation, the absorbances decreases were statistically distinguishable in samples with different rabbit IgG concentrations ranging from 440 ng/mL to 0 ng/mL.[47]

Tailoring the aggregation reaction yields versatile formats for GNPs-based biomolecular assays. As shown in Figure 1-19,[43] there are a variety of designs used in the GNP aggregation assay. In a most common format, shown as pathway A, receptor-conjugated GNPs form aggregates through crosslinking by target molecules. Other formats of assays, such as competitive assays (shown as Figure 1-19B), are also reported. In this case, two GNP probes which have a pair of recognizing biomolecules were used. Without the addition of analyte, these two GNP probes will form aggregates and introduce red-shift of the SPR band. Because the analyte has a specific binding with one of the two GNP probes through bio-recognition reactions, the aggregation reaction is partially or fully hindered by the addition of the analyte depending on its concentrations.[43]

These assays have higher sensitivity than conventional biomolecular assays but easier. Typically, the detection limit is in the range of nM to μM when performed without any signal amplification steps. The detection limit varies with the design of the system, the binding affinity between the receptor molecule on GNP surface and the analyte molecule, as well as other assay conditions. If extra signal amplification steps are used the sensitivity can be further improved to fM for DNA or low pM range for protein detection.[48] However, these amplification steps complicate the assay procedure and often cause problems in the reproducibility of the assays. To solve this problem, alternative methods based on the light scattering property of GNPs have been explored.

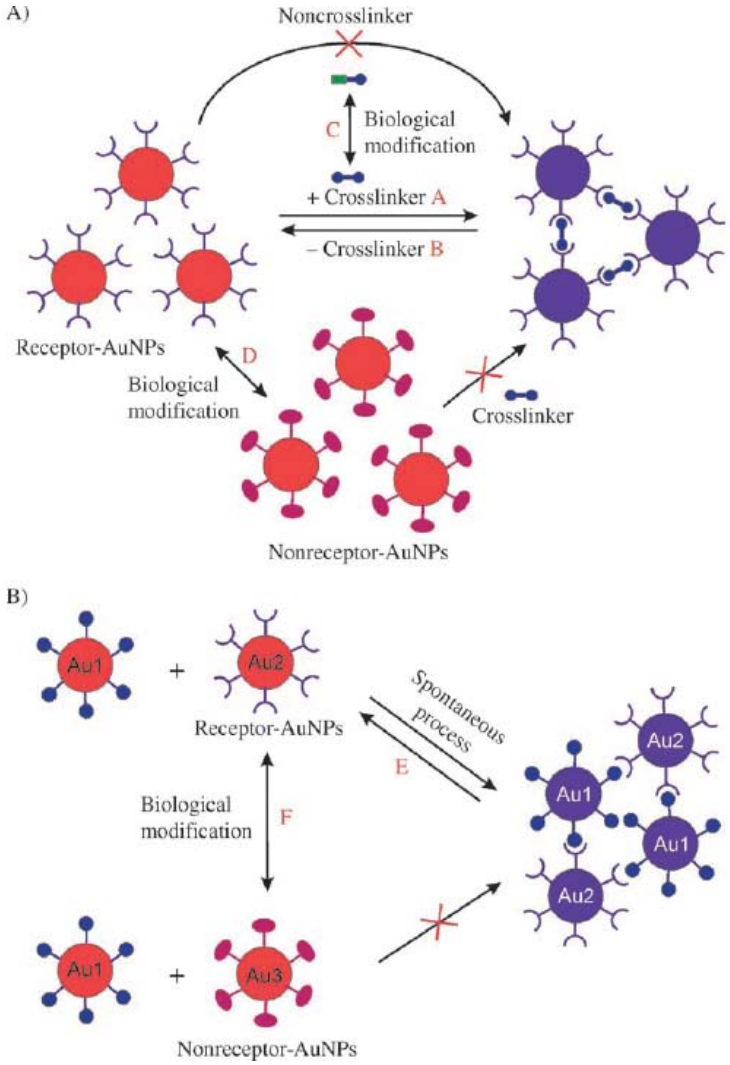

Figure 1- 19. GNP aggregation reaction applied in biomolecules detection. A) GNPs are brought together by crosslinking molecules that have multiple binding sites for the corresponding receptors on GNPs (pathway A). Biological recognition events (or processes) that remove (or break) crosslinking molecules cause GNP de-aggregation (pathway B). Biological recognition events (or processes) that can modify crosslinking molecules (pathway C) or receptors on GNP surface (pathway D) can indirectly control GNP aggregation and dissociation. (B) Competitive GNP assays based on GNP probe aggregation reaction. Without analyte molecules, the two types of multi-valent GNP probes aggregate. With analyte molecules, the aggregation reaction was hindered. (Copyright ® 2008 Elsevier B.V.)

1.4.1.2 Biomolecular assays based on the light scattering property of GNPs

The strong light scattering property of GNPs enables GNPs to be detected by light scattering techniques sensetively. In 1998, Vance et al. found that the hyper-Rayleigh

scattering (the scattering produces frequency doubled light) intensity of spherical GNPs is linearly dependent on GNP concentrations.[49] When GNPs form aggregates, the light scattering intensity increases dramatically due to the SPR coupling of neighboring GNPs. The aggregation reaction detected by light scattering techniques is correlated to the analyte concentration, similarly in absorption property based GNP assays. In 2006, Ray et al. first demonstrated that the hyper-Rayleigh light scattering intensity could be used for DNA detection.[50] As shown in Figure 1-20, when target DNA was present and hybridized with single-strand DNA (ssDNA) on GNP probes, the hyper-Rayleigh scattering intensity at 650 nm (with a 1300 nm incident laser irradiation) was increased dramatically. This assay also had very good selectivity. In the comparison study, the sample which added by single-base mismatched target DNA showed no increases in the scattering intensity (Figure 1-20).[51]

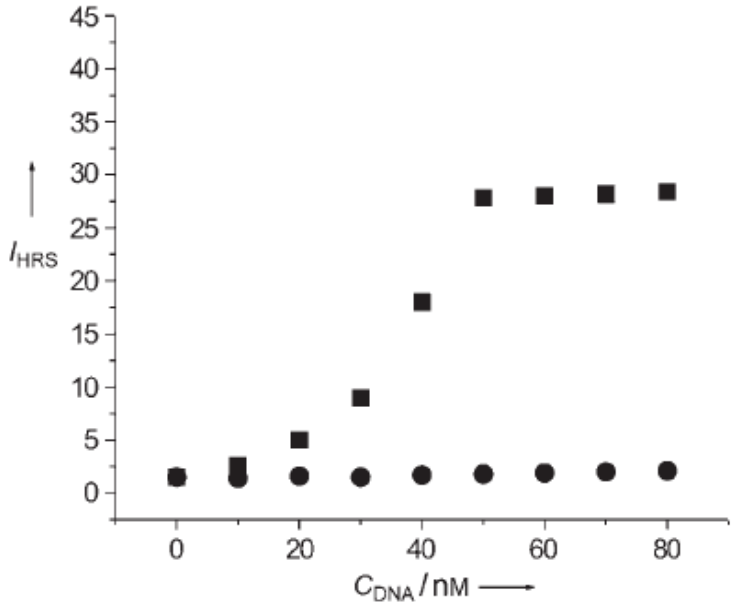

Figure 1- 20. Plot of hyper-Rayleigh scattering intensity versus concentration of target DNA. (Squares: target DNA; circles: target DNA with one base-pair mismatch). (Copyright ® 2006 WILEY-VCH Verlag GmbH & Co. KGaA, Weinheim)

Other than the nonlinear hyper-Rayleigh scattering, other scattering phenomena of GNPs such as the resonance scattering can also be used in biomolecular detection applications. In 2006, Qin et al. used an antibody-labeled 9 nm GNPs to detect proteins Apolopoprotein Al (ApoAl) and Apolipoprotein B by measuring the resonance light scattering intensity. Detections limit were determined to be 2 ng/mL and 0.96 ng/mL, respectively for these two proteins.[51] Liu et al. reported the ssDNA-stabilized GNP probes for target DNA detection with a linear response between the light scattering intensity and the concentration of target DNA from 0.7-110 pM.[52] Du et al. reported a better sensitivity of 10 fM-1 nM for DNA detection by adding a silver enhancement step before the light scattering intensity detection.[53] As shown in Figure 1-21, the scattering light intensity at 315 nm is increased linearly with the target DNA concentration.

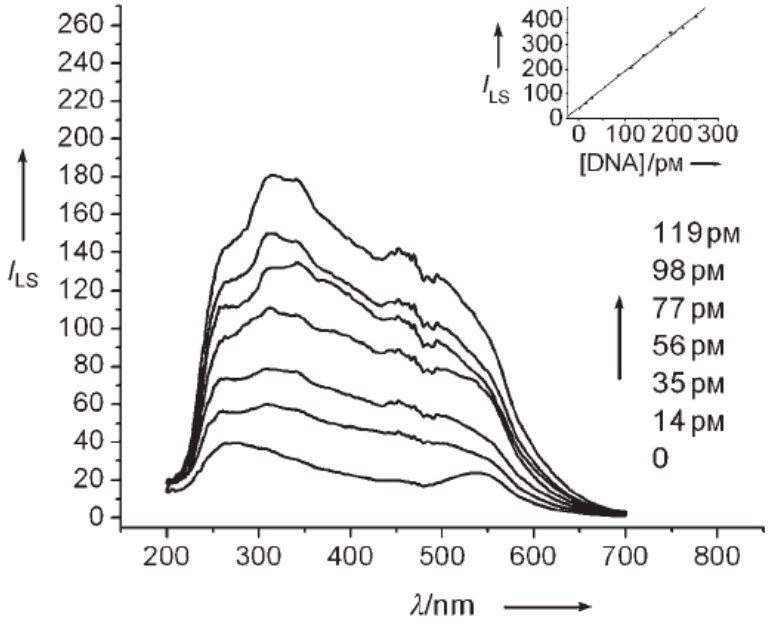

Figure 1- 21. Light scattering spectra of GNPs modified with two probe DNAs for the detection of the complementary DNA target at different concentrations. (Copyright ® 2006 WILEY-VCH Verlag GmbH & Co. KGaA, Weinheim)

Other than their use for homogenous solution assays, GNPs can also be used as for heterogeneous biomolecular assays. Such heterogeneous format assays are similar to the design of solid phase sandwich type immunoassays (such as ELISA) but use biomolecules labeled GNPs as the detection probes. Figure 1-22 is an example to use GNPs in a heterogeneous assay for DNA detection. DNA hybridization reaction is used for target DNA binding. The substrate was washed extensively to lower down the back ground scattering intensities. After that, the light intensity from the resonance light scattering is collected and used for target DNA quantifications. This technique was first invented by Yguerabide et al. in 1998 and now commercially available from Invitrogen Similar concept in a heterogeneous format was also demonstrated by Wang et al. for protein detection with sensitivity in the range of ng/mL.[54]

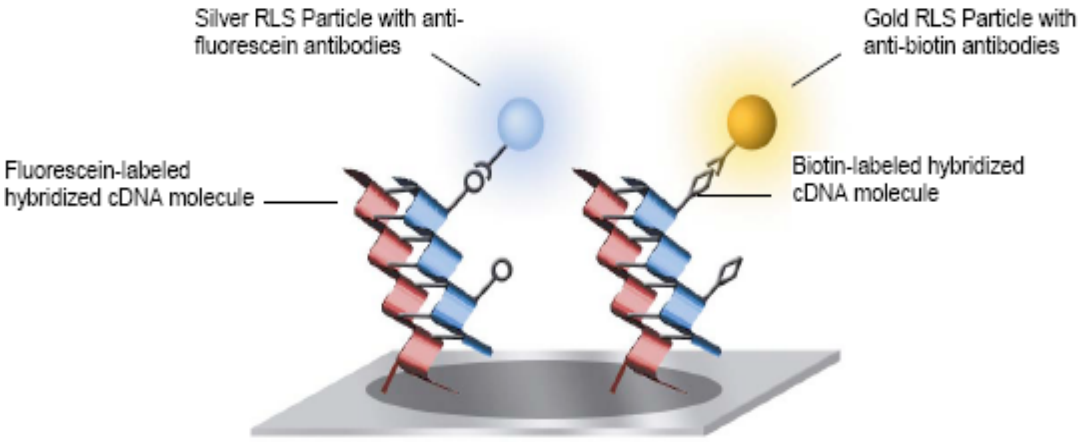

Figure 1- 22. Schematic light scattering detection assay of the GeniconRLSTM two-color DNA microarray kit.[55]

Dynamic light scattering (DLS), also known as photon correlation spectroscopy or quasi elastic light scattering, is a technique used widely for particle size and size distribution studies based on monitoring the scattering intensity variation of the sample

solution at a specific angle. DLS is used routinely to analyze the size and size distribution of polymers, proteins, colloids and nanoparticles. Recently, DLS is used to measure the light scattering intensity in GNPs-based light scattering assays. In 2007, O'Neal et al. used DLS to measure the light scattering intensity of gold nanoshells in whole blood. As shown in Figure 1-23, DLS can detect gold nanoshells down to pM range. The same group also did in vivo study on the uptake of gold nanoshells by mice using DLs as the detection technique. A linear increase in scattering intensity was found when more gold nanoshells were injected into the mouse. These studies show that DLS is a very sensitive and convenient technique in detecting GNPs. [56]

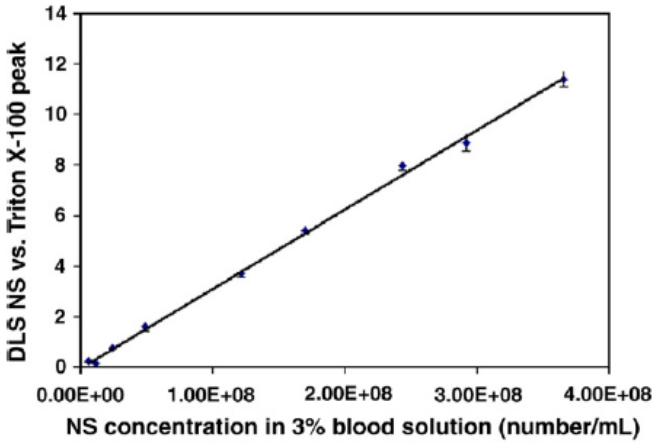

Figure 1- 23. Dynamic Light Scattering intensity area ratio of gold nanoshells to Triton X-100 in 3% murine blood versus gold nanoshells concentrations. (Copyright ® 2007 Elsevier B.V.)

1.4.2 Application of GNPs for enhanced cell imaging and analysis

GNPs have been used as immuno-staining agents in cell studies under Scanning Electron Microscopy (SEM) and Transmission Electron Microscopy (TEM) since 1950s due to the high contrast of gold under electron beam. These techniques are cumbersome in the sample preparation procedure and require well-trained professionals in the

operation. In 1998, Yguerabide et al. used a different imaging technique, dark field optical imcroscopy, to observe the cells stained with GNPs. Due to the strong light scattering of GNPs, cells stained with GNPs can be seen much more clearly under an optical microscopy.[34]

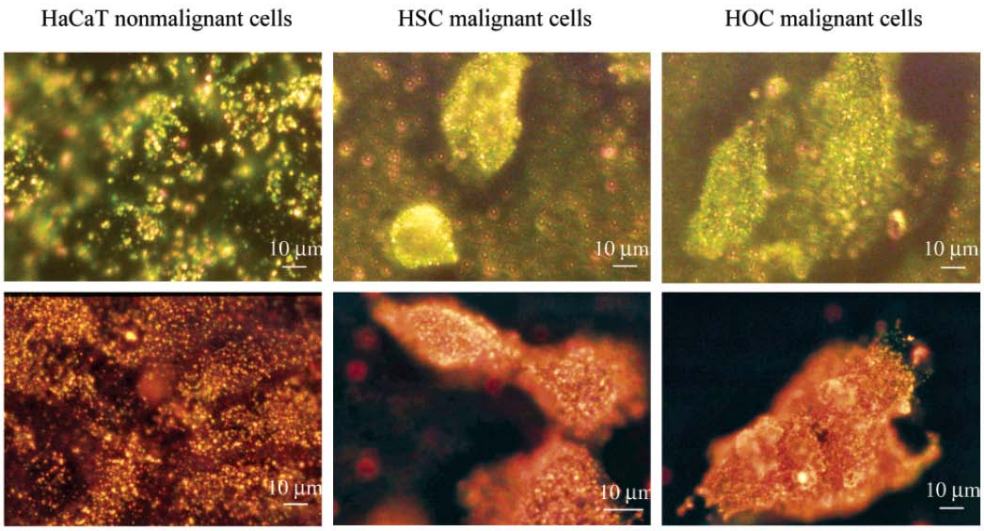

Figure 1- 24. Dark filed imaging for cells after uptake of anti-EGFR (Epithermal Growth Factor Receptor) antibody conjugated spherical GNPs (upper row) and gold nanorods (bottom row). Micrographs are shown for noncancerous cells (left column), and two cancerous cells (middle and right columns) (Copyright ® 2006 Amrican Chemical Society)

Figure 1-24 is an example reported by El-Sayed et al.on cancer cell imaging using GNPs.[29] Epithelial Growth Factor Receptor (EGFR) is a cell-surface receptor. The over expression of EGFR can be associated with a number of cancers. In this example, anti-EGFR antibody conjugated GNPs were used to stain both noncancerous and cancerous cells. The cancerous cells which over-expressed EGFR on the surface showed much brighter color under a dark field microscopy.[57] Clear differences can be seen in the dark field images from cancerous and noncancerous cells. For cancerous cells, GNPs selectively aggregated on the cell surface due to the specific binding of the antibodies on

the GNP surface to EGFR on cell surface. For noncancerous cells, GNPs did not form aggregates as severe as for cancerous cells due to fewer EGFR on cell surface. As a result, cancerous cells were much brighter than noncancerous cells.

There are many unique advantages to use GNPs in cell imaging and analysis, comparing with other cell imaging agents such as fluorescence dyes. For example, GNPs are resistant to photobleaching. Photobleaching is a serious problem for fluorescence dyes especially if a long observation time is required in certain cell studies. In contrast, GNPs are much stable and thus very suitable to trace cell-related reactions at long time scales. Another advantage of GNPs is the much larger light scattering coefficient than the light emission efficiency of fluorescence dyes. A single GNP could be easily seen under dark field imaging using an optical microscopy with simple setups. These unique advantages enable GNPs as very promising imaging contrast agents for cell studies.

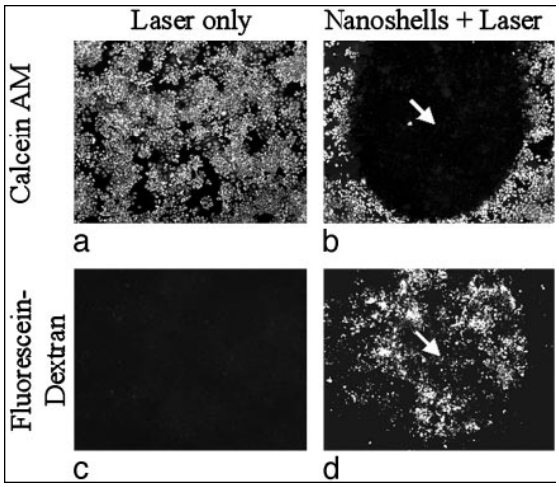

Figure 1- 25. Cells irradiated in the absence of gold nanoshells maintained both viability (a) (as indicated by the calcein fluorescence) and membrane integrity (c) (as indicated by the lack of intracellular flouroscein dextran uptake), while cells irradiated in the presence of gold nanoshells showed cell death and membrane corrupt. (Copyright ® 2003, The National Acedemy of Sciences)

1.4.3 GNPs enhanced photothermal therapy

The photothermal conversion property of GNPs makes them very promising to be used as "cellular bombs" in destroying disease cells through photothermal therapy. When GNPs are delivered specifically to disease cells by bio-recognition reactions, a laser irradiation can introduce photothermal conversion and create a high temperature around GNPs. Cells nearby the GNPs will be affected and then lose their biological activity during the laser irradiation process.

In 2003, Halas et al. used antibody-conjugated gold nanoshells for photothermalysis of human breast cancer cells. In an in-vitro test, as shown in Figure 1-25, tumor cells loaded with gold nanoshells were found to become dead after laser irradiation, while normal cells were not affected under the same experimental condition. In an in-vivo study, solid tumors treated with gold nanoshells had an increase in the temperature up to $\Delta T=37.4\ ^{o}C$. Tumors showed irreversible tissue damage within 4-6 minutes of laser irradiation by a 4 W/cm^2 laser at 820 nm irradiation. [58]

El-Sayed et al. also used both 40 nm spherical GNPs and 40 GNRs for in-vitro photothermalysis of two squamous carcinoma cells lines. The uptake of the 40 nm GNPs was confirmed by dark field imaging. When irradiated by a laser at 430 nm, the cancerous HOC and HSC cells (two oral squamous carcinoma cells) suffered damage within 4 minutes of irraditation at laser energy thresholds (19 W/cm^2 and 25 W/cm^2), while damage was observed from healthy HaCaT cells (one benign epithelia cell) at a much higher laser energy threshold (57 W/cm^2). [59]

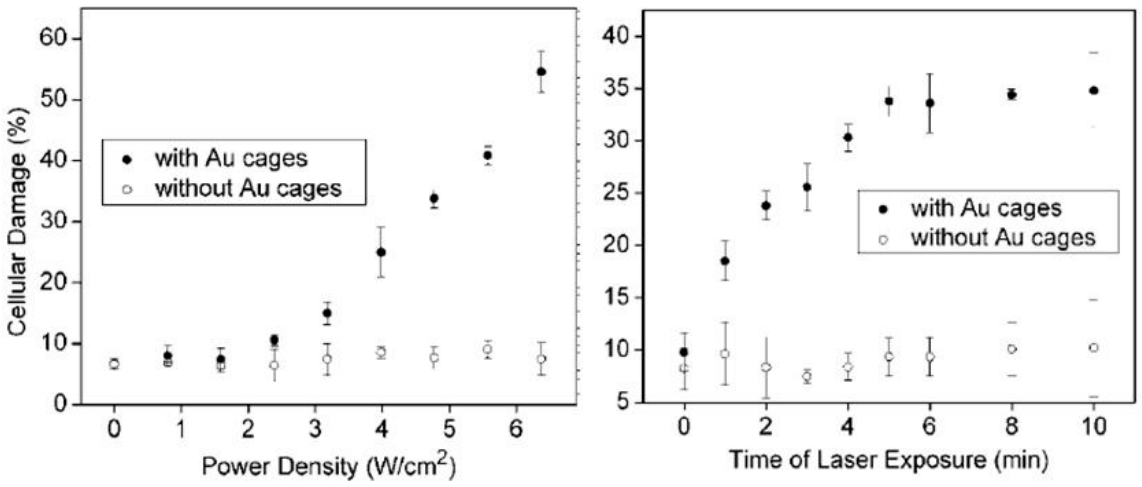

Figure 1- 26. Plots of celluar damage versus laser power density (left) and laser exposure time (right) for SK-BR-3 cells loaded with gold nanocages.

In 2008, Xia et al. reported a quantitative study on the cellular damage of breast cancer in the GNP-assisted photothermalysis. Gold nanocages with average length of 65 nm and SPR band at 800 nm were conjugated with anti-HER2 antibodies to target breast cancer cells (SK-BR-3) through the over-expressed EGFR on cell surface. As shown in Figure 1-26, cells loaded with gold nanocages responded immediately to the laser irradiation and the cellular damage was irreversible at power densities greater than 1.6 W/cm^2. The percentage of dead cells increased with increasing exposure time up to 5 min and then became steady.[60]

1.5 Summary of the Dissertation

The synthesis, surface modification, biomolecular conjugation, and applications of GNPs in bio-sensing, bioimaging and photothermal therapy have been studied extensively over the last two decades and these research areas are still in fast growing. However, there are remaining many questions and challenges.

First, the synthetic mechanism of GNPs with respect to reaction conditions is not well-understood. Nanoparticle growth in solution is a rather complicated process governed by many thermodynamic and kinetics factors. We addressed these questions in Chapter 2 and Chapter 3.

In Chapter 2, we conducted both experimental and theoretical study on the kinetics of Brust-Schiffrin reaction for the synthesis of gold nanoparticles. Using a large excessive amount of thiol ligands, the nanoparticle growth was stopped at different intermediate stages. Our study revealed and confirmed that the reproducibility of Brust-Schiffrin reaction for the synthesis of gold nanoparticles with diameter around 2 nm is rather poor due to the intrinsic complexity of this two-phase reaction. The analysis results of each intermediate product by TEM showed that nanoparticles grew very rapidly at early stage of reaction and reached a maximum value of 2.6 nm at reaction time of around 10 minutes. Further increase of reaction time led to a decrease of nanoparticle size. In addition to the experimental study, we proposed a kinetic model for nanoparticle growth in solution by assuming that the nanoparticle core expands through incremental addition of gold atoms to the existing nanoparticle nuclei. This model not only gave a relatively good fitting to the experimental data, but also provided further insight into the nucleation and core expansion stage of the nanoparticle growth, which has not been revealed in previous modeling studies.

In Chapter 3, we investigated the kinetic growth procedure of the 7.8 nm oleylamine protected GNPs. The time-dependent size and SPR band changes of GNPs were monitored by UV-Vis and TEM, respectively. The chemical structure changes of these oleylamine ligands before and after the GNPs synthesis reaction was investigated in

detail. It was found that experimental results supported the transition of oleylamine to oleyamide during the reaction. Oleylamine ligands formed large complex aggregates with gold salt instantly upon mixing these two agents together. At an elevated temperature of 80 ^{o}C, the complex decomposed first into very small particles and then the small particles recombined together into larger and thermally stable particles with an average core size around 9-10 nm. The oleylamide ligands formed a protecting monolayer around the nanoparticles through a hydrogen bonding network between the amide groups. The recombination of small particles into larger ones was found to follow a logistic model, as confirmed by a nonlinear regression fitting of the UV-Vis absorption data of the reaction solution with the mathematical model.

Second, to have controlled surface functionality on the GNP surface, especially mono-functionality, remains difficult. The well-known place exchange reaction in solution produces multiple functionalized GNPs. In Chapter 4, we used a solid phase assisted place exchange reaction in the preparation of single-functional GNPs. This is based on the ligands absorbing property of solid resins and the place exchange reaction of thiol molecules to GNPs. Bi-functional thiol ligands are first trapped by the ionic resin. This is due to electrostatic interactions between the carboxylic groups on one end of these ligands and the surface charged groups on ionic resin surface. GNPs at size ~2 nm were then added and the place exchange reaction was performed in such condition where the mobility of the bi-functioal thiol ligans was restricted. As a result, single carboxyl group functional GNPs were synthesized and verified by diamine coupling reactions. These novel mono-functional GNPs could be used as the building blocks for functionalized materials syntheses and applications.

Third, the optical property of GNPs, especially in the analytical perspective, has more to be revealed out. In Chapter 5, we investigated systematically the SPR absorption and scattering property of GNPs, and determined the detection limits of GNPs in DLS measurements. Three different types of GNPs with sizes range from 3.76 nm to 250 nm were prepared and studied: citrate-stabilized nanoparticles in eleven different sizes; oleylamide-protected gold nanoparticles with a core diameter of 8 nm, and a decanethiol-protected nanoparticle with a diameter of around 4 nm. A linear relationship between the logarithms of extinction coefficients and core diameters of gold particles was found independent of the capping ligands on the particle surface and the solvents used to dissolve the nanoparticles. This linear relation may be used as a calibration curve to determine the concentration or average size of an unknown nanoparticle or nanoparticle-biomolecule conjugate sample. Detection of GNPs by DLS revealed out that DLS is a very sensitive technique in measuring GNP size, concentration and aggregations.

The last challenge is to prepare stable and also bio-functionalized GNPs and apply to biological applications. Current reports already demonstrated that GNPs have great potentials in biological applications. However, robust and reproducible GNPs-based techniques have not been very successful. Motivated by to develop GNPs-based techniques for realistic applications, we explored the great potential applications of GNPs in immunoassay (Chapter 6, Chapter 7 and Chapter 8), bio-imaging and photothermal therapy (Chapter 9) based on the strong light scattering property of GNPs.

In Chapter 6, we developed a one-step, washing-free and amplification-free assay for protein analysis using GNPs and DLS technique. Specific biomolecular interaction-induced nanoparticle aggregation is monitored by DLS, and the degree of aggregation is

correlated to protein analyte concentration. We then investigated the kinetics of nanoparticle aggregation and developed two formats of assays using mouse IgG as the target protein. Effects of reaction time, temperature, and GNP probe concentration on the aggregation process were revealed. In this one-step assay, mouse IgG can be detected at concentrations from 7.8 pg/mL to 50 ng/mL (or approximately 52 fM to 0.33 nM) without any amplification process. A second format of assay developed in this study is a competitive assay conducted by using both mouse IgG and goat anti-mouse IgG-conjugated GNPs. This competitive assay avoided the problem of "hook effect" as often encountered in non-competitive assays. In this work, we demonstrated here that by using GNPs as a light scattering enhancer and selecting the proper assay formats, low cost, easy-to-conduct, and highly sensitive bioassays can be developed for protein detection and analysis.

In Chapter 7, GNPs were used for in-vitro diagnostic of protein cancer biomarkers. The concept was proved by using two GNP probes, 40 nm spherical GNPs and 40 nm by 10 nm gold nanorods, with two paired antibodies for prostate specific antigen (PSA) conjugated onto each probe respectively. When the two probes were added into the PSA antigen solutions, the two GNP probes formed aggregates through the sandwich type conjunction with the bi-valent antigen in the center. The extent of the aggregation reaction was found to be correlated with PSA concentrations. Such aggregation reaction was detected by Dynamic Light Scattering (DLS) very sensitively. This work demonstrated a one-step washing-free and amplification-free immunoassay for cancer biomarker PSA detection. The novel immunoassay showed advantages of higher sensitivity, simplified procedure and cost reduction over conventional assays.

In Chapter 8, robust PEG-coated GNPs were prepared through the place exchange reaction of thiolated PEG polymers and citrate-protected GNPs. These robust GNPs were subjected to test their resistance from aggregation in solutions with a high ionic strength or at different pH values. The robust 40 nm and 100 nm PEG-coated GNPs were used to covalently bond with free-PSA antibodies to form robust GNP probes. The conjugate of antibodies to GNPs were verified by DLS. These probes were used in the development of free-PSA immunoassays. Better sensitivity down to 0.046 ng/mL for f-PSA was achieved.

In Chapter 9, GNPs were used for in-vitro bio-imaging and photothermal therapy of tumor cells. Based on their strong scattering properties, antibody coated 40 nm GNPs were conjugated with A547 lung cancer cells. This can be imaged clearly under dark field microscopy. Cells after GNPs uptake were irradiated with a continuous laser beam with the wavelength at 633 nm. The viability loss of cancer cells during the laser irradiation was monitored in real time under a confocal microscopy. It is found that GNPs can accelerate the death of cells as soon as the laser irradiation started. Power and irradiation time were found to greatly affect the cell death rate. At a 3.75 mW/cm^2 irradiation power density, the fastest cell death rate was observed. The irradiation time of 60 seconds was found to introduce 98% viability drop of cells, with much reduced irradiation time and much higher viability drop comparing with literature results for other cancer cells. In contrast, cells without GNPs maintained a high bio-activity. In this work, the combined bio-imaging and photothermal therapy of lung cancer cell A549 were demonstrated.

References:

1 (a) Templeton, A.C.; Wuelfing, W.P.; Murray, R.W. Acc. Chem. Res. 2000, 33, 27-36. (b) Daniel, M.C.; Astruc, D. Chem. Rev. 2004, 104, 293-346. (c) Hutchings, G.J.; Brust, M.; Schmidbaur, H. Chem. Soc. Rev. 2008, 37, 1759-1765.

2 Hunt, L.B. Gold Bulletin 1976, 9, 134-139.

3 Faraday, M. Philos. Trans. R. Soc. London 1857, 147, 145.

4 (a) Turkevich J.; Hillier, J.; Stevenson, P.C. Discuss. Faraday Soc. 1951, 11, 55-74. (b) Frens, G. Nat. Phys. Sci. 1973, 241, 20. (c) Enustun, B.V.; Turkevich, J. J. Am. Chem. Soc. 1963, 85, 3317-3328. (d) Turkvich, J. Gold Bull. 1985, 18, 86-91. (e) Turkevich, J. Gold Bull. 1985, 18, 125-131. (f) Pong, B.-K.; Elim, H.I.; Chong, J.-X.; Ji, Wei, Trout, B.L.; Lee, J.-Y. J. Phys. Chem. C 2007, 111, 6281-6287.

5 (a) Schmid, G.; Boese, R.; Pfeil, R.; Bandermann, F.; Mayer, S.; Calis, G.H.M.; van der Velden, J.W.A. Chem. Ber. 1981, 114, 3634. (b) Schmid, G.: Baumle, M.; Geerkens, M.; Heim, I.; Osemann, C.; Sawitowski, T. Chem. Soc. Rev. 1999, 28, 179-185. (b) Schmid, G. Chem. Soc. Rev. 2008, 37, 1909-1930.

6 Brust, M.; Walker, M.; Bethell, D.; Schiffrin, D.J.; Whyman, R. Chem. Commun. 1994, 801-802.

7 Hostetler, M. J.; Wingate, J. E.; Zhong, C.-J.; Harris, J. E.; Vachet, R. W.; Clark, M. R.; Londono, J. D.; Green, S. J.; Stokes, J. J.; Wignall, G. D.; Glish, G. L.; Porter, M. D.; Evans, N. D.; Murray, R. W. Langmuir 1998, 14, 17-30.

8 Jana, N.R.; Gearheart, L; Murphy, C.J. Chem. Mater. 2001, 13, 2313-2322.

9 (a) Stoeva, S.; Klabunde, K.J.; SOrense, C.M.; Dragieva, I. J. Am. Chem. Soc. 2002, 124, 2305-2311. (b) Shimizu, T.; Teranishi, T.; Hasegawa, S.; Miyake, M. J. Phys. Chem. B 2003, 107, 2719-2724.

10 (a) Leff, D.V.; Brandt, L.; Heath, J.R. Langmuir 1996, 12, 4723-4730. (b) Hiramatsu, H.; Osterloh, F.E. Chem. Mater. 2004, 16, 2509-2511. (c) Newman, J.D.S.; Blanchard, G.J. Langmuir 2006, 22, 5882-5887.

11 (a) Yu, Y.-Y.; Chang, S.-S.; Lee, C.-L.; Wang, C.R. J. Phys. Chem. B 1997, 101, 6661. (b) Gao, J.; Bender, C.M.; Murphy, C.J. Langmuir 2003, 19, 9065-9070. (c) Nikoobakht, B.; El-Sayed, M.A. Chem. Mater. 2003, 15, 1957-1962. (d) http://www.nanopartz.com/

12 Sun, Y.; Xia, Y. Science 2002, 298, 2176.

13 (a) Pham, T.; Jackson, J.B.; Halas, N. J.; Lee, T. R. Langmuir 2002, 18, 4915-4920. (b) Nooney, R.I.; Dhanasekaran, T.; Chen, Y.; Josephs, R.; Ostafin, A.E. Adv. Mater. 2002, 14, 529-532. (c) Graf, C.;

Vossen, D.L.J.; Imhof, A.; Blaaderen, A.v. Langmuir 2003, 19, 6993-6700. (d) Tovmachenko, O.G.; Graf, C.; Heuvel, D.J.v.d.; Blaaderen, A.v.; Gerritsen, H.C. Adv. Mater. 2006, 18, 91-95.

14 Nehl, C.L.; Liao, H.; Hafner, J.H. Nano. Lett. 2006, 6, 683-688.

15 (a) Kehle, T.; Herzog, V. European J. of Cell Biology 1987, 45, 80-87. (b) Englebienne, P. Analyst 1998, 123, 1599-1603. (c) Ghitescu, L.; Bendayan, M. J. Histochem. Cytochem. 1990, 11, 1523-2530. (d) Pissuwan, D.; Cortie, C.H.; Calenzuela, S.M.; Cortie, M.B. Gold Bulletin 2007, 40, 121-130. (e) Roe, C.D.; Courtoy, P.J.; Baudhuin, J. Histochem. Cytochem. 1987, 35, 1191-1198. (f) He, W.; Huang, C.Z.; Li, Y.F.; Xie, J.P.; Yang, R.G.; Zhou, P.F.; Wang, J. Anal. Chem. 2008, 80, 8434-8430.

16 Zheng, M.; Huang, X. J. Am. Chem. Soc. 2004, 126, 12047-12054.

17 Wuefing, W.P.; Stephen, M.G.; Miles, D.T.; Murray, R.W. J. Am. Chem. Soc. 1998, 12696-12697.

18 Chapman, A.P. Adv. Drug Delivery Rev. 2002, 54, 531-545.

19 (a) Miyamoto, D.; Ioshi, M.; Kojima, K.; Yoshimoto, K.; Nagasaki, Y. Langmuir 2008, 24, 5010-5017. (b) Eck, W.; Craig, G.; Sigdel, A.; Ritter, Gerd, Old, L.J.; Tang, L.; Brennan, M.F.; Allen, P.J.; Mason, M.D. ACS Nano 2008, ASAP. (d) Qian, X.; Peng, X.-H.; Ansari, D.O.; Yin-Goen, Q.; Chen, G.Z.; Shin, D.M.; Yang, L.; Young, A.N.; Wang, M.D.; Nie, S. Nat. Biotech. 2007, 26, 83-90.

20 (a) Kumar, C.S.; Leuschner, C.; Doomes, E.E.; Henry, L.; Juban, M.; Hormes, J. J. Nanosci. Nanotech. 2004, 4, 245-249. (b) Yam, C.M.; Pradier, C.M.; Salmain, M.; Fischer-Durand, N.; Jaouen, G. J. Colloids and Interface Science 2002, 245, 204-207.

21 Koh, A.L.; Sinclair, R. Mater. Res. Soc. Symp. Proc. 2007, 1019, 1019-FF05-01.

22 Brisson, A.; Mornet, S. PCT Int. Appl. 2007. WO200712250.

23 Jain, P.K.; Huang, X.; El-Sayed, I.H., El-Sayed, M.A. Plasmonics 2007, 2, 107-118.

24 Mie, G. Ann. Phys. 1908, 25, 377.

25 (a) Link, S.; El-Sayed, M.A. J. Phys. Chem. B 1999, 103, 8410. (b) Jain, P.K.; El-Sayed, I.H.; El-Sayed. Nanotoday 2007, 2, 18-29.

26 Link, S.; El-Sayed, M.A. J. Phys. Chem. B 1999, 103, 4212-4217.

27 Haiss, W.; Thanh, N.T.K.; Aveyard, J.; Fernig, D.G. Anal. Chem. 2007, 79, 4215-4221.

28 (a) Link, S.; Mohamed, M. B.; El-Sayed, M. A. J. Phys. Chem. B 1999, 103, 3073. (f) Yan, B.; Yang, Y.; Wang, Y. J. Phys. Chem. B 2003, 107, 9159.

29 Huang, X.; El-Sayed, I.H.; Qian, W.; El-Sayed, M.A. J. Am. Chem. Soc. 2006, 128, 2115-2120.

30 Dujardin, E.; Hsin, L.-B.; Wang, C.R.; Mann, S. Chem. Comm. 2001, 1264-1265.

31 Gans, R. Ann. Phys. 1015, 47, 270.

32 Papavassiliou, G.C. Prog. Solid State Chem. 1980, 12, 18.

33 http://www.chem.duke.edu/~wwarren/tissueimaging.php

34 (a) Yguerabide, J.: Yguerabide, E.E. Anal. Biochem. 1998, 262, 137-156. (b) Yguerabide, J.: Yguerabide, E.E. Anal. Biochem. 1998, 262, 157-176.

35 http://www.ias.ac.in/initiat/sci_ed/resources/chemistry/LightScat.pdf. Retrived on Oct. 20, 2009.

36 Zhua, J.; Huanga, L.; Zhaoa, J.: wang, Y.; Zhaoao, Y.; Haoa, L.: Lu, Y. Mater. Sci. Eng. B 2005, 121, 199-203.

37 Jain, P.K.; Lee, K.S.; El-Sayed, I.H.; El-Sayed, M.A. J. Phys. Chem. B. 2006, 110, 7238-7248.

38 Itoh, T.; Asahi, T.; Masuhara, H. Appl. Phy. Lett. 2001, 79, 1667-1669.

39 Link, S.; El-Sayed, M.A. Annu. Rev. Phys, Chem. 2003, 54, 331-366.

40 (a) Govorov, A.O.; Zhang, W.; Skeini, T.; Richardson, H.; Lee, J.; Kotov, N.A. Nanoscale Res Lett 2006, 1, 84-90. (b) Govorov, A.O.; Richardson, H.H. NanoToday 2007, 2, 30-38.

41 Huang, X.; Jain, P.K.; El-Sayed, I.H.; El-Sayed, M.A. Photochemistry and Photobiology 2006, 82, 412-417.

42 (a) Sperling, R.A.; Gil, P.R.; Zhang, F.; Zanella, M.; Parak, W.J. Chem. Soc. Rev. 2008, 37, 1896-1908. (b) Wilson, R. Chem. Soc. Rev. 2008, 37, 2028-2045. (c) De, M.; Ghosh, P.S.; Rotello, V.M. Adv. Mater. 2008, 20, 1-17. (d) Cai, W.; Gao, T.; Hong, H.; Sun, J. Nanotechnology, Science and Applications 2008, 1, 17-32.

43 Zhao, W.; Brook, M.A.; Li, Y. ChemBioChem 2008, 9, 2363-2371.

44 Storhoff, J.J.; Lazarides, A.A.; Mucic, R.C.; Mirkin, C.A.; Letsinger, R.L; Schatz, G.C. J. Am. Chem. Soc. 2000, 122, 4640-4650.

45 Elghanian, R.; Storhff, j.J.; Mucic, R.C.; Letsinger, R.L.; Mirkin, C.A. Science 1997, 277, 1078-1081.

46 Medley, C.D.; Smith, J.E.; Tang, Z.; Wu, Y.; Bamrungsap, S.; Tan, W. Anal. Chem. 2008, 80, 1067-1072.

47 (a) Hirsch, L.R.; Halas, N.J.; West, J.L. Proceedings of the Second Join EMBS/BMES Conference 2002, Houston, TX, USA. (b) Hirsch, L.R.; Jackson, J.B.; Lee. A.; Halas, N.J.; West, J.L. Anal. Chem. 2003, 75, 2377-2381.

48 (a) Taton, T.A.; Mirkin, C.A.; Lestinger, R.L. Science 2000, 289, 1757-1760. (b) Stoeva, S.I.; Lee, J.-S.; Smith, J.E.; Rosen, S.T.; Mirkin, C.A. J. Am. Chem. Soc. 2006, 128, 8378-8379. (c) Goluch, E.D.; Nam, J.-M.; Georganopoulou, D.G.; Chiesl, T.N.; Shaikh, K.A.; Ryu, K.S.; Barron, A.E.; Mirkin C.A.; Liu, C. Lab on a Chip 2006, 6, 1293-1299.

49 Vance, F.W.; Lemon, B.I.; Hupp, J.T. J. Phys. Chem. B 1998, 102, 10091-10093.

50 Ray, P.C. Angew. Chem. Int. Ed. 2006, 45, 1151-1154.

51 Jiang, Z.; Sun, S.; Liang, A.; Huang, W.; Qin, A. Clin. Chem. 2006, 52, 1389-1394.

52 Liu, R.; Liew, R.; Zhou, J.; Xing, B. Angew. Chem. Int. Ed. 2007, 46, 8799-8803.

53 Du, B.-A.; Li, Z.-P.; Liu, C.-H. Angew. Chem. Int. Ed. 2006, 45, 8022-8025.

54 Gao, J.; Liu, D.; Wang, Z. Anal. Chem. 2008, in press.

55 http://tools.invitrogen.com/content/sfs/manuals/superscriptdirect_rls_man.pdf

56 Xie, H.; Gill-Sharp, K.L.; O'Neal, D.P. Nanomedicine: Nanotech. Bio. Medi. 2007, 3, 89-94.

57 El-Sayed, I.H.; Huang, X.H.; El-Sayed, M.A. Nano Lett. 2005, 5, 829-834.

58 Hirsh, L.R.; Stafford, R.J.; Bankson, J.A.; Sershen, S.R.; Rivera, B.; Price, R.E.; Hazle, J.D.; Halas, N.J.; West, J.L. PNAS, 100, 13549-13554.

59 El-Sayed, I. H.; Huan, X.; El-Sayed, M.A. Cancer Lett. (2006) 239, 129-135.

60 Au, L.; Zheng, D.; Zhou, F.; Li, Z.-Y.; Li, X.; Xia. Y. ACS Nano 2008, 2, 1645-1652.

CHAPTER 2. KINETIC STUDY OF GOLD NANOPARTICLE GROWTH IN SOLUTION BY BRUST-SCHIFFRIN REACTION

2.1 Introduction

GNPs represent one of the most extensively studied nanomaterials because of their many unique size- and aggregation-dependent properties such as surface plasmon resonance, surface enhanced Raman scattering, quantized charging effect, etc.[1-3] A convenient wet chemical method to prepare GNPs is through Brust-Schiffrin reaction.[4,5] This reaction leads to thiolate monolayer-protected GNPs with sizes typically in the range of 1-5 nm. The size of the nanoparticles can be controlled by adjusting the ratio of thiol ligands and gold salts in the reaction mixture, the reaction conditions,[5] or by post-synthesis thermal annealing treatment.[6,7] The thiolate-protected GNPs exhibit good solubility in a wide range of solvents, and are sufficiently stable for most application purposes. Therefore, alkanethiol monolayer-protected GNPs have gained significant attention since its first report.

However, despite the extensive use of Brust-Schiffrin reaction for gold nanoparticle synthesis, many aspects of this reaction are still not well understood. One of the remaining significant challenges in nanoparticle synthesis is the precise control of nanoparticle size and size distribution. This problem arises from the rather complicated kinetics and thermodynamics of the nanoparticle growth in solution.[8-12] In general, a nanoparticle growth in solution includes three basic steps: nucleation, core size expansion, and passivation.[13] As for Brust-Schiffrin reaction, this reaction involves a multi-step process:[5,13] First, in the presence of thiol ligands, Au (III) is reduced to Au(I) by oxidizing thiols to disulfides. If more than 2 equiv of thiols are present, the resulting

Au(I) and excess thiol will combine into a polymeric Au(I)-thiolate complex. In the presence of sodium borohydride, all Au(I) are reduced to gold atoms. The free gold atoms quickly coalesce together into small nuclei. Free gold atoms are then continuously added to the existing nuclei or small nanoparticles coalesce together into larger particles. The role of thiol ligands in this reaction is to passivate nanoparticle growth and to protect the so-formed nanoparticles from aggregation by forming an alkanethiolate monolayer on the nanoparticle surface.

$$AuCl_4^- + RSH \rightarrow (—Au^ISR—)_n \text{ (polymer)} \quad (2\text{-}1)$$

$$(—Au^ISR—)_n + NaBH4 \rightarrow Au_x(SR)_y \quad (2\text{-}2)$$

Among all the steps involved in this reaction, each step alone poses significant challenges for kinetic study. The nucleation process often occurs extremely fast and cannot be easily monitored by commonly available instrumentation techniques. For the core size expansion stage, an important question is whether the incremental addition of gold atoms to the existing nuclei plays a dominant role or whether the coalescence of smaller nanoparticles into larger nanoparticles is the major expansion pathway.[14,15] Finally, the passivation of nanoparticle growth by thiol ligands is also a rather complicated issue. Despite the fact that the self-assembled monolayer process has been studied extensively,[16-21] the kinetics of thiol ligand adsorption onto gold substrates remains unclear in many cases. With the substrate dimension reduced from two-dimensional flat surface to highly curved three-dimensional nanosphere, the kinetic study of thiol adsorption to GNPs becomes even more challenging.[22-24]

As a first step leading to a further understanding of nanoparticle growth in solution, we designed and conducted a simplified experiment to study the kinetics of

Brust-Schiffrin reaction. Recently, it was reported by Murray and coworkers that ultra small gold nanoclusters with diameters below 1 nm could be synthesized by the addition of large excess amount of thiol ligands or under very low temperature reaction condition.[25] The purpose of large excess amount of thiol ligands is to increase the passivation speed of thiol ligands so that the nanoparticle growth can be stopped at a very early stage. Referring to this concept, we conducted the following experiment. Using the conditions as reported in Murray's work,[5] a room temperature Brust-Schiffrin reaction was set up using one to one ratio of 1-butanethiol ligands versus gold salt. After the addition of reducing agent, sodium borohydride, a portion of the reaction mixture was taken out from time to time and added with approximately 300 fold excess of more butanethiol. The reaction was continued for another one hour to allow completion of the reaction. The purpose for adding large excessive thiol ligands to the reaction mixture was to increase the adsorption rate of thiol ligands to the nanoparticles, so as to stop the nanoparticle growth effectively at different reaction stages. In this way, we can exclude or minimize the kinetic effect of thiol ligands adsorption on nanoparticle growth and obtain a better picture on the nucleation and core size expansion stages. Following the experimental study, two kinetic models were proposed to explain the kinetic behavior of Brust-Schiffrin reaction. Both models showed a fairly good fit with the experimental data, with one model revealing more detailed information on nanoparticle growth mechanism.

2.2 Materials and Methods

2.2.1 Chemicals, solvents and materials

All Solvents and organic chemicals (ACS Reagents) were purchased from Aldrich (Milwaukee, WI) or VWR (West Chester, PA) except for the hydrogen

tetrachloroaurate(III) hydrate ($HAuCl_4$), which was purchased from Strem Chemicals (Newburyport, MA).

2.2.2 Synthesis of butanethiolate-protected GNPs ($_{Bt}$GNP)

Butanethiolate-protected GNPs ($_{Bt}$GNP) were synthesized according to the Brust-Schiffrin reaction.[4,5] All the reactions were conducted at room temperature. Briefly, tetraoctylammonium bromide (1500 mg, 2.74 mmol, 2.5 equivalents) was stirred vigorously in 80 ml toluene in a 500 mL round bottom flask. $HAuCl_4 \cdot xH_2O$ (310 mg, 0.912 mmol, 1 equivalent) in 25 mL deionized water was added. As the $AuCl_4^-$ was transferred from the aqueous phase to the organic phase, the solution changed from a bright yellow to a red-brown color. The organic phase was separated and 1.1 equiv. of 1-butanethiol (74.9 mg, 0.832 mmol) was added to the solution. The solution was stirred at room temperature for 10 min followed by the addition of $NaBH_4$ (380 mg, 7.84 mmol, 10 equivalents) in 25 ml deionized water over 10 s. The resulting solution quickly turned dark black. Following the complete addition of $NaBH_4$, 10 mL aliquots were removed from the reaction solution at time intervals of: 1, 2, 3, 5, 10, 30 60, and 180 min and added to a separate flask followed by the addition of 3 mL 1-butanethiol (2.526 g, 28.00 mmol). Each reaction was allowed to continue for 1 h at room temperature with continuous stirring. Nanoparticles were collected by removing the solvent using a rotary evaporator under vacuum at 48°C. The dark nanoparticle product was then purified by successive washing with 25 mL of ethanol and centrifugation. After four to five times of washing, the residual ethanol was blown off using a stream of nitrogen gas and the $_{Bt}$GNPs were dispersed in dichloromethane for size analysis.

2.2.3 Particle size analysis

For TEM analysis, approximately 1 □ L of sample in dichloromethane was added on a 300 mesh Formvar-coated copper grid using an Eppendorf micropipette and immediately wicked off using filter paper. After allowing the sample to air dry for 5-10 min, images were obtained using a JEOL 100CX transmission electron microscope at 80 keV. The average particle core diameter D and standard deviation σ were determined according to equation (2-3) and (2-4) from the analysis of 100 particles randomly appeared on TEM image. The diameters were measured using a LUPE 30X magnifier (Ted Pella Inc. CA) with a built-in ruler.

$$\overline{D} = \frac{\sum_{i=1}^{r} N_i \times D_i}{\sum_{i=1}^{r} N_i} \tag{2-3}$$

$$\sigma = \sqrt{\frac{\sum_{i=1}^{i=r} (D_i - \overline{D})^2}{N-1}} \tag{2-4}$$

2.3 Results and Discussions

2.3.1 Average core diameter

According to the previous work by Hostetler et al,[5] using a one-to-one ratio of thiol ligands versus gold salt and a room temperature reaction condition, nanoparticles with approximately 2 nm core diameters can be obtained as the major product. We have also used this condition routinely in our own lab to synthesize butanethiolate-protected nanoparticles.[26-29] Therefore we chose this condition as an example in our kinetic study. After the extraction of gold salt into organic solvent using tetraoctylammonium bromide and immediately following the addition of sodium borohydride into the solution, aliquots of the reaction mixture were taken out after 1, 2, 3, 5, 10, 30, 60, and 180 minutes of

reaction and added to approximately 300-fold excess of additional butanethiol ligand. At the end of the reaction, each product was collected and purified by washing and centrifugation. Each sample was characterized by a transmission electron microscope and the average size and size distribution of each product were analyzed according to the method described in the experimental section.

Table 2- 1. Average core diameter (*d*), standard deviation (σ), and number of Au atoms per particle (*N*) of nanoparticles collected at different reaction stages

	Batch 1			Batch 2			Batch 3		
t (min)	*d* (nm)	*σ (nm)*	*N*	*d* (nm)	*σ (nm)*	*N*	*d* (nm)	*σ (nm)*	*N*
1	2.10	0.29	286	2.26	0.35	355	2.36	0.47	403
2	2.48	0.35	469	2.29	0.38	375	2.35	0.38	400
3	-	-	-	2.41	0.36	426	2.45	0.40	453
5	2.43	0.35	442	2.48	0.36	467	2.48	0.36	467
10	2.60	0.37	541	2.56	0.34	516	2.60	0.33	541
30	2.45	0.33	450	2.54	0.34	504	2.33	0.41	387
60	2.58	0.28	527	2.19	0.36	325	2.38	0.38	415
180	2.59	0.57	534	2.21	0.31	330	2.39	0.38	420

This experiment was repeated three times. The average diameters of each nanoparticle product collected at different reaction times were summarized in Table 2-1 and Figure 2-1. From the comparison of these three experimental data sets, there are three results to be noticed: first, from one batch of sample to the other batch of sample, the average diameter of the nanoparticles under the same reaction conditions varies significantly. In other words, the reproducibility of Brust-Schiffrin reaction for the synthesis of GNPs in the range of 2 nm is very poor. As a matter of fact, we have noticed such poor reproducibility in our extensive previous studies.[26-29] Second, despite the large variation of nanoparticle size from one batch of synthesis to the other, it was observed that the nanoparticles core diameter exhibited a general trend of fast increase within a few

minutes of reaction time and all three samples reached a maximum average core diameter of 2.6 nm after 10 minutes of reaction. At a reaction time of one minute, the nanoparticle diameter has already increased to more than 2 nm. Third, after the nanoparticle size reached this maximum value, the nanoparticle size either decreased or remained at this maximum value with elongated reaction time. The average diameter of nanoparticles obtained after three hours of reaction is around 2.2 nm.

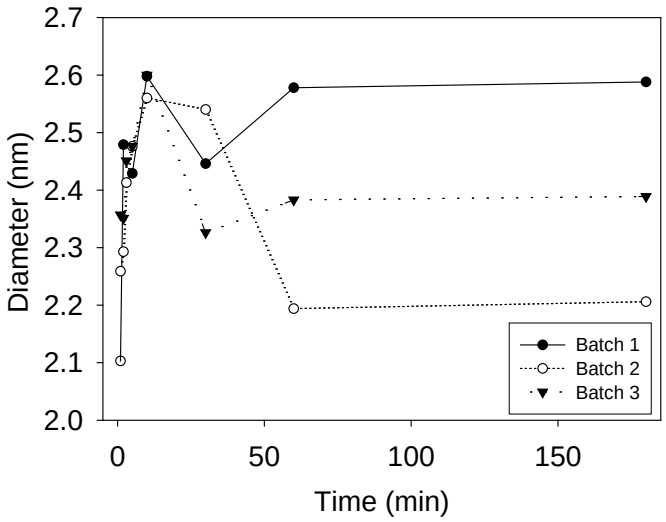

Figure 2- 1. Diagram of nanoparticle average core diameter change over reaction time. (Copyright ® 2006 American Scientific Publishesr)

The poor reproducibility of Brust-Schiffrin synthesis is due to the rather complicated kinetics of this reaction.[5, 8-13] First of all, this reaction is an inhomogeneous two-phase reaction (water plus toluene), which means that the stirring speed has a great effect on the reaction kinetics. Second, it was also noticed that the rate of addition of reducing agents in solution could affect the concentration of nuclei formed in solution,[12] therefore, the size of the nanoparticle product. Third, the nucleation is a fast process and any slight variation of the experimental condition such as stirring speed of the reaction

solution could change the nuclei concentration, so as to the size of the nanoparticles dramatically. A very small experimental error from the reagent concentration could also bring such dramatic effects. This poor reproducibility makes the scale up for industrial production of nanoparticles using Brust-Schiffrin reaction very challenging.

Although the variation of nanoparticle size from one sample to the other is large, one can still see a general trend of rapid size increase within 10 minutes of reaction time. From the data collected here, it is difficult to judge when the nucleation process started. Because of the very rapid size increase, it is difficult to control the nanoparticle size at this stage of reaction. However, it is interesting to note that all three samples reached the same maximum diameter of 2.6 nm at 10 minutes of reaction time. This suggests that the maximum nanoparticle size in a Brust-Schiffrin reaction is mainly determined by the ratio of chemical agents used in the study, but not much affected by the specific reaction conditions. After reaching the maximum size, the nanoparticles either remained at this size or even decreased. It is unclear at this time what is the exact mechanism behind the size decrease, however, we believe this is possibly due to the etching effect of thiol ligands, as pointed in some previous reports.[30-32] Because of the rather complicated nature of self-assembled monolayer formation on three-dimensional nanocluster surface, the mathematic modeling study described in this paper will not address this effect.

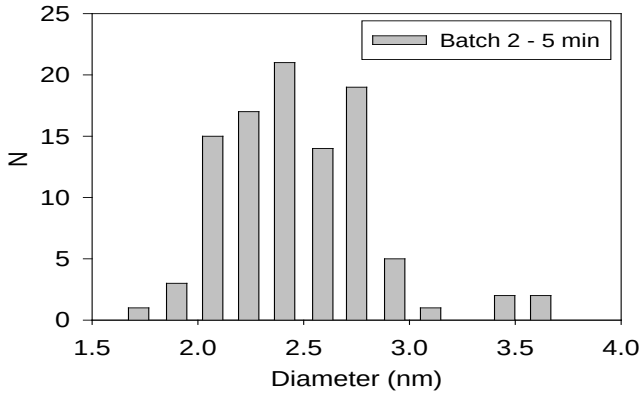

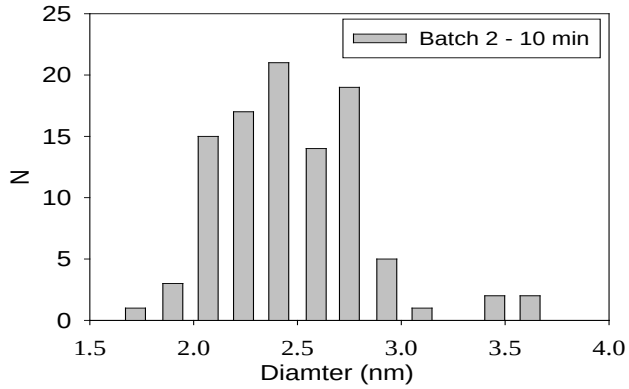

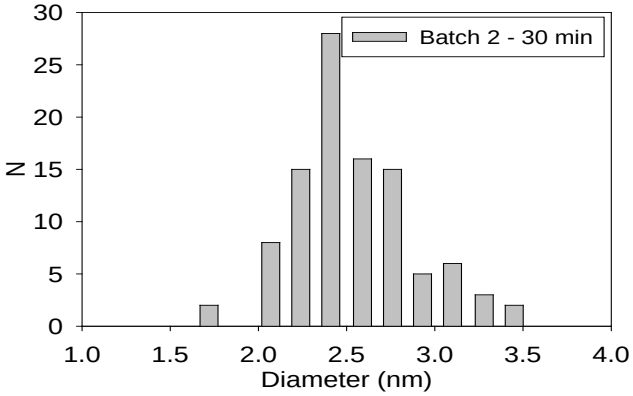

Figure 2- 2. The particle size distributions of batch 2 synthesis product obtained after (a) 5 minutes, (b) 10 minutes, and (c) 30 minutes of reaction time. (Copyright ® 2006 American Scientific Publishesr)

2.3.2 Nanoparticle polydispersity

The polydispersity of each nanoparticle sample collected at reaction time of 5, 10 and 30 minutes was analyzed and summarized in Table 2-1 and Figure 2-2. Only the

results from batch 2 synthesis are shown here. Essentially, it was noticed that the polydispersity for all the samples collected at different reaction time intervals and from different batches of synthesis is approximately 14%. Different from the average core diameter of the nanoparticles, the polydispersity of the nanoparticle product is much less affected by the conditions applied to the reaction, such as stirring speed, the addition rate of reducing agents, the concentration of each agents, etc. A statistical model governed by a certain nanoparticle growth mechanism such as coalescence of smaller nanoparticles into larger ones may play a more important role in polydispersity property of nanoparticle product grown in solution.

2.3.3 Kinetic modeling study

We used two kinetic models in this work to explain the observed experimental results. The first one was proposed by Hiramatsu et al. based on the synthesis of oleylamine-protected GNPs.[10] In this model, the nanoparticle growth is expressed as the $AuCl_4^-$ concentration change that follows a first-order kinetic. This model also assumes a constant gold nanoparticle concentration throughout the whole reaction, which was estimated from the maximum size of nanoparticles in the final product. The number of gold atoms in a nanoparticle at a give reaction time is:

$$n(t) = \frac{\left[AuCl_4^-\right]_0 \left(1 - e^{-kt}\right)}{\left[AuNP\right]} \tag{2-5}$$

$[AuCl_4^-]_0$ is the initial concentration of gold salt or gold atom concentration. [AuNP] is the concentration of GNPs, also nanoparticle nuclei concentration at any given reaction time.

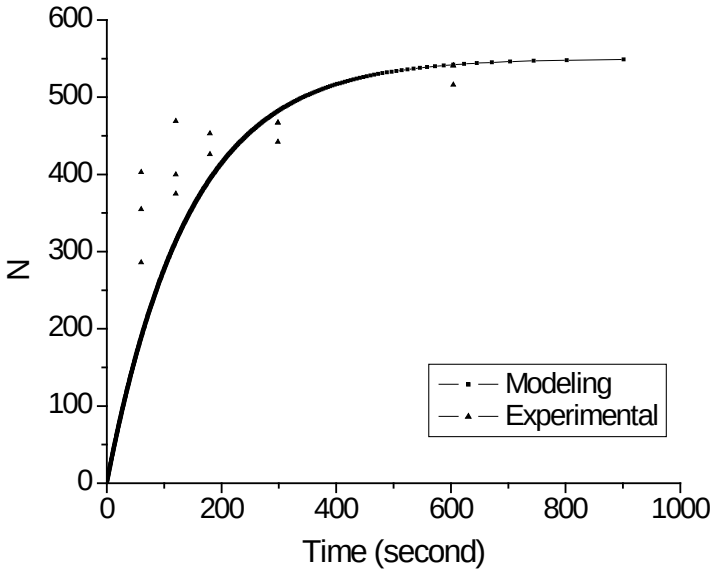

Figure 2- 3. Non-linear regression fitting curve from kinetic equation (5) with respect to experimental data. (k=0.007s^{-1}) (Copyright ® 2006 American Scientific Publishesr)

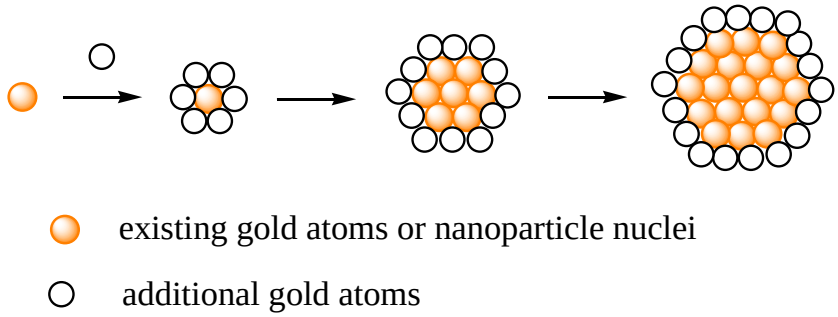

Figure 2- 4. The incremental addition model of nanoparticle growth process

We used the implementation of non-linear regression found in the software program MATHEMATICA for the curve fitting. This implementation uses the Levenberg-Marquart gradient search method to find the least squares minimum for the model.[33] The fitting result of this model to the experimental results is shown in Figure 2-3. In the graph, the experimentally obtained average diameters of nanoparticles were converted to number of gold atoms by assuming a spherical geometry as shown in Figure

2-4.[34,35] The *k* value obtained from this fitting is 0.007s^{-1}. The 95% confidence interval for the value of k is (0.0058, 0.0082). For the fitting, the F-statistics is 161.58, which yields a p-statistic value[36] less than 0.00001, an indication of good non-linear regression fitting. Although this model fits well into the experimental results, it does not provide more detailed information on the mechanism of nanoparticle growth. For example, this model cannot tell whether nanoparticles grow mainly by incremental addition of gold atoms to the existing nuclei or by coalescence of smaller nanoparticles into larger ones. This model also failed to identify and explain the nucleation process. To obtain a further understanding on these questions, we proposed a second kinetic model by assuming that a nanoparticle grows by incremental addition of gold atoms to existing nuclei as shown in Figure 2-4. The concentration of nuclei remains constant throughout the reaction. In this case, the number of gold atoms in a nanoparticle at any reaction time can be expressed in equation (2-6):

$$\frac{dn}{dt} = kn^{2/3}\left(\left[AuCl_4^-\right]_0 - [AuNP]n\right) \tag{2-6}$$

$$t = \frac{1}{6a^{2/3}b^{1/3}k}\left(3\ln\left(\frac{a^{2/3}+a^{1/3}b^{1/3}n^{1/3}+b^{2/3}n^{2/3}}{a^{2/3}-2a^{1/3}b^{1/3}n^{1/3}+b^{2/3}n^{2/3}}\right)+6\sqrt{3}Arc\tan\left(\frac{1+\frac{2b^{1/3}n^{1/3}}{a^{1/3}}}{\sqrt{3}}\right)-\pi\sqrt{3}\right)$$

$a = [AuCl_4^-]_0$ $\qquad$ $b = [AuNP]$ $\qquad$ (2-7)

The number of gold atoms added to an existing nanoparticle nuclei per unit time is related to the concentration of gold atoms in solution, which is $[AuCl_4^-]_0$-[AuNP]*n*, and the number of reactive sites on an existing gold nanoparticle surface. The number of reactive sites is roughly equivalent to the number of gold atoms on the surface, which is equivalent to $\rho n^{2/3}$ (ρ is a constant), assuming a nearly spherical structure of the

nanoparticle core. Here *k* is the product of reaction rate constant and ρ, therefore, is also a constant. The solution of this kinetic equation is given in equation (2-7).

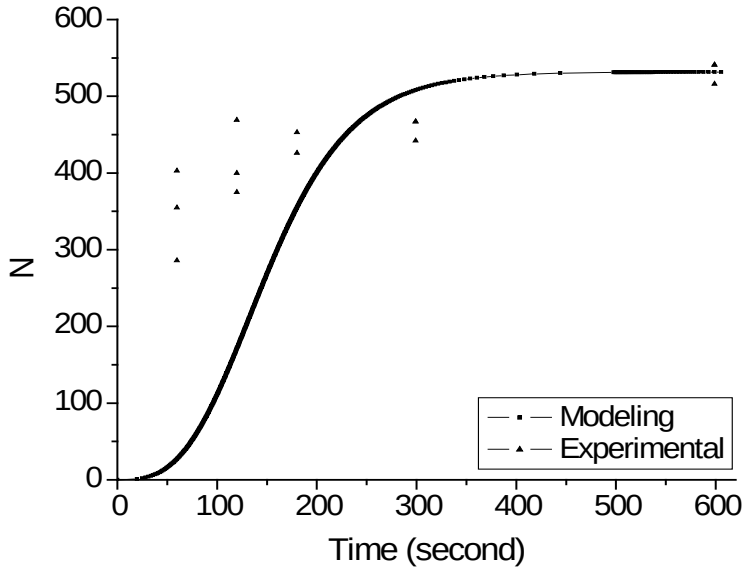

Figure 2- 5. Non-linear regression fitting curve from kinetic equation (6) with respect to experimental data. (*k*=15.2712, *a*= 0.01 M, *b*= 0.000018812 M) (Copyright ® 2006 American Scientific Publishesr)

The value of *a* was set at 0.01 M, as used in the experiment. The non-linear regression found in the software program MATHEMATICA was used to find the optimum values for *b* and *k*. The value obtained for *b* from curve fitting was 0.000018812 M and the value obtained for k was 15.2712. The fitting curve and the experimental data are shown in Figure 2-5. The 95% confidence interval for b is (0.000018465, 0.000018497). The 95% confidence interval for *k* is (9.9416, 20.6008). The F-statistic for this model is 44.2477, which provides a p value for the F-distribution of less than 0.00001. This indicates a relatively good fit of the model to the data. Experimentally, the *b* value, the concentration of GNPs, was found to be 0.0000181 M, very close to the results obtained by the model.

The good fitting between the model and the experimental data indeed suggests that incremental addition of gold atoms onto existing nanoparticle nuclei is likely a major pathway for nanoparticle growth. At later stage of the reaction, nanoparticle-nanoparticle aggregation and coagulation may start to present a significant effect on the growth process. It is interesting to note that the incremental addition model proposed here reveals clearly a “nucleation” stage of the nanoparticle growth (Figure 2-5). The time for nuclei formation was found to be around 10-20 seconds according to the model. Within 20 seconds, the rate of nanoparticle growth is almost zero. After about 50 seconds, the nanoparticle starts to grow rapidly. The mechanism for nucleation is due to or at least partially associated with the number of surface sites available for addition of more gold atoms. Since gold atoms coalesce together by van der Waals interactions, a larger surface area will attract more gold atoms to the nanoparticle surface per unit time.

2.4 Conclusion

In summary, we conducted both experimental and modeling studies to understand the nanoparticle growth kinetics in solution. These studies revealed and confirmed that the reproducibility of Brust-Schiffrin reaction for the synthesis of GNPs with diameter around 2 nm is rather poor due to the intrinsic complexity of this two-phase reaction. Although it is unlikely that a single mathematical model can be found to explain the kinetics of such complex reaction, the incremental addition model proposed in our study revealed some important information on the nucleation and growth stage. From this study, we also conclude that in order to gain a more comprehensive understanding on wet chemical synthesis of nanoparticle materials, it is important to first disseminate and examine the different stages of nanoparticle growth separately and then collectively. With

Brust-Schiffrin reaction being used extensively for gold nanoparticle synthesis, a full understanding of this process is critical for both fundamental research as well as mass production of nanoparticle materials for practical applications.

References:

1 Schmid, G. Clusters and Colloids: From Theory to Applications 2004, VCH, New York.

2 Templeton, C.; Wuelfing, M. P.; Murray, R. W. Acc. Chem. Res. 2000, 33, 27.

3 Daniel, M.-C.; Astruc, D. Chem. Rev. 2004, 104, 293.

4 Brust, M.; Walker, M.; Bethell, D.; Schiffrin, D.J.; Whyman, R. J. Chem. Soc., Chem. Comm. 1994, 7, 801.

5 Hostetler, M.J.; Wingate, J.E.; Zhong, C.-J.; Harris, J.E.; Vachet, R.W.; Clark, M.R.; Londono, J.D.; Green, S.J.; Stokes, J.J.; Wignall, G.D.; Glish, G.L.; Porter, M.D.; Evans, N.D.; Murray, R.W. Langmuir 1998, 14, 17.

6 Maye, M.M.; Zheng, W.; Leibowitz, F.L.; Ly, N.K.; Zhong, C-J. Langmuir 2000, 16, 490.

7 Teranishi, T.; Hasegawa, S.; Shimitzu, T.; Miyake, M. Adv. Mater. 2001, 13, 1699.

8 Shimmin, R.G.; Schoch, A.B.; Braun, P.V. Langmuir 2004, 20, 5613.

9 Wilcoxon, J.P.; Provencio, P.P. J. Am. Chem. Soc. 2004, 126, 6402.

10 Hiramatsu, H.; Osterloh, F.E. Chem. Mater. 2004, 16, 2509.

11 Yang, C.-S.; Awschalom, D.D.; Stucky, G.D. Chem. Mater. 2001, 13, 594.

12 Bullen, C.R.; Mulvaney, P. Nano. Lett. 2004, 4, 2303.

13 Chen, S.; Templeton, A.C.; Murray, R.W. Langmuir 2000, 16, 3543.

14 José-Yacamán, M.; Gutierrez-Wing, C.; Miki, M.; Yang, D.-Q.; Piyakis, A.N.; Sacher, E. J. Phys. Chem. B 2005, 109, 9703.

15 Iijima, S.; Ajayan, P.M. J. Appl. Phys. 1991, 70, 5138.

16 Camillone, N. III. Langmuir 2004, 20, 1199.

17 Bain, C.D.; Troughton, E.B.; Tao, Y-T.; Evall, J.; Whitesides, G.M.; Nuzzo, R.G. J. Am. Chem. Soc. 1989, 111, 321.

18 Schneider, T.W.; Buttry, D.A. J. Am. Chem. Soc. 1993, 115, 12391.

19 Kim, H.J.; Kwak, S.; Kim, Y.S.; Seo, B.I.; Kim, E.R.; Lee, H. Thin Solid Films 1998, 191, 327-329.

20 Karpovich, D.S.; Blanchard, G.J. Langmuir 1994, 10, 3315.

21 Pan, W.; Durning, C.J.; Turro, N.J. Langmuir 1996, 12, 4469.

22 Humbert, C.; Busson, B.; Abid, J.-P.; Six, C.; Girault, H.H.; Tadjeddine, A. Electrochimica Acta 2005, 50, 3101.

23 Choo, H.; Cutler, E.; Shon, Y.-S. Langmuir 2003, 19, 8555.

24 Pradeep, T.; Sandhyarani, N. Pure Appl. Chem. 2002, 74, 1593.

25 Jimenez, V.L.; Georganopoulou, D.G.; White, R.J.; Harper, A.S.; Mills, A.J.; Lee, D.; Murray, R.W. Langmuir 2004, 20, 6864.

26 Dai, Q.; Worden, J.G.; Trullinger, J.; Huo, Q. J. Am. Chem. Soc. 2003, 127, 8008.

27 Worden, J.G.; Dai, Q.; Shaffer, A.; Huo, Q. Chem. Mater. 2004, 16, 3746.

28 Shaffer, A.; Worden, J.G.; Huo, Q. Langmuir 2004, 20, 8343.

29 Worden, J.G.; Shaffer, A.W.; Huo, Q. Chem. Comm. 2004, 518.

30 Schaaff, T.G.; Whetten, R.L. J. Phys. Chem. B 1999, 103, 9394.

31 Wilcoxon, J.P.; Provencio, P. P. J. Phys. Chem. B 2003, 107, 12949.

32 Prasad, B.L.V.; Stoeva, S.I.; Sorensen, C.M.; Kladunde, K.J. Chem. Mater. 2003, 15, 935.

33 Ratkowsky, D.A. Handbook of Nonlinear Regression Models 1990, Marcel Dekker.

34 The number of gold atoms is obtained from the diameter of the nanoparticle according to the following equation:

$$\frac{4}{3}\pi\left(\frac{d}{2}\right)^3 = N\frac{M}{\rho}$$

(where d is the particle diameter, N is the number of gold atoms, M is the atomic weight of gold and ρ is the Au density.)

35 Although typical GNPs exhibit truncated octahedron crystalline structures with certain “magic” numbers of gold atoms in the core, we found that the spherical geometry treatment gives very similar number of gold atoms in a nanoparticle as the one predicted from the truncated octahedron crystalline structures.

36 Obtained from the online facility for the computation of p-values for the F-statistic at http://davidmlane.com/hyperstat/F_table.html

CHAPTER 3. A STUDY ON GOLD NANOPARTICLE SYNTHESIS USING OLEYLAMINE AS BOTH REDUCING AGENT AND PROTECTING LIGAND

3.1 Introduction

GNPs have promising application potentials in many fields, ranging from bioconjugate probes, sensors, electronics and optics, to photon-thermal energy converters, and catalysis.[1-5] Since the first synthesis of gold colloids 150 years ago,[6] there have been numerous methods developed for the wet chemical synthesis of gold nanoclusters, nanoparticles, and colloids.[7-9] To list a few, Turkevich et al used sodium citrate as the reducing agent to make citrate-stabilized GNP with size ranging from a few nanometers to tens of nanometers.[10] Brust and Schiffrin developed a two-phase reaction to prepare alkanethiolate-protected GNP with core size ranging from 2 to 5 nm.[11,12] Other than thiol ligands, other types of ligands have also been used extensively as capping agents for gold nanoparticle synthesis.[13-15] Recently, a study was reported on the use of an amine-borane complex as a mild reducing agent to make monodispersed gold and silver nanoparticles.[16] In spite of these extensive work, understanding on the mechanism and growth kinetics of nanoparticles under different chemical environment and conditions is still very limited. Such understandings are critical for the development of nanoparticles with controlled sizes, shapes and expectant properties.

Among the different methods for gold nanoparticle synthesis as mentioned above, we are particularly interested in amine compound-based gold nanoparticle synthesis. Gomez et al revealed that Au(I) complex could undergo decomposition with alkylamines and form amine-protected GNPs.[17] Osterloh et al. synthesized nearly monodispersed amine-protected gold and silver nanoparticles using an oleylamine ligand.[18] Aslam et al

recently reported the synthesis of an oleylamine (OA)-stabilized GNPs which were soluble in both water and organic solvents.[19] A significant difference between amine chemistry versus thiol chemistry-based synthesis is that amine ligands can serve as both the reducing agent and capping ligands for nanoparticle synthesis. This means amine-based gold nanoparticle synthesis can often be conducted in a single-phase reaction system. For thiol chemistry-based synthesis, an additional reducing agent other than thiol ligands, usually sodium borohydride, needs to be added to the reaction. Since sodium borohydride is only soluble in a polar solvent such as water and most thiol ligands are only soluble in nonpolar organic solvents such as toluene, thiol chemistry-based nanoparticle synthesis are often conducted on a two-phase reaction system, such as the case of Brust-Schiffrin reaction.[11,12] The kinetic control of a two-phase reaction is typically much more difficult than single-phase reactions. As revealed in one of our recent studies, the average core size of the nanoparticles synthesized using Brust-Schiffrin reaction varies significantly from batch to batch.[20] This difficulty poses significant challenges to the understanding of nanoparticle growth kinetics.

We herein report a mechanism and kinetic study of an oleylamine-protected gold nanoparticle growth using a procedure reported by Aslam et al.[19] Although this method was reported a few years ago, not much is understood on the growth process and the monolayer structure of the nanoparticles. The interesting aspect of this synthetic protocol is that the reaction is done using water as a single phase solvent: both gold salt and oleylamine were dissolved in water, and the product is soluble in both water and organic solvents. After the reaction, relatively monodispersed GNPs in the size range of tens of nanometers were obtained in high yield by precipitation. Because of the simplicity of the

procedure and the use of water as solvent, this reaction may become a very useful method for large scale commercial production of GNPs. From our study, we obtained important and detailed information on the nanoparticle growth process, as well as the chemical structural change of the amine ligands during the reaction. Our results lead to a different explanation on the protecting effect of oleylamine ligands on the nanoparticles than some reported studies. We also found for the first time that the nanoparticle growth kinetics follows a logistic model,[21] a model that has been used to explain many natural growth and decay processes.[22-24] Results obtained from our study will be valuable in assisting further design and synthesis of nanoparticle materials with controlled sizes and properties.

3.2 Experimental

3.2.1 Chemicals, solvents and materials

Oleylamine ($C_{19}H_{37}NH_2$; tech., 70%) and all solvents (ACS Reagents) were purchased from Aldrich (Milwaukee, WI) except for the hydrogen tetrachloroaurate (III) hydrate ($HAuCl_4 \cdot xH_2O$), which was purchased from Strem Chemicals (Newburyport, MA).

3.2.2 Synthesis and kinetic study of oleylamine-protected GNPs ($_{OA}$GNPs)

Nanoparticles were synthesized according to a reported procedure.[19] $HAuCl_4 \cdot xH_2O$ (51.5 mg, 0.15 mmol) was dissolved in 120 mL nanopure water and heated up to 80 ^oC. An aliquot of 2 mL yellow gold salt solution was taken out and UV-Vis spectrum of the solution was recorded immediately. Oleylamine (300 μL, 0.66 mmol) was then added to the solution and at time intervals of 5 s, 3, 6, 9, 12, 17, 22, 27, 32, 37, 42, 47, 52, 57, 62, 72, 82, 92, 102, 112, 122, 132, 142, 152, 162, 172, 182, 192, 202, 212 min following the addition, 2 mL of reaction mixture were taken out and UV-Vis spectra

were recorded from 200 to 800 nm for each sample at a scanning rate of 600 nm/min. To obtain the final product, after reacting for three hours, the reaction mixture was cooled down to room temperature and 300 mL of methanol was added to the solution to allow the product precipitate out. After placing the solution at room temperature for 24 hours, the product was collected by centrifugation, washing with copious amount of methanol and drying in air.

3.2.3 Infrared spectroscopy

The infrared spectrum of the nanoparticle product was recorded using a PerkinElmer Spectrum™ 100 FT-IR spectrometer with a universal ATR sampling accessory. Analyses were performed on solid samples deposited on a diamond coated ZnSe crystal (d = 1 mm) by evaporation of several drops of nanoparticle solution in toluene. A background was taken without sample deposited before each measurement.

3.2.4 Nuclear Magnetic Resonance (NMR)

^{1}H NMR spectra of free ligand oleylamine and $_{OA}$GNPs in $CDCl_3$ were obtained on a Varian Mercury 300 MHz spectrometer using a line-broadening factor of 1 Hz and relaxation delay of 1 s at pulse 45 degrees and an acquisition time of 1.997 s.

3.2.5 UV-Vis Spectroscopy

UV-Vis absorption spectra of the nanoparticle product and reaction intermediates were recorded on sample solution using a Cary 300 Bio double-beam UV-Vis spectrophotometer with a scan range of 200-800 nm and a 1 nm resolution. Sample cell used in the study was a 1 cm quartz curvette. All experimental data were corrected for water background absorption.

3.2.6 Transmission Electron Microscopy (TEM)

TEM images were obtained by a FEI TECNAI F30 electron microscope. The accelerating voltage during measurement was 300 keV. The 400 mesh carbon/formvar-coated copper grids were first treated with a poly-L-lysine (M.W. 93800, Sigma) solution (0.0381 g/mL in 1:3 H_2O: MeOH mixture solvents). TEM sample grids were then prepared by extracting 5 μL reaction solution from the reaction mixture after oleylamine addition at reaction time intervals of 1, 4, 7, 10, 15, 20, 25, 30, 35, 40, 60, 80, 100, 120, 140, 160 and 180 min, casting the solution onto polylysine treated grids and vacuum dried. ImageJ software was used to analyze the average size and size distribution of nanoparticles in TEM images for each sample.

3.2.7 Modeling of $_{OA}$GNPs growth kinetics by MATHEMATICA

The UV-Vis absorption spectra of nanoparticle intermediate product were further analyzed using Cary WinUV software and the reaction kinetic was modeled using the nonlinear regression functions of the Statistics package of the program *MATHEMATICA*.[25] For samples collected at different time intervals, the absorbance of the samples at the surface plasmon resonance band 530 nm were recorded. The absorbance of the reaction solution versus reaction time was plotted and the data was fitted with a logistic model using *MATHEMATICA*.

3.3 Results and Discussions

3.3.1. Monolayer structure of the $_{OA}$GNP

As described in the experimental section, the synthesis of GNPs in aqueous solution using oleylamine as both reducing agent and stabilization agent is an extremely simple protocol. After three hours of reaction at 80 ^{o}C, the nanoparticle product was collected by simple precipitation and washing. Different from what was reported by

Aslam et al.,[19] we found that after the nanoparticles were precipitated out from methanol, the nanoparticles lost their solubility in water. The dried nanoparticles have good solubility in THF, toluene, and relatively good solubility in dichloromethane. TEM analysis of the end reaction product revealed mainly spherical nanoparticles with an average core diameter around 9.5 nm, with a polydispersity around ± 1 nm. The reproducibility of this reaction is very good. The average core size of the nanoparticles from three different batches of synthesis is 9.5 ± 1.1 nm.

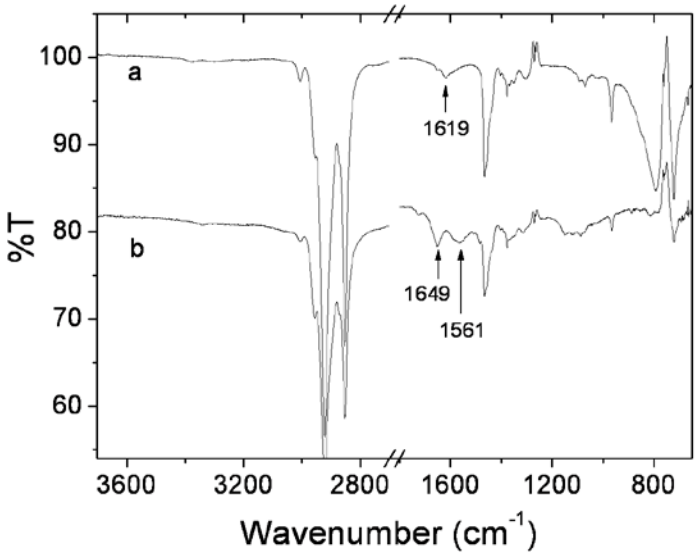

Figure 3- 1. IR spectra of (a) oleylamine and (b) oleylamide-protected GNPs. (Copyright ® 2007 American Scientific Publishers)

To better understand the nanoparticle growth and passivation by organic ligands, we first analyzed the ligand monolayer structure of the nanoparticles using FT-IR and NMR spectroscopy. Figure 3-1a and b are the IR spectra of neat oleylamine and $_{OA}$GNP product. The IR spectrum of oleylamine contains the following major bands: N-H stretch around 3380-3250 cm^{-1}, C-H stretch at 3100-2850 cm^{-1}, N-H bending at 1615 cm^{-1}, C-H bending at 1500-1300 cm^{-1}, and weak C-N stretch at 1100-1050 cm^{-1}. Two major

differences were observed from the IR spectrum of $_{OA}$GNP: the N-H bending of oleylamine at 1615 cm^{-1} disappeared, and two new peaks appeared at 1654 and 1567 cm^{-1}. These two peaks are representative vibration bands of amide bonds, as typically seen in the IR spectra of peptides and proteins.[26] The comparison of Figure 3-1a and b suggests that the amine group from free ligands was converted into amide when Au (III) was reduced to Au (I) or Au (0). Amide is an oxidized form of amine. In both Osterloh[18] and Aslam's[19] studies, the structural change of the oleylamine ligand during gold nanoparticle formation was not mentioned. However, Sun et al. discovered in a polyamine-induced gold nanoparticle formation that the amine groups were converted to amide groups.[27] Our finding not only corroborates with this reported study, but is also further supported by the NMR spectroscopic analysis as discussed in the following.

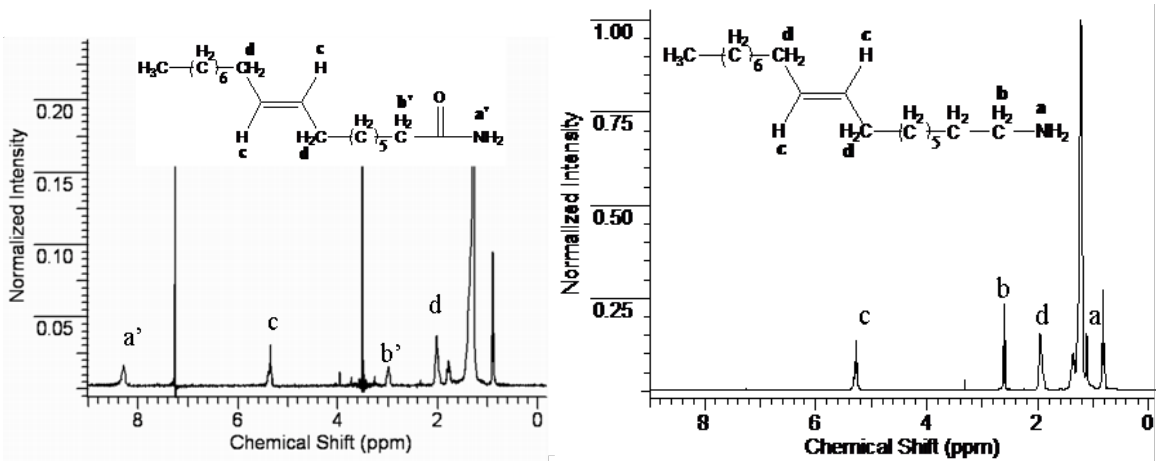

Figure 3- 2. NMR spectra of oleylamine (left) and oleylamide-protected GNPs (right). (Copyright ® 2007 American Scientific Publishers)

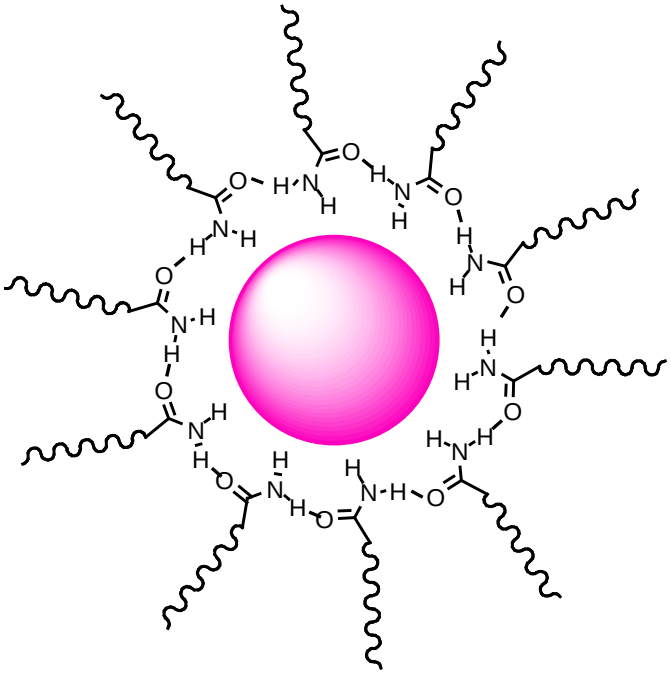

Figure 3- 3. The hydrogen bonding network formed between oleylamide ligands as a protecting layer on the GNPs. (Copyright ® 2007 American Scientific Publishers)

The ^{1}H NMR spectra of oleyamine and $_{OA}$GNP product are shown in Figure 3-2. The major peak assignment for pure oleylamine is the following: a small broad single peak at 1.13 ppm for N**H**$_2$, a triplet at 2.61 ppm for C**H**$_2$-NH$_2$, a multiplet at 1.37 ppm for C**H**$_2$-CH$_2$-NH$_2$, a triplet at 5.25 ppm for -C**H**=CH-, a quartet at 1.96 ppm for C**H**$_2$-CH=CH- and a triplet at 0.86 ppm for the C**H**$_3$ groups. In the spectrum of $_{OA}$GNP, a few major changes were observed: first, the N**H**$_2$ peak at 1.13 ppm disappeared and a new broad peak at 8.27 ppm appeared. The relative intensity of this new peak versus the C**H**$_3$ peak is about 2:3. It is known that the chemical shift of amide N**H**$_2$ is generally around 6 ppm. However, amides tend to form intermolecular hydrogen bonding in solid state, and the hydrogen bonding can cause the downfield shift of the proton NMR signal.[28] In addition to the direct observation of amide bond formation, a few other changes were also noticed to accompany this conversion: for example, a triplet at 2.61 ppm that belongs to

C**H**$_2$-NH$_2$ disappeared, and a new multiplet can be attributed to C**H**$_2$-CO-NH$_2$ appeared at 2.97 ppm. Judging from both NMR and FT-IR spectrum of $_{OA}$GNP, we believe that oleylamine was converted to oleylamide during nanoparticle formation and oleylamide ligands formed a complementary hydrogen bonding network around the gold nanoparticle surface as shown in Figure 3-3. The network formed a protective ligand monolayer to stabilize the nanoparticles. To further verify the existence of H-bonding network, 200 μL trifluoroacetic acids were added into 4 mL as-prepared $_{OA}$GNP water solution. Nanoparticles were instantly precipitated out of the solution. Trifluoroacetic acids destroyed the H-bonding network and destabilized the nanoparticles.

It was further noticed that each proton peak in the spectrum of $_{OA}$GNP, including the α proton next to the amide group, is rather sharp, suggesting that the amide groups are not directly complexed to the surface gold atoms. The oleylamide-protected gold nanoparticle is more like a nano-sphere floating inside a hydrophilic micelle-like compartment formed by oleylamide ligands. This is a distinct difference from thiol ligands-protected GNPs. As described in many reported studies, when thiol ligands are directly chemically bonded or complexed with surface gold atoms, the α proton NMR signals next to thiol groups are generally broadened significantly due to Knights shift or electromagnetic coupling interactions of the proton nuclei in close proximity to a metal surface.[29-32] The results observed from our study bear some significant differences from some reported studies, where it is believed that the amine ligands are bound on nanoparticle surface by weak covalent bonds or electrostatic interactions.[13, 33]

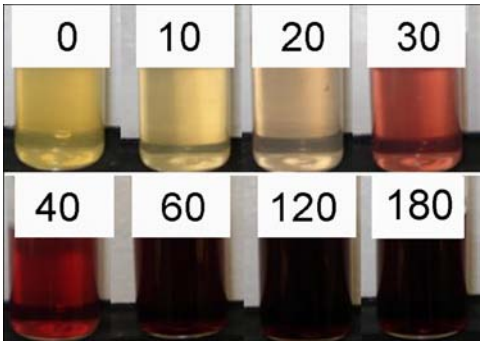

Figure 3- 4. Color change of the reaction solution observed during $_{OA}$GNPs growth at different reaction time (unit in minutes). (Copyright ® 2007 American Scientific Publishers)

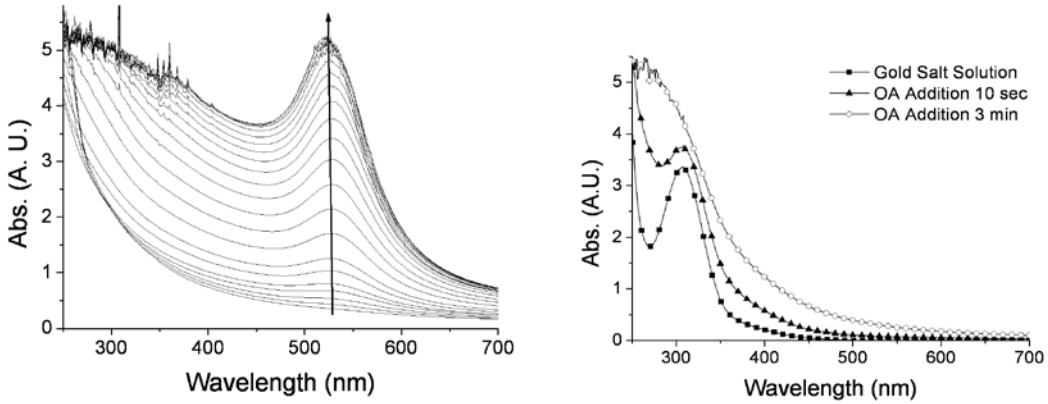

Figure 3- 5. (left) UV-Vis Spectra of gold salt $HAuCl_4 \cdot xH_2O$ solution in deionized water at 80 ^oC (-■-) and the reaction solution after oleylamine was added to the solution for 10 s (-▲-) and 3 min (-○-); (right) UV-Vis spectra of the reaction solution taken at different time from 32 to 212 min (time increased from 32 to 37, 42, 47, 52, 57, 62, 72, 82, 92, 102, 112, 122, 132, 142, 152, 162, 172, 182, 192, 202, 212 min along the arrow). (Copyright ® 2007 American Scientific Publishers)

3.3.2 Growth kinetics and mechanism study of the $_{OA}$GNP product

During the nanoparticle synthesis, a continuous color change was observed from the reaction solution as shown in Figure 3-4. The aqueous solution of gold salt is a bright yellow colored solution. After the addition of oleylamine, the solution immediately changed to light brown, and then to burgundy with increasing intensity throughout the reaction. UV-Vis absorption spectra of the reaction solution were recorded at very early stages of reaction and shown in Figure 3-5 (left). From the spectra, one can see that after

oleylamine was added to the solution, the absorption band of gold (III) salts at 320 nm disappeared very quickly. This is due to the complex formation of oleylamine with gold (III).[17,19] The UV-Vis spectra presented here confirmed that the complexation of oleylamine with Au (III) is a rather fast process. Within 1 minute of reaction time, the reduction and complexation should be completed. After the addition of oleylamine, the UV-Vis absorption spectra of the reaction solution was collected at different time intervals and presented in Figure 3-5 (right). From these spectra, one can see that at a reaction time of around 40 minutes, a surface plasmon resonance band appeared at 530 nm. The absorbance of the band continued to increase during the reaction. The wavelength of the SPR band did not show much significant shift during the reaction. From the absorbance increase of the SPR band, it is difficult to judge whether the increase was only due to the concentration increase of the nanoparticles or also reflected the size change of the nanoparticles. It is known that the SPR absorption of GNPs increases with increased size.[12]

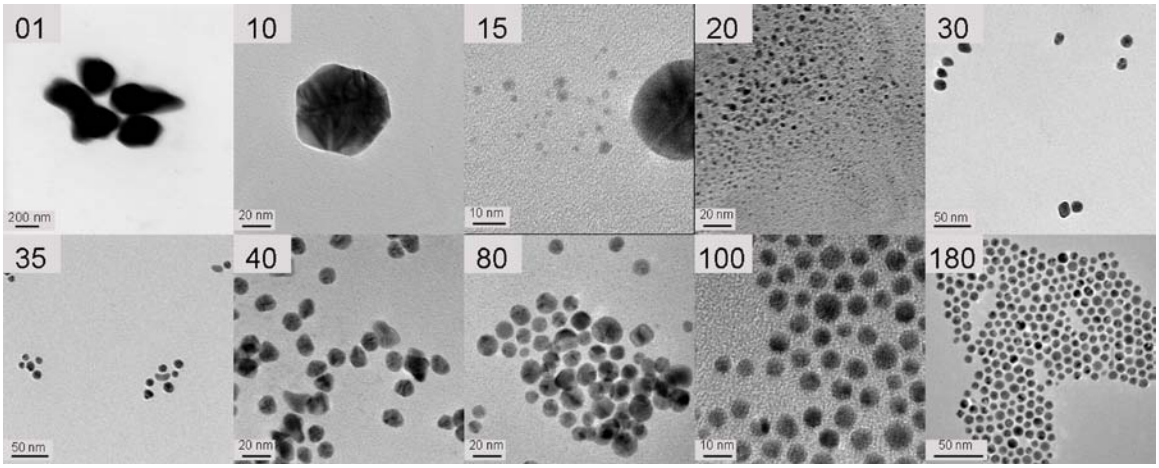

Figure 3- 6. Transmission electron microscopy images of intermediate product of gold nanoparticle growth collected at different reaction stages (unit in minutes, indicated in left-top corner for each one). (Copyright ® 2007 American Scientific Publishers)

To answer this question, we analyzed the reaction intermediate product using TEM. During the reaction, a small aliquot (~ 2 μL) of reaction mixture was taken out of the reaction flask and immediately deposited on formvar-coated copper grids. TEM images of reaction intermediates collected at different reaction stages are shown in Figure 3-6. At early stages of reaction, only very large non-spherical aggregates were observed. The size of the aggregates varies from a few hundreds of nanometers to even microns. The density of the aggregates appeared on the TEM grids was very scarce. After a few minutes of reaction, the size of the aggregates started to decrease, at the same time, some small particles (less than 1-3 nm) started to appear. At reaction time of around 20 min, all the large aggregates disappeared and only small particles were present. Then the small particles started to recombine together into larger nanoparticles with an average diameter around 10 nm. In the next 20 min of reaction time, we saw from the TEM images a large number of small particles (1-3 nm) and a very small amount of larger particles around 10 nm. At reaction time of about 40 minutes, the number of nanoparticles at 10 nm size range increased dramatically and the number of small particles decreased. Referring to the UV-Vis absorption spectroscopic study of the reaction solution, this is also the stage where one started to observe obvious Surface Plasmon Resonance (SPR) band in the UV-Vis absorption spectra. As the reaction continues, the number of nanoparticles at 9-10 nm size range in the reaction solution would continue to increase, as seen from Figure 3-5 at time 40, 80, 100 and 180 minutes. This result indeed suggests that the observed SPR band absorbance increase from the UV-Vis absorption spectra of the reaction solution was due to the increased concentration of GNPs in the size range of 10 nm, since GNPs less than 3

nm do not exhibit obvious SPR band.[12] It should be the case that small particles combined together into larger nanoparticles of which the final size was controlled by an equilibrium state. To summarize the results obtained from TEM and UV-Vis spectroscopic analysis, we believe the nanoparticle growth follows a process as outlined in Figure 3-7.

Referring to reported work,[17] the large aggregates formed at very early stage of the reaction should be an amine-Au (III) or amide-Au (I) or Au (0) complex. The disappearance of Au (III) salt absorption band at 340 nm at very early stage of the reaction also pointed out this possibility. The amine or amide-Au complex is a kinetically controlled product rather than a thermally stable product. Upon continuous heating, the thermally unstable complex was converted into thermally more stable nanoparticle product. The size of the final product of nanoparticles is determined by the stabilization effect of oleylamide ligands. Indeed, as noted by Aslam et al,[19] the average core size of the nanoparticles synthesized from this reaction can be tuned using different ratio of oleylamine ligands versus gold salt added to the reaction.

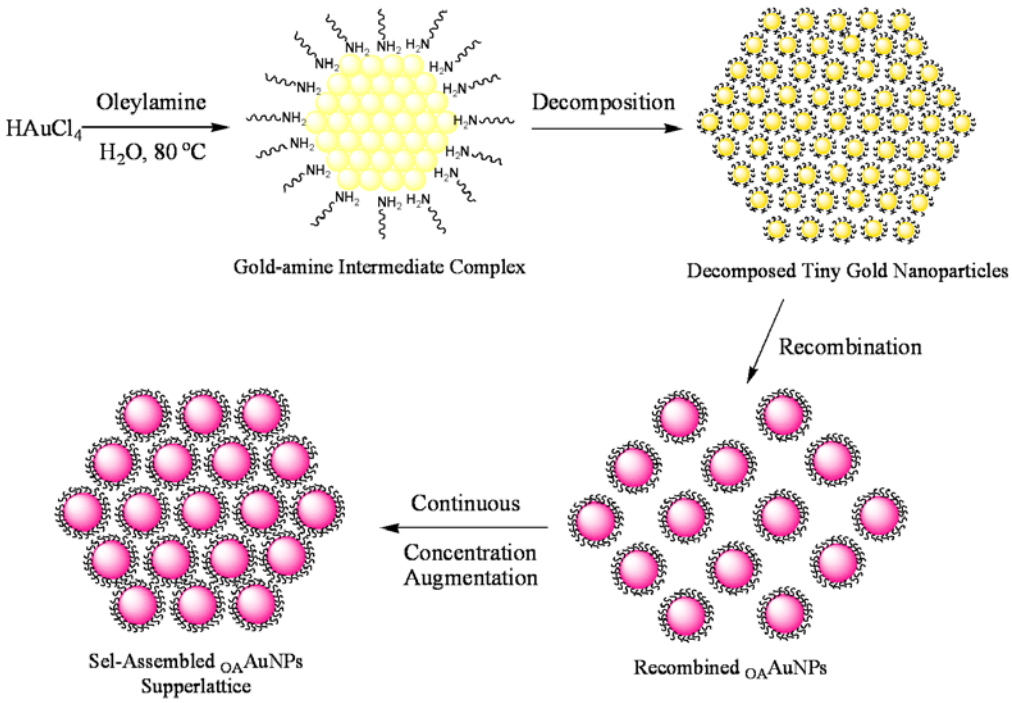

Figure 3- 7. An illustration of the gold nanoparticle formation process using oleylamine as both reducing and capping agents. (Copyright ® 2007 American Scientific Publishers)

3.3.3. Modeling of the nanoparticle growth kinetics

Using the UV-Vis absorption data presented in Figure 3-5, we plotted the absorbance change of the reaction solution at 530 nm versus reaction time as shown in Figure 3-8. At a glance, it appears that the SPR band absorbance increase of the reaction solution follows a well known mathematical model, the logistic model. The logistic model was first proposed by P. F. Verhulst[21] and has been found to be applicable to many scientific phenomena such as population dynamics.[22-24] We repeated the synthesis of $_{OA}$GNP under exactly the same conditions two additional times and the absorbance of the SPR bands of the solution at different reaction stage are included in Figure 3-8. From the three batches of data, it can be seen that the reproducibility of the reaction is very good.

The average of the three sets of data was fit to a logistic model by a nonlinear regression function and the fitting curve is shown in Figure 3-8 (solid line).

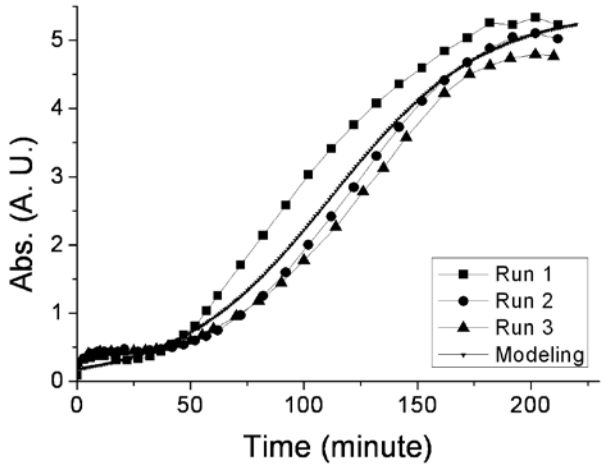

Figure 3- 8. Plots of the SPR band absorbance of reaction solution versus reaction time (min) for three different batches of nanoparticle synthesis and the curve fitting of the experimental data with a logistic model. (Copyright ® 2007 American Scientific Publishers)

The best fit for the combined data sets was found to be the function $f(t)=0.0301696/(0.00554857+e^{-1.80796+0.0301696t})$. This gives a p-value[34] of less than .00001, which is indicative of a very good fit. The good fitting of experimental data with the logistic model suggests that the final size of the nanoparticle product is controlled by an equilibrium state. After the nanoparticle growth reaches a certain size, the combination of the particles into larger ones will form equilibrium with the dissociation of larger particles into smaller ones. This equilibrium state is achieved when the oleylamide ligands form a most stable protecting monolayer around the GNPs through combined hydrogen bonding network formation between the amide groups and the van der Waals interactions between the long hydrocarbon chains of oleylamide ligands.

3.4 Conclusions

From this study, we discovered some interesting details on the structure and growth mechanism of a gold nanoparticle product that was synthesized in solution using an organic amine ligand as both reducing agent and capping agent. This reaction has promising potential for large scale and environmental friendly production of gold nanoparticle materials due to its simplicity and the use of water as reaction solvent. The important findings of this work include: (1) the amine ligands were oxidized into amides when gold (III) was reduced and the amide ligands formed a hydrogen bonding network as a protecting layer around the GNPs; (2) the nanoparticle growth follows a process of thermal decomposition of large amine or amide-Au complex aggregates into smaller particles and the recombination of these smaller particles into more thermally stable larger particles; and (3) the concentration (population) increase of the thermally stable nanoparticles in solution follows a logistic model. Although the detailed reason behind the last finding remains unclear, it is interesting to note that the growth of nanoparticles in solution bears some close resemblance to natural population growth models. A further study along this line may lead to a better understanding and methods for controlled nanoparticle synthesis.

References:

1 Daniel, M.-C.; Astruc. D. Chem. Rev. 2004, 104, 293−346.

2 Burda, C.; Chen, X. R. Narayanan and M. A. El-Sayed. Chem. Rev. 2005, 105, 1025–1102.

3 Katz, E.; Willner, I. Angew. Chem. Int. Ed. 2004, 43, 6042–6108.

4 Pissuwan, D.; Valenzuela, S. M.; Cortie, M.B. Trends Biotech. 2006, 24, 62-67.

5 Kogan, M.J.; Bastus, N.G.; Amigo, R.; Grillo-Bosch, D.; Araya, E. Nano. Lett. 2006, 6, 110-115.

6 Faraday, M. Philos. Trans. R. Soc. London. 1857, 147, 145-153.

7 Schmid, G. Clusters and Colloids: From Theory to Applications 2004, VCH: New York.

8 Templeton, A.C.; Wuelfing, M.P.; Murray, R.W. Acc. Chem. Res. 2000, 33, 27-36.

9 Perez-Juste, J.; Pastoriza-Santos, I.; Liz-Marzan, L.M.; Mulvaney, P. Coordination Chem. Rev. 2005, 249, 1870-1901.

10 Turkevich, J.; Stevenson, P.C.; Hillier, J. Discuss. Faraday Soc. 1951, 11, 55-75.

11 Brust, M.; Walker, M.; Bethell, D.; Schiffrin, D.J.; Whyman, R. J. Chem. Soc., Chem. Commun. 1994, 801-802.

12 Hostetler, M.J.; Wingate, J.E.; Zhong, C.-J.; Harris, J.E.; Vachet, R.W.; Clark, M.R.; Londono, J.D.; Green, S.J.; Stokes, J.J.; Wignall, G.D.; Glish, G.L.; Porter, M.D.; Evans, N.D.; Murray, R. W. Langmuir. 1998, 14, 17-30.

13 Leff, D.V.; Brandt, L.; Heath, J.R. Langmuir. 1996, 12, 4723-4730.

14 Selvakannan, P.R.; Kuman, P.S.; More, A.S.; Shingte, R.D.; Wadgaonkar, P.P.; Sastry, M. Langmuir 2004, 20, 295-298.

15 Knecht, M.R.; Garcia-Martinez, J.C.; Crooks, R.M. Langmuir. 2005, 21, 11981-11986.

16 Zheng, N.; Fan, J.; Stucky, G.D. J. Am. Chem. Soc. 2006, 128, 6550-6551.

17 Gomez, S.; Philippot, K.; Colli`ere, V.; Chaudret, B.; Senocq, F.; Lecante, P. Chem. Comm. 2000, 1945–1946.

18 Hiramatsu, H.; Osterloh, F.E. Chem. Mater. 2004, 16, 2509-2511.

19 Aslam, M.; Fu, L.; Su, M.; Vijayamohanan, K.; Dravid, V. P. J. Mater. Chem. 2004, 14, 1795-1797.

20 Liu, X.; Worden, J.G.; Huo, Q.; Brennan, J.P. J. Nanosci. Nanotech. 2006, 6, 1054-1059.

21 Verhulst, P.F. Correspondance Mathématique et Physique. 1838, 10, 113-121.

22 Ausloos, M.; Dirickx, M. The logistic map and the route to chaos: from the beginnings to modern applications; Springer-Verlag: Berlin, 2006.

23 Gottman, J.M.; Murray, J.D.; Swanson, C.C.; Tyson, R.; Swanson, K.R. The mathematics of marriage; MIT Press: Cambridge, MA, 2002.

24 Thieme, H.R. Mathematics in population biology; Princeton University Press: Princeton, NJ, 2003.

25 MATHMATICA, Wolfram Research Inc., Champaign, IL, Version 2.5 2005.

26 Socrates, G. Infrared and Raman, Characteristic Group Frequencies: Tables and Charts, 3rd ed.; John Wiley & Sons LTD: England, 2001.

27 Sun, X.; Dong, S.; Wang, E. Mater. Chem. Phys. 2066, 96, 29-33.

28 Pavia, D.L.; Lampman, G.M.; Kriz, G.S. Introduction to Spectroscopy, 3rd ed.; Thomson Learning Inc., 2001.

29 Shaffer, A.; Worden, J.G.; Huo, Q. Langmuir. 2004, 20, 8343-8351.

30 Badia, M.; Demers, L.; Dickinson, L.; Morin, F.G.; Lennox, R.B.; Reven, L. J. Am. Chem. Soc. 1997, 119, 11104-11105.

31 Hasan, M.; Bethell, D.; Brust, M. J. Am. Chem. Soc. 2002, 124, 1132-1133.

32 Kohlmann, O.; Steinmetz, W.E.; Mao, X.-A.; Wuelfing, P.; Templeton, A.C.; Murray, R.W.; Johnson Jr., C.S. J. Phys. Chem. B. 2001, 105, 8801-8809.

33 Kumar, A.; Mandal, S.; Selvakannan, P.R.; Pasricha, R.; Mandale, A.B.; Sastry, M. Langmuir 2003, 19, 6277-6282.

34 Obtained from the online facility for the computation of p-values for the F-statistic at http://davidmlane.com/hyperstat/F_table.html

CHAPTER 4. MONOFUNCTIONAL GOLD NANOPARTICLES PREPARED FROM A NONCOVALENT INTERACTION-BASED SOLID PHASE MODIFICATION APPROACH

4.1 Introduction

The ability to prepare gold and other metal nanoparticles with a controlled surface chemistry is critically important for the preparation of more complex nanostructures. Since the initial results by Brust and Schiffrin, numerous methods have been published for the preparation of monolayer protected GNPs of different sizes with a variety of surface functional groups.[1-3] Until recently, the ability to control the surface functionality has been limited to the place exchange reaction between existing bound ligands on the nanoparticle surface and bifunctional ligands in solution.[3,4] It has recently been demonstrated by several authors that polymeric solid supports such as Wang resin may be used for the controlled surface functionalization of GNPs.[4-8] Previous techniques relied on the covalent bonding of a bifunctional ligand onto the solid support and subsequent place exchange with GNPs in solution. Under the proper conditions, nanoparticles with a single or very small number of functional groups can be cleaved from the solid support as the major product.

In this communication we present an alternative method for the solid-phase preparation of monofunctionalized GNPs using noncovalent interactions. The purpose of this work was to reduce the cost and time for the synthesis and to find milder reaction conditions so that a wider range of nanoparticles could be modified by this method.

4.2 Experimental

4.2.1 Preparation of monofunctional $_{Bt}GNP_{COOH}$ particles using amine-functional silica Gel

Electrostatic absorption of 11-mercaptoundecanoic acid onto amino functionalized silica gel was performed by suspending 3 g of silica gel in 10 mL of 1:1 dichloromethane with methanol followed by addition of the appropriate amount of 11-mercaptoundecanoic acid as indicated in Table 4-1. The reaction mixtures were then shaken vigorously for 30 minutes at room temperature. The silica gel was then filtered and thoroughly washed with dichloromethane and methanol to remove any unbound free thiol ligands. Ellman's agent (5,5'-dithio-bisnitrobenzoic acid) was used to monitor the absorption of thiol ligands to dried silica gel. The dried silica gel with bound 11-mercaptoundecanoic acid was suspended in 2 mL of dichloromethane. To the suspension, 30 mg of 2.2 nm $_{Bt}$GNP in 6 mL of dichloromethane was added. The exchange reaction was allowed to proceed for 8-12 hours at room temperature with gentle shaking. During this time the silica gel turned dark black. After filtering and washing with warm dichloromethane to remove unbound nanoparticles, the silica gel was dried under vacuum. The nanoparticles were then cleaved from the gel by suspending the gel in 4.0 mL of 5% acetic acid in dichloromethane and shaking the suspension for 5 minutes at room temperature. Functionalized GNPs were collected by filtration and dried by gentle nitrogen flow.

The crude product was purified by washing the sample several times with petroleum ether with occasional sonication followed by centrifugation. After each cycle, the wash solution was tested for organic impurities by spotting a TLC plate and checked

for impurities with a UV lamp. After drying, the nanoparticles were further purified by GPC using Sephadex LH-20 gel. Using dichloromethane as the solvent, Sample A (which had the highest concentration of 11-mercaptoundecanoic acid) split into two bands. The first band (about half of the sample) consisted of nanoparticles which could be collected in pure dichloromethane. About half of the second band could be collected when the solvent mixture was changed to 9:1 dichloromethane with acetic acid. The remaining sample could not be collected unless pure acetic acid was added to the column. For sample B, most of the sample was soluble in pure dichloromethane while a small portion was collected when a 9:1 solution of dichloromthane with acetic acid was added to the column. Sample C was found to be soluble in pure dichloromethane and was collected in one portion. The total yield of the $_{Bt}GNP_{COOH}$ nanoparticles obtained for sample C was about 50% (calculated from the amount of nanoparticles added to the solid phase place exchange reaction. For 3g of silica gel, 15mg of monofunctional GNPs were obtained from 30 mg of nanoparticles added in the solid phase place exchange reaction).

4.2.2 Preparation of monofunctional $_{Bt}GNP_{COOH}$ nanoparticles using Rink resin

Solid phase synthesis using Rink resin was performed using the same procedure as for the silica gel except for the following changes. First, the resin was initially suspended for 30 minutes in a. 20% solution of piperidine in DMF to remove the fluorenylmethyloxycarbonyl (FMOC) protecting groups. Second, a 50:1 molar ratio between the amino groups on the resin and the 11-mercaptoundecanoic acid was used to load the resin. Third, the nanoparticles were cleaved from the resin using a 20% acetic acid in dichloromethane for 5 minutes with stirring. It was estimated that about half the nanoparticles could be cleaved off the resin.

The crude product was further purified by the following procedure. The dark residue was washed with petroleum ether 10-15 times with occasional sonication followed by centrifugation. After each cycle, the washing solution was tested for organic impurities by spotting a TLC plate and checked for impurities with a UV lamp. To the sample, a solvent mixture of 9:1 dichloromethane:methanol was added and the sample was briefly sonicated. It was found that approximately half the sample was soluble in this solvent mixture. The remaining portion only became soluble when a trace amount of acetic acid was added to the sample. The sample in the 9:1 dichloromethane:methanol solution was further purified by passing the sample through a small column of reverse phase C18-modified silica gel in the same solvent mixture. It was found that more than 90% of the samples could be recollected.

4.3 Results and Discussions

The synthetic strategy used in this investigation is shown in Figure 4-1. The solid support used in this study was amino group functionalized silica gel. The bifunctional ligands, 11-mercaptoundecanoic acid, were then loaded onto the support directly through electrostatic interaction between the positively charged amino groups from silica gel and negatively charged carboxylic acid groups from the 11-mercaptoundecanoic acid ligands. The solid-phase modification was performed using three different ratios of 11-mercaptoundecanoic acid relative to that of the total number of amino groups on the silica gel as shown in Table 4-1. The amine to thiol ratio was calculated according to the weight percentage of nitrogen (2.1%) of the modified silica gel provided by the supplier. It is to be noted that the amino group to thiol ligand ratio is very high to ensure that only

one thiol ligand will be attached to one gold nanoparticle during the place exchange reaction.

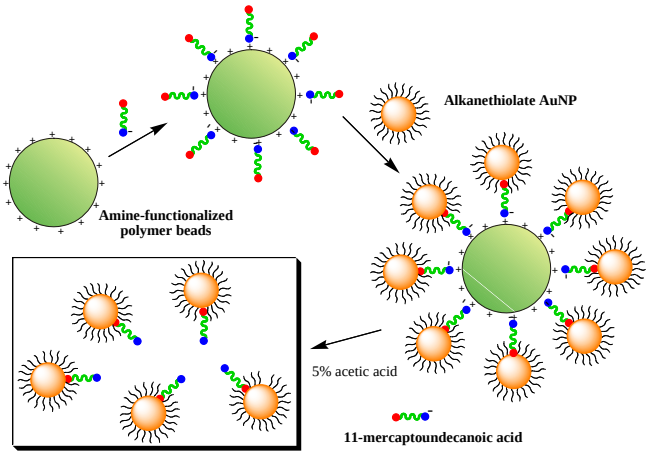

Figure 4- 1. Solid-phase method for the preparation of monofunctional GNPs using noncovalent interactions. (Copyright ® 2006 Wiley-VCH-Verlag Gmbh & Co. KgaA, Weinheim)

Table 4- 1. Experimental conditions used for the solid phase modification of GNPs

Sampl	Concentration of 11-mercaptoundecanoic acid (mol	Amine to thiol
A	**7.5×10^{-5}**	**6,000:1**
B	**2.5×10^{-5}**	**18,000:1**
C	**8.3×10^{-6}**	**54,000:1**

After loading the thiol ligands onto the silica gel and washing away any unbound thiol molecules, the surface-bound thiol groups were then allowed to undergo the place exchange reaction with $_{Bt}$GNPs which were prepared using the Schiffrin reaction with an average diameter of 2.2 nm. It was observed that after 8-12 hours of shaking at room temperature, the silica gel clearly began to acquire a brown color. Sample A exhibited the darkest color, while sample C was the lightest. After washing off any unbound nanoparticles, the silica gel-bound nanoparticles were cleaved using a solution of 5% acetic acid in dichloromethane for 5 minutes. The crude product was purified by washing with petroleum ether followed by GPC to yield monocarboxyl GNPs with a yield of 60-

90% (Calculated from the amount of nanoparticles loaded into the GPC column). Since the nanoparticles were not covalently bound to the silica gel, the cleavage step could be completed using very mild conditions in a much shorter period of time compared to previous work using covalent bond-based solid-phase synthesis.

During the purification process it was observed that there were solubility differences between the products obtained from the three different experimental conditions. When sample A was purified by GPC, it was observed that about 50% of the sample could be recollected using dichloromethane as the mobile phase. A second band consisting of about 25% of the particles could then be collected when the solvent was switched to 9:1 dichloromethane with acetic acid. The remaining sample could not be collected unless pure acetic acid was added to the column. For sample B it was found that most of the sample was soluble in dichloromethane, but a small portion remained insoluble unless the 9:1 dichloromethane with acetic acid solution was used. For the case of sample C, it was observed that acetic acid was not needed for solubility. The solubility results indicate a clear difference between the products from the three experimental conditions. The increased solubility of the nanoparticle product in pure dichloromethane from sample C indicates that these nanoparticles have less carboxylic acid groups compared to the nanoparticles collected in sample B and especially compared to sample A. The higher number of carboxylic acid groups from samples A and B is a clear sign of multiple place exchange reactions between the $_{Bt}$GNP nanoparticles and the bound 11-mercaptoundecanoic acid ligands on the silica gel surface.

To further evaluate the success of this noncovalent interaction-based solid-phase synthesis, the nanoparticles were reacted with ethylenediamine (EDA). If the

nanoparticles contain a single carboxylic acid group, then one would expect a very low percentage of nanoparticle trimers and larger aggregates.[6] Figure 4-2 shows the TEM images of the monofunctional GNPs after reacting with EDA for samples A and C. The results indicate that a majority of the nanoparticles from Sample A appeared as trimers or larger aggregates. In contrast, the TEM image for sample C indicates that less than 5-10% of the nanoparticles appeared as trimers or larger aggregates, suggesting that these nanoparticles have very few surface functional groups. In both TEM images, there are also a substantial amount of single particles. These particles are believed to be particles that have reacted with EDA (because large excess of EDA was added to drive the reaction to completion), but not with other particles.

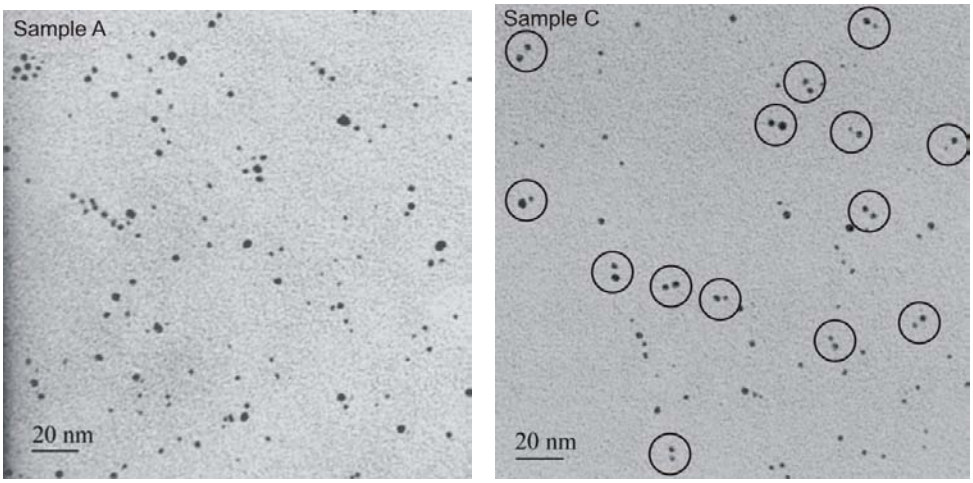

Figure 4- 2. TEM images of EDA coupled $_{Bt}GNP_{COOH\ COOH}$ nanoparticles that were prepared using amino group functionalized silica gel. (Copyright ® 2006 Wiley-VCH-Verlag Gmbh & Co. KgaA, Weinheim)

In addition to amino group functionalized silica gel, Rink resin was also used for the surface functionalization of GNPs. Rink resin is an amino group functionalized resin consisting of a lightly crosslinked polystyrene matrix. To use the Rink resin, the amino groups were first deprotected using a 20% solution of piperidine in DMF. The Rink resin

was then used as a polymer support for the attachment of 11-mercaptoundecanoic acid ligands and subsequent preparation of monofunctional nanoparticles. Following the same synthesis and purification protocol as used in the case of silica gel support, the collected nanoparticle product was found to be soluble in a solution of 9:1 dichloromethane with methanol.

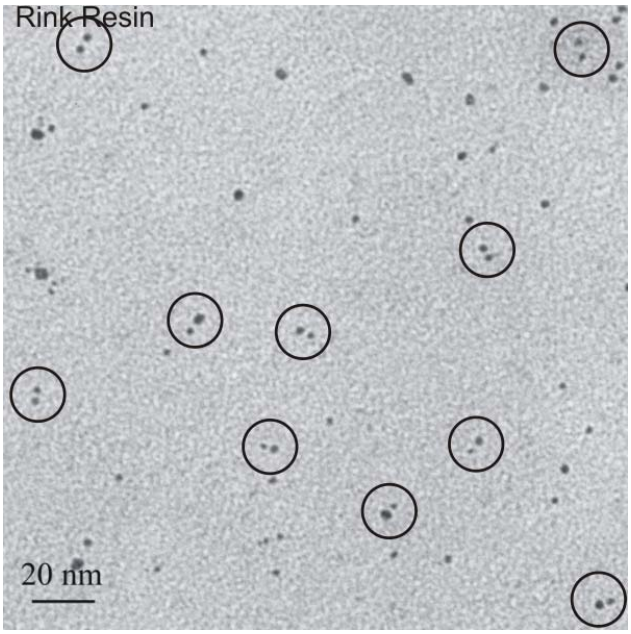

Figure 4- 3. TEM image of EDA coupled $_{Bt}GNP_{COOH\ COOH}$ nanoparticles that were prepared using Rink resin. (Copyright ® 2006 Wiley-VCH-Verlag Gmbh & Co. KgaA, Weinheim)

Table 4- 2. XPS results of monofunctional GNPs prepared using Rink resin as the solid support.

element	binding energy (eV)	normalized area	total area	assignment
O	**531.7**	**33.77**	**717.21**	**COOH**[9]
	532.7	**211.31**		**H_2O**[10]
	533.8	**232.05**		**SiO_2**[11]
S	**162.3**	**499.96**	**518.59**	**S-Au**[12]
	163.9	**18.64**		**S-H**[12]

Figure 4-3 is the TEM image of these nanoparticles after coupling with EDA. As can be seen there are a large number of nanoparticle pairs and single particles with only a

few trimers. In addition to TEM analysis, these nanoparticles were also characterized by X-Ray Photoelectron Spectroscopy (XPS) and the results are shown in Table 4-2 and Figure 4-4. By comparing the normalized area of oxygen from the carboxylic acid functional ligand to that of sulfur from all the thiolate ligands, it is possible to determine how many carboxylic acid group ligands are on the nanoparticle surface. The results indicate that approximately 3% of the ligands on the nanoparticle surface are 11-mercaptoundecanoic acid (Table 4-2). This exchange level is consistent with what was observed in our previously reported NMR study for monofunctional GNPs prepared using Wang resin as the solid support, indicating that only a minimum number of bifunctional thiol ligands were attached to nanoparticle surface.[4] It should be noted here that so far there is no analytical technique available to provide exclusive evidence on the monofunctional group identity of these solid phase-modified GNPs. The key barrier is that one can not obtain nanoparticles with absolute monodispersity at the nanometer scale range using the existing chemical synthesis methods. Without a monodispersed size and molecular weight of the nanoparticles, an accurate quantitative analysis of the number of functional groups attached to the particle surface cannot be conducted. So far we found that the most reliable method to determine the relative purity of monofunctional nanoparticle product is by conducting a diamine coupling reaction to the solid phase modified nanoparticles and using TEM to analyze the coupled product. The fewer amounts of nanoparticle trimers, tetramers and other oligomers appeared in the TEM images correspond to a higher purity of monofunctional nanoparticles in the product, as explained in much detail in our previous work.[6]

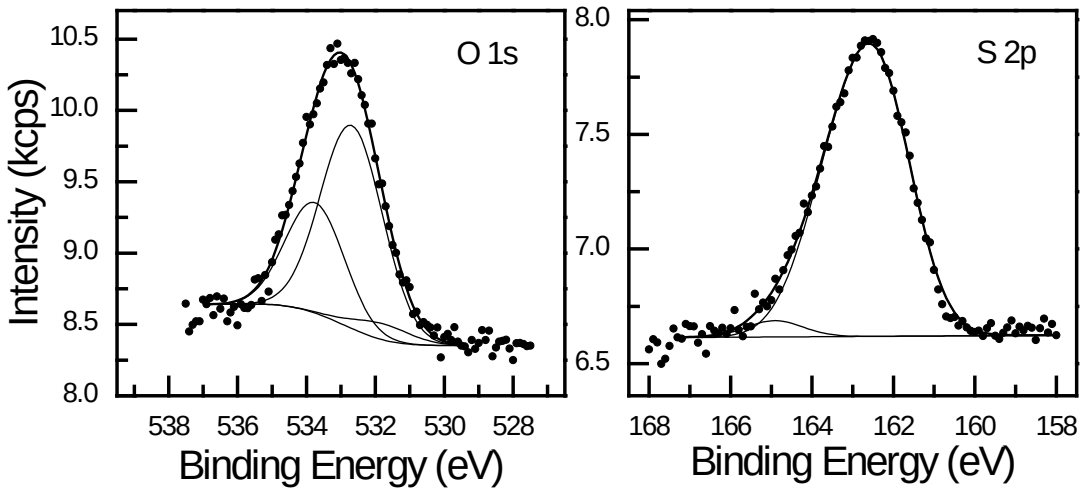

Figure 4- 4. O 1s and S 2p regions from the XPS spectrum of monofunctional GNPs prepared from Rink resin. (Copyright ® 2006 Wiley-VCH-Verlag Gmbh & Co. KgaA, Weinheim)

4.4 Conclusion

Through this study, we demonstrated that bifunctional thiol ligands can be effectively loaded to polymer support by noncovalent interactions. After place exchange reaction, GNPs with a single functional group on the surface were obtained as the major product by cleaving from polymer support under very mild conditions. This mild condition will allow the use of this solid phase method for controlled chemical functionalization of a wider range of nanoparticles. The purification process was also simplified significantly. Compared to the previously reported solid-phase modification based on covalent bond chemistry, the current modification can be completed in a much shorter period of time and is much more cost effective. The scale-up preparation of monofunctional nanoparticles with reasonable quantities is becoming possible.

References:

1 Brust, M.; Walker, M.; Bethell, D.; Schiffrin, D.J.; Whyman, R.J. J. Chem. Soc. Chem. Commun. 1994, 801-802.

2 Templeton, A.C.; Wuelfing, W.P.; Murray, R.W. Acc. Chem. Res. 2000, 33, 27-36.

3 Hostetler, M.J.; Templeton, A.C.; Murray, R.W. Langmuir 1999, 15, 3782 -3789.

4 Shaffer, A.W.; Worden, J.G.; Huo, Q. Langmuir 2004, 20, 8343-8351.

5 Worden, J.G.; Shaffer, A.W.; Huo, Q. Chem. Commun. 2004, 518-519.

6 Worden, J.G.; Dai, Q.; Shaffer, A.W.; Huo, Q. Chem. Mater. 2004, 16, 3746-3755.

7 Sung, K.-M.; Mosley, D.W.; Peelle, B.R.; Zhang, S.; Jacobson, J.M. J. Am. Chem. Soc. 2004, 126, 5064-5065.

8 Abed, A. Vaskevich, R. Arad-Yellin, A. Shanzer, I. Rubinstein, Chem. Eur. J. 2005, 11, 2836-2841.

9 Schnadt, J.; O'Shea, J.N.; Patthey, L.; Schiessling, J.; Krempaský, J.; Shi, M.; Martensson, N.; Brühwiler, P.A. Surf. Sci. 2003, 544, 74-86.

10 Wagner, C.D.; Zatko, D.A.; Raymond, R.H. Anal. Chem. 1980, 52, 1445-1451.

11 Montero, M.; Galán, L.; de la Cal, E.; Albella, J.M.; Pivin, J.C. Thin Solid Films 1990, 193, 325-332.

12 Joseph, Y.; Besnard, I.; Rosenberger, M.; Guse, B.; Nothofer, H-G.; Wessels, J.M.; Wild, U.; Knop-Gericke, A.; Su, D.; Schlögl, R.; Yasuda, A.; Vossmeyer, T. J. Phys. Chem. B 2003, 107, 7406-7413.

CHAPTER 5. EXTINCTION AND SCATTERING PROPERTIES OF GOLD NANOPARTICLES AT THEIR SURFACE PLASMA RESONANCE BAND

5.1 Introduction

GNPs are among one of the most extensively studied nanomaterials. Since the first report of gold colloids more than 100 years ago by Faraday,[1,2] numerous studies have been reported on the synthesis, property study and application development of gold clusters, colloids, and nanoparticles.[3-6] GNPs exhibit many unique and interesting physical and optical properties such as surface plasmon resonance (SPR), surface enhanced Raman scattering (SERS), nonlinear optical properties (NLO), and quantized charging effect.[7-9] The surface plasmon resonance of GNPs is an optical property that holds promising potentials in biosensing, molecular imaging, and photothermal treatment of diseases. Mirkin et al. demonstrated the use of GNPs as an optical probe to detect DNA molecules based on the color change of individually scattered nanoparticles and the complementary DNA-hybridized nanoparticle aggregates.[10] Recently the photothermal conversion property of GNPs and nanoshells has attracted a keen interest from the scientific community.[11] GNPs or nanoshells that are irradiated by a laser beam at a wavelength around the SPR band can efficiently convert the photon energy to thermal energy, which leads to the destruction of biological cells such as tumor and bacteria.[12,13] The analysis of SPR band can also provide valuable information on the size, structure and aggregation properties of GNPs. We herein present in our study of using UV-Vis absorption spectroscopy and transmission electron microscopy to determine the extinction coefficients of GNPs with different sizes and different capping ligand monolayer. The extinction coefficient is an important parameter that can be used to

calculate the nanoparticle concentration or estimate the nanoparticle size. Although this may appear to be a trivial issue, the accurate calculation or estimation of the molar concentration of nanoparticles is actually a challenge. The main reason is that nanoparticles are not monodispersed. For some particles synthesized from one batch to another, the size and size dispersity may vary significantly. Recently, El-Sayed et al. reported a theoretical calculation of extinction coefficient of GNPs and its dependence on the nanoparticle size.[14] Experimental studies reported by the same group earlier on a citrate-stabilized GNPs were in accordance with these theoretical calculations.[15] In our study, we examined three different types of GNPs, citrate-stabilized GNPs with size ranging from approximately 5 to 250 nm; oleylamide-protected GNPs with an average diameter around 8 nm; and a decanethiol-stabilized gold nanoparticle with an average core diameter of 4 nm. Our analysis revealed that despite the different capping ligands and the solvents used to dissolve GNPs, the logarithms of extinction coefficient and nanoparticle core diameter follow a linear relationship. This correlation can be used as an effective rule-of-thumb to estimate nanoparticle concentration or core size.

5.2 Experimental

5.2.1 Chemicals and materials

Citrate stabilized GNPs ($_{Ci}$GNPs) (with sizes at ~5 nm, ~10 nm, 20 nm, 40 nm, 60 nm, 80 nm, 100 nm, 150 nm, 200 nm and 250 nm) were purchased from Aldrich. Oleylamine ($C_{19}H_{37}NH_2$; tech., 70%), decanethiol, tetraoctylammonium bromide, sodium borohydride, trisodium citrate and all solvents (ACS Reagents) were purchased from Aldrich (Milwaukee, WI). Hydrogen tetrachloroaurate (III) hydrate ($HAuCl_4 \cdot xH_2O$) was purchased from Strem Chemicals (Newburyport, MA).

5.2.2 Synthesis of $_{Dt}$GNPs, $_{OA}$GNPs and $_{Ci}$GNPs

1-Decanethiol protected GNPs ($_{Dt}$GNPs) were synthesized according to a modified Brust-Schiffrin reaction.[16] Briefly, $HAuCl_4 \cdot xH_2O$ (310 mg, 1 equiv) was dissolved in 25 mL nanopure water and phase transferred to 80 mL toluene using 1.5 g of tetraoctylammonium bromide. Following the addition of 1-decanethiol (17 μL, 1/11 equiv) and aqueous solution of $NaBH_4$ (0.38 g, 10 equiv, in 25 mL nanopure water) into the organic phase, the reaction solution was stirred at room temperature for 3h. Oleylamide-protected GNPs ($_{OA}$GNPs) were synthesized by following a reported method .[17] Typically, 35 mg of $HAuCl_4 \cdot xH_2O$ was dissolved in 80 mL nanopure water and heated up to 80 ^oC before addition of 200 μL oleylamine by a syringe. The reaction was allowed to continue for 3h. After the reaction mixture was cooled down to room temperature, 240 mL methanol was added to the solution and nanoparticles were collected by precipitation and washing a few times with a copious amount of methanol. The 25.67 nm and 34.36 nm $_{Ci}$GNPs were synthesized according to Turkevich method.[18]

5.2.3 High Resolution Transmission Electron Microscopy (HRTEM)

TEM grids were treated with polylysine solution first before depositing nanosphere water solutions onto grids. The HRTEM images of each sample were obtained using a FEI TECNAI F30 transmission electron microscope. The accelerating voltage used in the measurement was 300 keV. The 400 mesh carbon/formvar-coated copper grids for citrate-stabilized nanoparticles were first treated with a poly-L-lysine (M.W. 93800, Sigma) solution (0.0381 g/mL in 1:3 H_2O: MeOH mixture solvents). TEM sample grids were then prepared by extracting 5 μL sample solution, casting onto polylysine treated grids and vacuum dried. Average gold core diameter (*D*), size

distributions and standard deviations were calculated for each nanoparticle sample by averaging 200 particles from the TEM images using ImageJ software (developed at the National Institutes of Health).

5.2.4 UV-Vis spectroscopy

All UV-Vis spectra were recorded using a Cary 300 Bio double-beam UV-Vis spectrophotometer at a 300 nm/min scanning rate from 300-700 nm. For each sample, UV-vis spectra at five different concentrations were recorded by directly diluting the as-prepared nanoparticle solution with appropriate solvents to the expected relative concentrations. For $_{Ci}$GNPs samples (diameters at 4.61, 8.55, 20.6, 25.67, 34.46 nm), solutions with relative concentrations of 1.0, 0.8, 0.6, 0.4, and 0.2 to the initial concentrations were prepared using Nanopure water as solvent. For $_{Ci}$GNPs at other sizes, the original solutions were measured. For $_{Dt}$GNPs, relative concentrations of 0.088, 0.070, 0.053, 0.035 and 0.018 to the initial concentration of the as-prepared sample were obtained by diluting the sample with toluene. For $_{OA}$GNPs sample, THF was used as the solvent to dilute the as-prepared sample to achieve relative concentrations of 0.064, 0.124, 0.244, 0.515 and 1.040 to the initial concentration. The extinction coefficient at the corresponding SPR peak wavelength was calculated according to the Beer's Law.

5.2.5 Size and scattering intensity measurements of $_{Ci}$GNPs solutions by Dynamic Light Scattering

Solutions of $_{Ci}$GNPs at sizes 40, 60, 80, 100, 150, 200, and 250 nm were measured by a Malvern ZetaSizer NanoZS DLS system. All DLS measurements were done under the same parameter setup: sample volume 40 µL, measurement angle 13^{o}, fixed sample position 4.65 µm, and fixed attenuation 11. The intact $_{Ci}$GNPs solutions

were diluted to different concentrations. The concentrations of GNPs were calculated according to the product description from the vendor and also the dilution factors used in this study. For each sample measured by DLS, the size and the DLS scattering intensity were recorded. Detection limits of GNPs by DLS were calculated using the standard 3σ method.

5.3 Results and Discussions

5.3.1 Calculation of average number of gold atoms per GNP

The average number of gold atoms per nanoparticle may be calculated from TEM analysis. The HRTEM images of four nanoparticle product synthesized in this study are shown in Figure 5-1. Using ImageJ software, the average core diameters of the particles (*D*/nm) were measured and summarized in Table 5-1. Assuming a spherical shape and a uniform fcc structure,[19] the average number of gold atoms (*N*) for each type of nanosphere was calculated by equation (5-1), where ρ is the density for fcc gold (19.3 g/cm^3) and *M* stands for atomic weight of gold (197 g/mol).[20,21]

$$N = \frac{\pi}{6}\frac{\rho D^3}{M}N_A = 30.89602 \times D^3 \quad (5\text{-}1)$$

$$C = \frac{N_{Total}}{N \times V \times N_A} \quad (5\text{-}2)$$

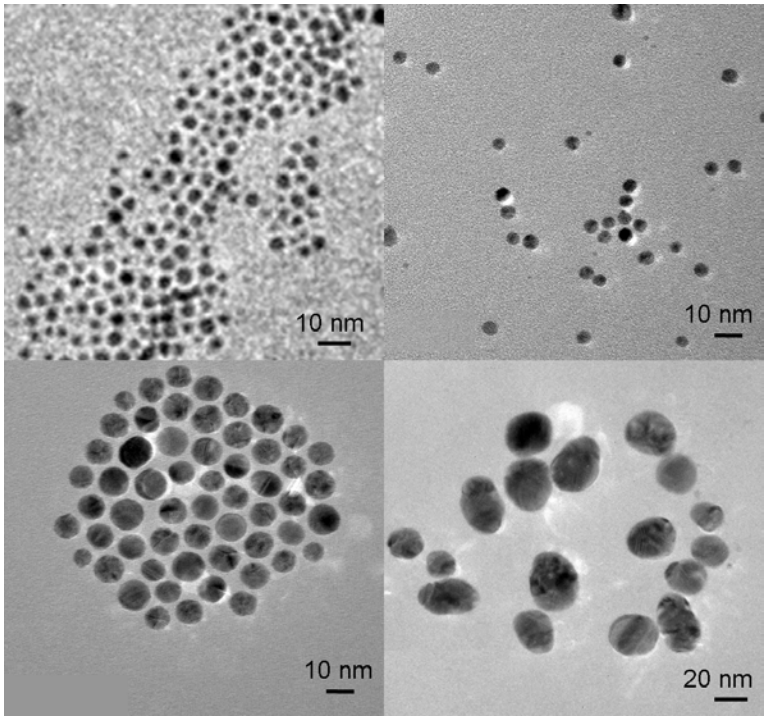

Figure 5- 1. High resolution transmission electron microscopy images of (a) 3.76 nm 1-decanethiol-capped AuNPs; (b) 4.61 nm citrate-stabilized AuNPs; (c) 7.58 nm oleylamide-protected AuNPs and (d) 25.67 nm citrate-stabilized AuNPs. (Copyright ® 2007 Elsevier B.V.)

5.3.2 Determination of molar concentrations of nanoparticle solution

The molar concentration of the nanosphere solutions were calculated by dividing the total number of gold atoms (N_{total}, equivalent to the initial amount of gold salt added to the reaction solution) over the average number of gold atoms per nanosphere (N) according to equation (5-2), where V is the volume of the reaction solution in liter and N_A is the Avogadro's constant. It is assumed that the reduction from gold (III) to gold (0) was 100% complete. The concentrations of each diluted solution may be calculated from this initial concentration according to their relative concentration as stated in the experimental section. Concentrations of all sizes GNPs were calculated by either this method or as provided by the product vendor (Table 5-1).

Table 5- 1. The extinction coefficients (ε) of gold nanoparticles with different core sizes and capping ligands determined in this study

Surface ligand	Solvent	GNP Diameter D (nm) [a]	SPR band Peak λ_{max} (nm)	Original concentration (M)	Extinction Coefficient ε ($M^{-1}cm^{-1}$)
Decanethiol	Toluene	3.76±0.65	506	9.45E-06 [b]	(3.61±0.08) E+6
Citrate	Water	4.61±0.48	517	9.42E-08 [b]	(8.56±0.09) E+6
Citrate	Water	8.55±0.79	517	1.49E-88 [b]	(5.14±0.07) E+7
Oleylamine	THF	8.76±1.11	520	1.30E-07 [b]	(8.79±0.03E+7
Citrate	Water	20	521	1.16E-09 [c]	7.62E+08
Citrate	Water	20.60±1.62	521	1.07E-09 [b]	(8.78±0.06) E+8
Citrate	Water	25.67±5.62	526	4.92E-10 [b]	(2.93±0.02E+9
Citrate	Water	34.46±4.34	529	2.22E-10 [b]	(6.06±0.03) E+9
Citrate	Water	40	530	1.49E-10 [c]	7.07E+09
Citrate	Water	60	531	4.32E-11 [c]	2.92E+10
Citrate	Water	80	545	1.83E-11 [c]	5.58E+10
Citrate	Water	100	564	9.30E-12 [c]	9.14E+10
Citrate	Water	150	642	2.82E-12 [c]	1.47E+11
Citrate	Water	200	571	1.16E-12 [c]	3.15E+11
Citrate	Water	250	600	5.98E-13 [c]	4.78E+11

[a] Values with standard deviations were the average size of 200 GNPs from TEM images, respectively for each size GNPs. Values without standard deviations were cited from the product description provided by the vendor.
[b] Values obtained according to Equations (5-1) and (5-2).
[c] Values obtained according to the product description provided by the vendor.

5.3.3 Extinction coefficients

5.3.3.1 Calculations of extinction coefficients

The extinction coefficient of each nanoparticle sample was determined according to Lambert-Beer Law, equation (5-3). The as-prepared or purchased GNP solution was diluted into solutions into different concentrations as stated in the experimental section. The absorption spectrum of each solution was measured. The absorbance at 506 nm was recorded for each sample and plotted versus the molar concentration of the solution. The extinction coefficient can be obtained from the slope of the linear region of the absorbance-concentration curve. Other samples were analyzed in the similar way.

$$A = \varepsilon b C \qquad (5\text{-}3)$$

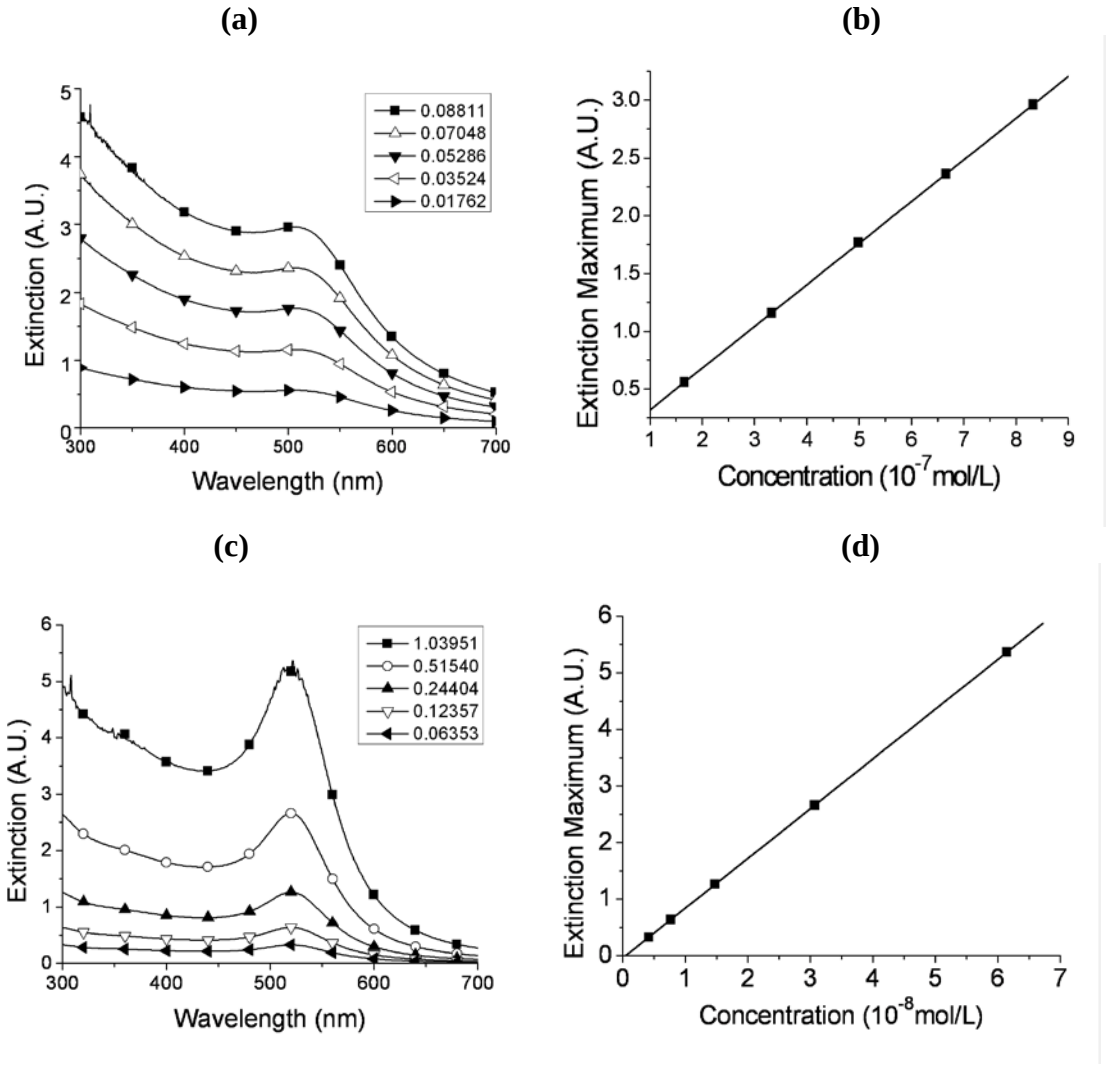

Figure 5- 2. Extinction spectra of (a)1-decanethiol and (c) oleylamide-protected gold nanoparticles at different relative concentrations. (b) and (d) are plots of experimental data of maximum extinction around 520 nm versus corresponding concentration and the linear fitting curves for decanethiol and oleylamide-protected gold nanoparticles, respectively. (Copyright ® 2007 Elsevier B.V.)

Figure 5-2a-d is an illustration of the UV-Vis absorption spectra and the linear fitting curve of absorbance-concentration plots for decanethiol and oleylamide-protected GNPs. Both curves are linear with a correlation coefficient very close to 1.0. A good linear fitting of the experimental data was found for all other nanoparticle samples. The

types of nanoparticles analyzed and the extinction coefficients calculated from the linear fitting curve were summarized in Table 5-1.

5.3.3.2 Shift of the SPR extinction peak

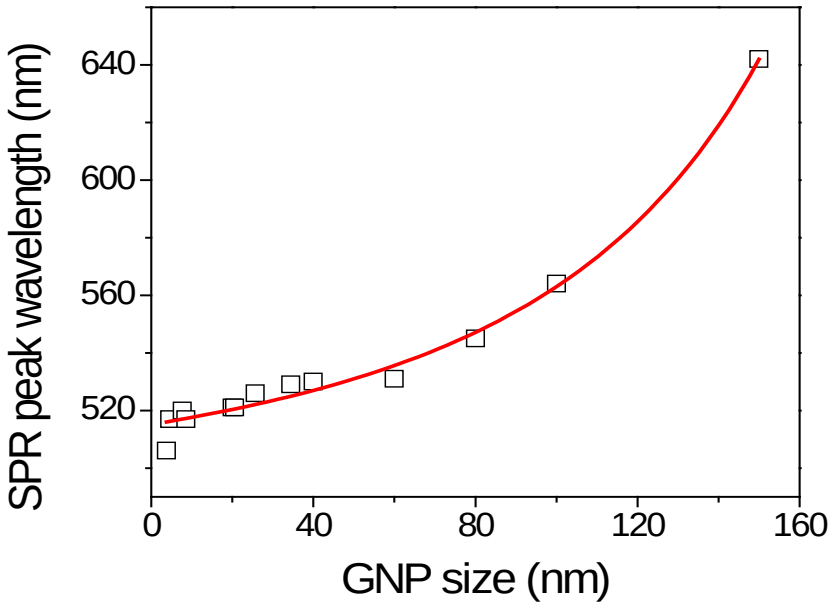

Figure 5- 3. Changes the SPR peak wavelengths of GNPs at increased GNP sizes (3.76 nm to 150 nm) (Lorentz fitting: $Y=485.01704+(2*148589.239/\pi)*(85.20574/(4*(X-255.01039)^2+85.20574^2))$; $R^2=0.98777$)

The SPR band peak wavelength (λ_{max})of GNPs showed a red-shift from 506 nm for the 3.76 GNPs to 642 nm for the 150 nm GNPs. This red-shift trend is in accordence with theoretical calculations made by Yuegubide et al.[24] They calculated that λ_{max} will increased from 535 nm for 20 nm GNPs to the maxima of 665 nm for 160 nm (Table 1-1). Our results illustrated the red-shift tread but showed lower λ_{max} values than predicted, probably due to effects from surface ligands of GNPs and the solvent. For the size range between 3.76 nm to 150 nm, the change of the λ_{max} over the GNP size can be fitted very well with Lorentz fitting, as shown in Figure 5-3. For GNPs with sizes larger than 150 nm, λ_{max} showed a blue-shift, which agrees with the trend predicted in theory.

5.3.3.3 Intensity of extinction coefficients

From Table 5-1, one can notice immediately that the extinction coefficients of GNPs are orders of magnitude higher than organic dye molecules. The measured extinction coefficients of citrate-stabilized GNPs are approximately in line with what has been reported by El-Sayed et al.[14] For example, the extinction coefficient values for a 20 nm citrate-stabilized gold nanoparticle obtained from this study, the experimental and theoretical study by El-Sayed et al are 8.8E8, 1.36E9, and 7.6E7 $M^{-1}cm^{-1}$, respectively. Between the three values, there is approximately an order of magnitude difference. Our data is between the experimental and theoretical value as reported by El-Sayed et al.

From Table 5-1, another important result to notice is that the increase in core diameter of GNPs introduced dramatic and continuous increase in the extinction coefficients. From a core diameter of ~4 nm to 35 nm, the extinction coefficient increased three orders of magnitude. From the double logarithm plot of extinction coefficient against the nanoparticle size in diameter, a good linear relationship was found and can be expressed in equation (5-4), Where ε is extinction coefficient in $M^{-1}cm^{-1}$, D is the core diameter of the nanoparticles, and k=2.85232, a=11.86382. The linear fitting of the experimental data gives a correlation coefficient of 0.99324.

$$\ln \varepsilon = k \ln D + a \qquad (5\text{-}4)$$

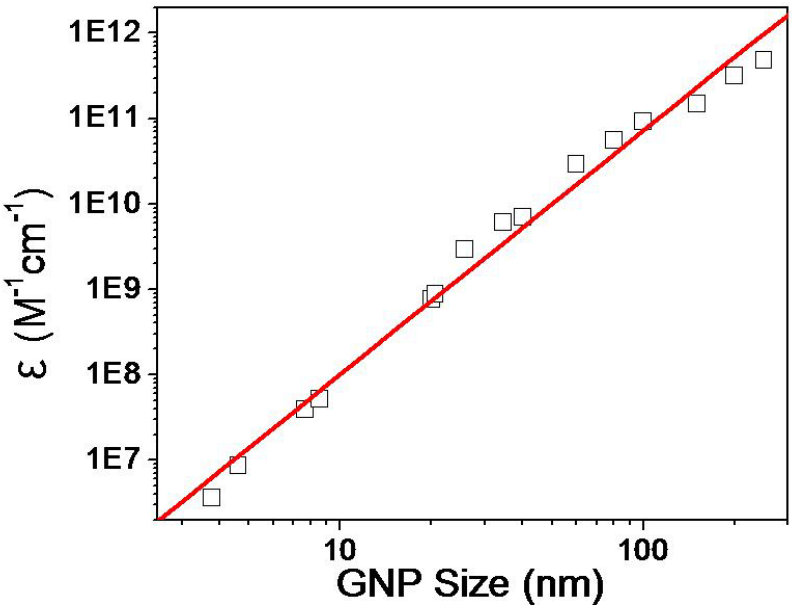

Figure 5- 4. The linear correlation between the extinction and the GNP size in double log scale. ($\ln(\varepsilon)=11.86382+2.85232\ln D$; $R^2=0.99324$)

This finding is also in accordance with the Mie theory as well as the study reported by El-Sayed et al. The *k* and *a* value obtained from our study is 3.32 and 10.8, respectively, while the values for these two parameters are 2.75 and 11.7 from the experimental study, and 3.36 and 8.1 from the theoretical study as reported by El-Sayed et al. Comparing these values, it appears that our experimental result is closer to the theoretical value as calculated by El-Sayed et al. The discrepancy between different studies is most likely due to the slight difference in the average core size and size dispersity of the nanoparticles.[15]

The experimental study reported by El-Sayed was on citrate-stabilized GNPs that were soluble in water. Our results suggest that the linear relationship of the double logarithm of extinction coefficient versus nanoparticle core diameter can be extended to most GNPs independent of the capping ligands used to protect the nanoparticles and the solvents used to dissolve the nanoparticles. The solvents used to dissolve the three types

of nanoparticles synthesized in this study, toluene for decanethiol-protected nanoparticles, THF for oleylamide-protected nanoparticles, and water for citrate-stabilized nanoparticles, have very different dielectric constants (as listed in Table 5-1), varying from 2.4 to 78. The stabilization effect by the capping agents for these three types of nanoparticles is also quite different. The citrate-stabilized nanoparticles rely on electrostatic interactions between the ligands and the nanoparticle core. The decanethiol-protected GNPs are stabilized by covalent bonding between thiolate groups and surface gold atoms, while the oleylamide-protected GNPs depend on hydrogen bonding network formation between amide groups to create a stable environment for nanoparticle core. Although Mie theory indicates that the plasmon resonance absorption of a nanoparticle is related to the dielectric constant of the environmental media around the nanoparticles (which include both solvents and the capping ligands), these effects do not appear to make significant contribution to the extinction coefficient of the surface plasmon resonance band.[7,22]

5.3.3.4 Application of extinction coefficients for GNP concentration determination

Because of the general applicability of the relation of nanoparticle extinction coefficient versus nanoparticle size, one can use the extinction coefficient-core diameter double logarithm curve established in this study as a calibration curve to calculate or estimate the nanoparticle concentration or average diameter of a nanoparticle solution sample. For example, by determine the average size of a nanoparticle sample using TEM, one can obtain the extinction coefficient of the sample. By taking UV-Vis absorption spectra of the sample, the concentration of the sample can be calculated. This will be useful for determining the concentration of biomolecules such as proteins when labeled with GNPs.[23] Most organic molecules and biomolecules have much lower extinction

coefficient than GNPs. By labeling biomolecules with GNPs, the biomolecules can be detected at concentrations as low as sub- nanomolar to picomolar range. This could lead to a very powerful tool at detection of biomarker molecules using a simple spectrophotometer. On the other hand, if the concentration and extinction coefficient of a nanoparticle sample can be determined, the size of the particle may be estimated without imaging analysis by TEM.

5.3.4 Light scattering property of GNPs studied using DLS

After investigating the extinction property of GNPs around their SPR band, we studied the light scattering property of GNPs using DLS. For each size GNP solution, the scattered light intensities at different concentrations were recorded by DLS. The results for GNPs at various sizes ranging from 40 nm to 250 nm were summarized in Figure 5-5.

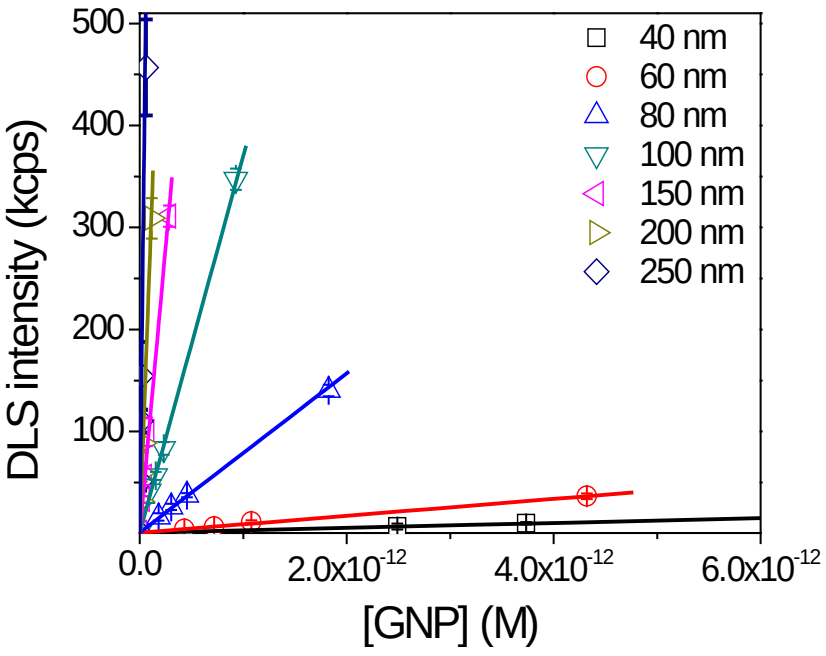

Figure 5- 5. The linear relationship between the DLS intensity and the concentration, respectively for each size GNP

There are some important points to be discussed from Figure 5-5 about the light scattering property of GNPs. First, it can be seen that the light scattering intensity increased linearly along GNP concentration increases. Such linear relationships were observed for GNPs at all sizes investigated in this study. Linear regression curves for the scattering intensity and the GNP concentration were summarized in Table 5-2. These results were different from reported results by reported by Yuegubide et al.[24] In Figure 1-11, the light scattering intensity was linearly dependent with the GNP concentration in double logarithmic scales, respectively for 52, 78, 87 and 118 nm GNPs. In our study, however, the light scattering intensity was directly linearly related to the GNP concentration, respectively for GNPs at sizes from 40 to 250 nm. The discrepancy between these two studies may come from the differences in the experimental setup for the light scattering intensity measurements.

Table 5- 2. GNP detection limits under DLS measurements and linear regression curves between the DLS intensity and the GNP concentration

		Y=A+BX		
GNP size (nm)	LLOD* (M)	A	B	R^2
40	5.95E-13	0.8593	2.37E+12	0.9998
60	1.79E-13	0.784	8.30E+12	0.99739
80	1.73E-14	0.91723	7.80E+13	0.99952
100	3.97E-15	0.80292	3.69E+14	0.99972
150	1.25E-15	0.8739	1.12E+15	0.99883
200	5.14E-16	0.85075	2.76E+15	0.99811
250	1.60E-16	0.85743	8.82E+15	0.98628
*LLOD: Low limit of detection; Y: DLS intensity (kcps); X: GNP concentration (M)				

Second, we can see that the light scattering intensity was different for GNPs solutions at the same concentration but different sizes. Larger size GNPs showed higher light scattering intensity values. According to the Rayleigh theory, the light scattering cross section of a small GNP ($D<0.05\ \lambda$) is proportional to the 6^{th} power of its diameter

(equation 1-8). As a result, when the size of GNP increases, the scattering intensity increases dramatically. For large GNPs (D<0.05 λ), the scattering cross section still increases along the particle size with a correlation smaller that 6th power. In our study, the relative light scattering efficiency for GNPs from 40 to 250 nm was characterized by the slope of the linear regression curve. Results were shown in Table 5-2 and plotted in Figure 5-6. The correlation between the light scattering efficiency and the GNP size can be fitted very well with Lorentz fitting. From Figure 5-6, the light scattering efficiency increases along the GNP size. These results were in accordance with the theoretical calculations by Yuegubide et al.[24]

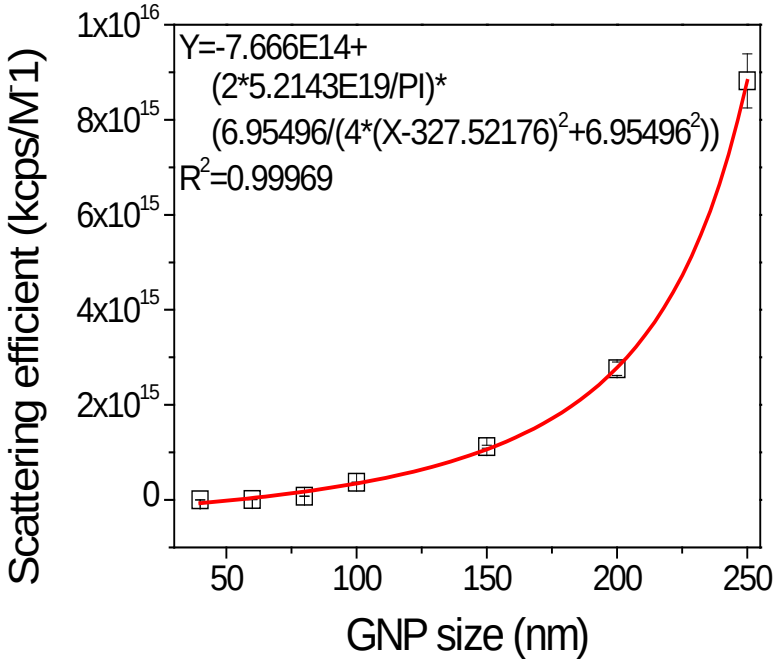

Figure 5- 6. Relative scattering efficiency of GNPs (red curve: Lorentz fitting).

Third, we need to notice that GNPs can be detected by DLS at very low concentrations without any amplification steps. As shown in Figure 5-5, GNPs at concentrations in the range of pM can be detected very easily by DLS. Detection limits of

GNPs in this study were summarized in Table 5-2. For example, the detection limit for 100 nm GNPs is as low as ~4 fM. Such high sensitivities of GNPs detection by DLS are due to the strong scattering property of GNPs. As discussed in section 1.3.2.1, the scattering cross section of GNPs is 4-6 orders of magnitude larger than that of small fluorescence molecules, polystyrene beads or biomolecules. As a result, under a laser irradiation GNPs scatter more lights to be captured by the DLS detector. The strong light scattering property of GNPs and thus the ultra sensitivity in DLS detection make them very promising to be used as ultra sensitive probes in biomolecular detection applications. Based on this, we investigated the applications of GNPs in biomolecular detection in Chapter 6, Chapter 7, and Chapter 8.

5.4 Conclusion

In this work we studied the light extinction and scattering properties of GNPs with core sizes ranging from ~4-250 nm. Extinction coefficients of GNPs were determined by HRTEM analysis and UV-Vis absorption spectroscopic measurements. Three different types of gold nanoparticles were prepared and studied: citrate-stabilized nanoparticles in eleven different sizes; oleylamide-protected gold nanoparticles with a core diameter of 8 nm, and a decanethiol-protected nanoparticle with a diameter of around 4 nm. A linear relationship between the logarithms of extinction coefficients and core diameters of gold particles was found independent of the capping ligands on the particle surface and the solvents used to dissolve the nanoparticles. This linear relation may be used as a calibration curve to determine the concentration or average size of an unknown nanoparticle or nanoparticle-biomolecule conjugate sample. Following the extinction studies, we investigated the light scattering property of GNPs using DLS. We

found out that the light scattering of GNPs were very strong. Very low detection limits were reported for GNPs by DLS detection. In addition, light scattering intensities of GNPs were found to increase linearly along the GNP concentration and non-linearly along the GNP size.

References:

1 Faraday, M. Philos. Trans. R. Soc. London 1857, 147, 145.

2 Daniel, M.-C.; Astruc, D. Chem. Rev. 2002, 104, 293.

3 Burda, C.; Chen, X.; Narayanan, R.; El-Sayed, M.A. Chem. Rev. 2005, 105, 1025.

4 Katz, E.; Willner, I. Angew. Chem. Int. Ed. 2004, 43, 6042.

5 Pissuwan, D.; Valenzuela, S.M.; Cortie, M.B. Trends Biotech. 2006, 24, 62.

6 Kogan, M.J.; Bastus, N.G.; Amigo, R.; Grillo-Bosch, D.; Araya, E. Nano. Lett. 2006, 6, 110.

7 Klar, T.; Perner, M.; Grosse, S.; von Plessen, G.; Spirkl, W.; Feldmann, J. Phys. Rev. Lett. 1998, 80, 4249.

8 Cao, Y.W.C.; Jin, R.; Mirkin, C.A. Science 2002, 297, 1536.

9 Averitt, R.D.; Westcott, S.L.; Halas, N.J. J. Opt. Soc. Am. B 1999, 16, 1824.

10 Taton, T.A.; Lu, G.; Mirkin, C.A. J. Am. Chem. Soc. 2001, 123, 5164.

11 Jones, C.D.; Lyon, L.A. J. Am. Chem. Soc. 2003, 125, 460.

12 West, J.L.; Halas, N.J. Annual Review of Biomedical Engineering 2003, 5, 285.

13 Paciotti, G.; Myer, L.; Weinreich, D.; Goia, D.; Pavel, N. Drug Delivery 2004, 11, 169.

14 Jain, P.K.; Lee, K.S.; El-Sayed, I. H.; El-Sayed, M.A. J. Phys. Chem. B 2006, 110, 7238.

15 Link, S.; El-Sayed, M.A. J. Phys. Chem. B 1999, 103, 8410.

16 Hostetler, M.J.; Wingate, J.E.; Zhong, C.J.; Harris, J.E.; Vachet, R.W.; Clark, M.R.; Londono, J.D.; Green, S.J.; Stokes, J.J.; Wignall, G.D.; Glish, G.L.; Porter, M.D.; Evans, N.D.; Murray, R.W. Langmuir 1998, 14, 17-30.

17 Aslam, M.; Fu, L.; Su, M.; Vijayamohanan, K.; Dravid, V.P. J. Mater. Chem. 2004, 14, 1795.

18 Turkevich, J.; Stevenson, P.C.; Hillier, J. Discuss. Faraday Soc. 1951, 11, 55.

19 Mucic, R.C.; Storhoff, J.J.; Mirkin, C.A.; Letsinger, R.L. J. Am. Chem. Soc. 1998, 120, 12674.

20 Zhang, H.; Hussain, I.; Brust, M.; Cooper, A.I. Advanced Materials 2004, 16, 27.

21 Cui, X.D.; Primak, A.; Zarate, X.; Tomfohr, J.; Sankey, O.F.; Moore, A.L.; Moore, T.A.; Gust, D.; Nagahara, L.A.; Lindsay, S.M. J. Phys. Chem. B 2002, 106,8609.

22 Oldenburg, S.J.; Averitt, R.D.; Westcott, S.L.; Halas, N.J. Chem. Phys. Lett. 1998, 188, 243.

23 Maxwell, D.J.; Taylor, J.R.; Nie, S. J. Am. Chem. Soc. 2002, 124, 9606.

24 (a) Yguerabide, J.: Yguerabide, E.E. Anal. Biochem. 1998, 262, 137-156. (b) Yguerabide, J.: Yguerabide, E.E. Anal. Biochem. 1998, 262, 157-176.

CHAPTER 6. A WASHING-FREE AND AMPLIFICATION-FREE ONE-STEP HOMOGENEOUS ASSAY FOR PROTEIN DETECTION USING GOLD NANOPARTICLE PROBES

6.1 Introduction

Protein detection and analysis plays an extremely important role in in-vitro diagnostics. With the tremendous progresses made in proteomics in the last few decades, there has been a growing demand for highly sensitive, fast and simple techniques for protein analysis using minimum volume of samples and cost effective instrumentations. Many protein biomarkers associated with cancer and other diseases exist in biological fluids and systems with low abundance, typically in the range of fg/mL to ng/mL.[1] How to detect these low abundance biomarker proteins has raised tremendous challenges for bioanalytical chemists. Traditional methods address this difficulty by using amplification labels such as enzymes, radioactive isotopes or fluorescent probes to achieve the required high sensitivity.[2-3] These methods, however, often involve many steps in the assay, including labeling, multiple washing and separation cycles, signal amplification and measurement. These complicated procedures not only make it difficult to automate the assay, but also increase the cost of protein analysis.

Since the middle 1990s, gold nanoparticles (GNP) have been investigated extensively for biomolecular imaging and detection.[4-9] The unique optical properties of GNPs, including their strong absorption and intense light scattering at the surface plasmon resonance wavelength region, aggregation-induced color change,[4] and the surface-enhanced Raman scattering,[5] have been studied in much details in both direct and amplified biomolecular assays.[6] GNPs, when conjugated with a detector antibody, may be used in a traditional heterogeneous sandwich-type immunoassay. The GNP probes

immobilized on a surface due to antibody-antigen binding may be detected optically or electrochemically.[6,7] GNPs have also been used to develop homogeneous biomolecular assays.[4,9] Such assays are based on the detection of nanoparticle aggregation caused by protein-protein interactions or DNA hybridization. GNP aggregation or de-aggregation often leads to optical property changes such as wavelength shifts of the surface plasmon resonance (SPR) bands (or color change),[4] melting temperature increases of the hybridized DNA,[6] fluorescence quenching or enhancement,[8] and surface enhanced Raman scattering.[5] Homogeneous assays offer some unique advantages compared to heterogeneous assays, especially in the simplicity of the assay. However, the sensitivity of homogeneous assays, including the assays involving GNPs as mentioned above, is often not as high as heterogeneous amplification assays. Mirkin et al. developed a bio-bar-code amplification method using DNA bar-code modified GNPs for both protein and DNA detection. Although this method has extremely high sensitivity, the assay involves a complicated multiple-step process that is very difficult to conduct and automate.

Laser light scattering immunoassays (LIA) have been known for more than 3-4 decades.[12,13] Most of these assays are based on immunoaffinity interaction-induced particle aggregation. The level of particle aggregation may be measured using turbidity, nephelometry, angle-dependent scattering intensity, or dynamic light scattering technique. Turbidity and nephelometry are still used substantially in medical diagnostic and environmental testing labs for biomolecule and microorganism detection. In these two assays, light transmitted through or scattered from a turbid assay solution due to particle aggregation is measured and correlated to analyte concentration. However, these two assays typically have very low sensitivity, and are mostly used for high abundance

protein analysis. Dynamic light scattering (DLS), a technique used extensively for characterizing particle size and size distribution, was also applied for particle agglutination-based immunoassays in late 1970s.[13] However, this technique never took off as a main stream immunoassay method for protein analysis due to multiple limitations. First and most important above all, these LIAs including DLS, turbidity, and nephelometry assays, use micron or submicron polymer beads such as latex particles as light scattering enhancers. The light scattering intensity of polymer latex particles, although substantially stronger than biomacromolecules, is still not strong enough to overcome the background scattering from sample matrices. Biological fluids such as blood serum or plasma contain large amounts of nanoparticles and micron scale particles. The intense light scattering from these matrix particles can cause significant interference to the assay. Second, when early attempts were made on using DLS for latex particle-based light scattering immunoassays, DLS was still a relatively high cost instrument, difficult to operate, with limited sensitivity and data analysis capability. Due to these multiple reasons, DLS was not considered as a promising tool for immunoassay applications.

Recently, the extensive study and further understanding on the optical properties of gold nanoparticles (GNPs) has opened many new doors in biomolecular imaging and detection. Gold nanoparticles, including spherical particles, nanorods and nanoshells with a size ranging from 10s to 100s nanometers, are known to have a large light absorption and scattering cross section in the surface plasmon resonance (SPR) wavelength region.[14] In normalized terms, the scattering cross section of a 30 nm gold particle at its SPR region is about 250 times larger than a 30 nm polystyrene particle. As compared to

fluorophores, the scattering light intensity from a 60 nm gold nanoparticle is four to five orders of magnitude higher than a strongly fluorescent fluorescein molecule.[14] Furthermore, the scattering light from nanoparticles does not suffer from the many problems of fluorophores, such as photobleaching, extreme sensitivity to environmental changes. The strong light scattering of gold nanoparticles has enabled many important and promising applications in biomedical field, such as molecular and cell imaging,[15] biosensing, and bioassays.[16]

Scheme 6- 1. Illustration of a one-step homogeneous biomolecular assay using gold nanoparticle probes as light scattering enhancers coupled with dynamic light scattering detection

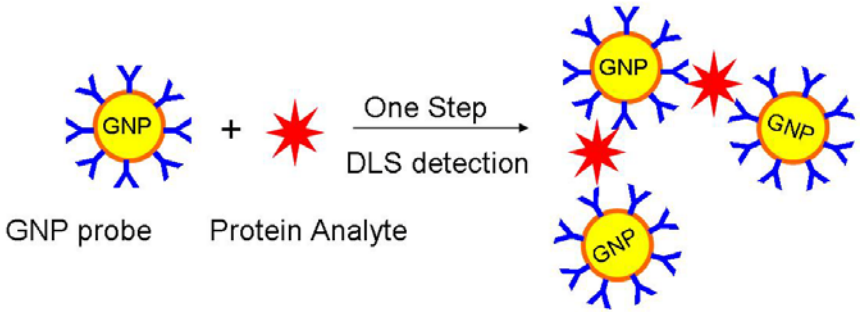

With its strong light scattering, we hypothesized that GNPs could be an excellent light scattering enhancer to replace polymer latex particles for immunoassay development using light scattering techniques. We recently conducted some exploratory studies to demonstrate the proof-of-concept of using GNPs for light scattering assay of both proteins and DNA targets as illustrated in Scheme 6-1. Using a non-competitive assay format, a sandwich type antibody-antigen binding or DNA hybridization was transduced into GNP aggregation formation, which was detected by DLS and subsequently correlated to the target analyte concentration. Due to the extremely strong light scattering intensity of GNPs around their SPR band region, this assay can potentially become a

highly sensitive for biomolecular detection and analysis. It is a single-step, washing-free and amplification free process, therefore, very easy to conduct and automate. In addition, the assay involves the use of very small volumes of samples and GNP probes (total 10 μL or less), which can lead to substantial cost reduction. High throughput 96- or 384-microtiter plate reader is becoming a standard feature of current DLS instruments, which means the new assay developed in our research can be easily adapted for high throughput biomolecular analysis.

In the present work, we conducted a systematic study to examine the sensitivity and dynamic range of this new immunoassay technique, and further developed two formats of competitive and non-competitive homogeneous assays using mouse IgG and goat anti-mouse IgG as a pair of model proteins. This study also revealed some important insights on the nanoparticle aggregation kinetics and its effects on the performance of the immunoassay, especially the dynamic range of the assay. We demonstrated that by properly adjusting the probe concentration and assay conditions, protein analytes may be detected at concentrations as low as pg/mL without any amplification steps.

6.2 Experimental Section

6.2.1 Chemicals and materials

0.01M phosphate buffer saline (NaCl 0.138 M; KCl 0.0027 M, pH 7.4), bovine serum albumin (BSA) powder, and Sepharose CL-2B gel and BiotinTag^{TM} biotinylation kit (cat# B-TAG) were purchased from Sigma-Aldrich (Milwaukee, WI). ChromPure Mouse IgG (whole molecule, IgG concentration 5.5 mg/mL, buffer: 10 mM sodium phosphate, 250 mM NaCl, pH 7.6, preservative: none) was from Jackson ImmunoResearch Laboratories, Inc. (West Grove, PA). Citrate-stabilized GNPs (core

diameter 100 nm), goat anti-mouse IgG (H+L) (AH)-conjugated GNPs (GNP-anti-IgG, core diameter of 40 nm) and streptavidin-conjugated GNPs (GNP-STV, core diameter 40 nm) were purchased from Ted Pella Inc. (Redding, CA). Nanopure water with a conductivity of 18 MΩ·cm was obtained from a Nanopure Diamond^{TM} system (Barnstead International, Dubuque, Iowa).

6.2.2 Preparation of mouse IgG conjugated GNPs (GNP-IgG) and bovine serum albumin-conjugated GNPs (GNP-BSA)

Mouse IgG was labeled with biotin by following the instruction of the biotinylation kit BiotinTag^{TM} from Sigma. 0.75 mL of purified biotin-labeled mouse IgG solution was obtained at a concentration of ~0.7 mg/mL using this kit. To 0.5 mL of 0.1 nM streptavidin-stabilized GNP in PBS buffer, 7 µL of biotin-labeled mouse IgG was added and incubated for 1 h, then centrifuged at 9000 rpm for 4 min and recovered into PBS buffer solution. Bovine serum albumin conjugated gold nanoparticles (GNP-BSA) were prepared using citrate protected 40 nm gold nanoparticles according to a literature report.[10]

6.2.3 Instrumentation

A set of micropipettes (0.5-10 µL, 10-100 µL and 100-1000 µL) from Eppendorf International (Hamburg, Germany) was used for liquid transfer and dilution. A Cary 300 Bio UV-Visible spectrophotometer from Varian Inc. (Palo Alto, CA) was used for UV-Vis spectroscopic study. A PD2000DLS^{PLUS} Dynamic Light Scattering Detector and PDDLS/CoolBatch 40T Dynamic Light Scattering detector system from Precision Detectors Inc. (Bellingham, MA) was used for DLS measurement. The DLS instrument was operated under the following conditions: temperature 20^{o}C, detector angle 90^{o},

incident laser wavelength 683 nm, laser power 100 mW. The DLS data was processed using the Precision Deconvolution software. Each assay solution was diluted into 1.50 mL of nanopure water to the appropriate concentrations and mixed well for 2 min before DLS measurement.

6.2.4 Sensitivity study of a 100 nm GNP by dynamic light scattering

The initial concentration of the 100 nm GNPs as purchased from Ted Pella, Inc. was determined by UV-Vis spectroscopy according to a reported method.[11] The light scattering intensities of nanoparticles at serial dilutions were then measured by DLS with three repeats for each concentration. Lower limit of detection (LLOD) of the 100 nm GNP was calculated from linear fitting curve using $s+3\sigma$ method.

6.2.5 Kinetic study and temperature effect on the aggregation of goat anti-mouse IgG conjugated GNPs (GNP-anti-IgG) and mouse IgG conjugated GNP (GNP-IgG)

100 µL of 0.1 nM GNP-anti-IgG and 100 µL of 0.1 nM GNP-IgG solutions were mixed together and incubated at 37 °C from 1 min up to 19 h. The average diameter of GNPs in solution was monitored by DLS periodically during this time. A control sample was prepared by substituting GNP-IgG with streptavidin-conjugated GNP-STV. Each concentration was run in duplicates. For temperature effect study, an equal volume mixture of GNP-IgG and GNP-anti-IgG was incubated at 4, 25 and 37 °C, respectively. The average diameter of GNPs in the mixture solution was regularly recorded from 1 min up to 24 hours.

6.2.6 A direct assay for mouse IgG using GNP-anti-IgG probes

A mouse IgG stock solution with a concentration of 5.5 mg/mL was used to prepare mouse IgG solutions at concentrations 50000, 5000, 500, 50, 5.0, 0.50, 0.05, and

0.005 ng/mL by serial dilutions. In the process, a 0.1% BSA solution (buffer: 10 mM PBS, 0.154 M NaCl, pH=7.4) after filtering through a 0.2 μm membrane was used as the sample dilutant and also as the control sample. The stock solution of 1 nM GNP-anti-IgG was purified by column chromatography using a Sepharose CL-2B gel column to eliminate any non-conjugated goat anti-mouse IgG. The purified solution was filtered through a 0.2 μm membrane and then diluted into 0.1, 0.01 and 0.001 nM solutions. In a first assay, 20 μL of mouse IgG solution was mixed with 60 μL of GNP-anti-IgG probe solution at a concentration of 0.1 nM, and the assay solution was incubated at 37 °C for 2 hours. The average hydrodynamic diameter of the assay solution between 20 and 400 nm, D_h, was then measured by DLS. Particles with sizes beyond this range were not included in the data analysis. A control study was performed under the same conditions using BSA conjugated GNP probes (GNP-BSA). In a second and third assay, the concentration of GNP-anti-IgG was reduced to 0.01 nM or 0.001 nM by 0.1% BSA solution, with all other conditions remained the same as used in the first assay.

6.2.7 A competitive assay for mouse IgG detection

60 μL of 0.1 nM GNP-anti-IgG solution, 60 μL of 0.1 nM GNP-IgG, and 20 μL of mouse IgG solutions with different concentration were mixed together and incubated at room temperature for 4.5 h. Particle size of the incubated solution was then measured by DLS.

6.3 Results and Discussions

6.3.1. Sensitivity of GNP detection by dynamic light scattering

We previously reported that the detection limits for a 40 nm spherical GNP, and a 10 by 40 nm gold nanorod (GNR) can reach 0.02 and 0.4 pM, respectively. In the present

study, we further examined the detection limit of a 100 nm spherical GNP by DLS. For our assay purpose, what actually needs to be detected is nanoparticle aggregates instead of individual gold nanoparticles. Since the GNP probes used in this study has an average diameter of 40 nm, a GNP with a diameter of 100 nm can be viewed as approximately equivalent to a dimer of a 40 nm GNP, the smallest aggregate to be present in the assay solution. Therefore, the detection limit of 100 nm GNPs is a good indication of the potential sensitivity of the immunoassay investigated in this study. The detection limit study of the 100 nm GNPs is shown in Figure 6-1. Similar to smaller size GNPs, there is a linear relationship between nanoparticle concentration and scattered light intensity. The lower limit of detection (LLOD) of this 100 nm GNP was determined to be around 0.7 fM, a 30 fold improvement compared to the 40 nm GNP. According to theoretical calculations,[14] the light scattering cross section of GNPs increases dramatically when the diameter of GNPs is above 80-100 nm. The sensitivity of DLS for GNP detection is also related to the wavelength and power of the laser. By increasing the gold nanoparticle size and varying the instrumental set-up, it is possible that GNPs can be detected at concentrations lower than fM, even at attomolar and zeptomolar (aM and zM) ranges. Furthermore, because the light scattering intensity is proportional to the particle size, the sensitivity of DLS for nanoparticle aggregation can be significantly higher than individual nanoparticles. Gold nanoparticles should be excellent light scattering enhancers to replace polymer latex particles for laser light scattering immunoassay applications.

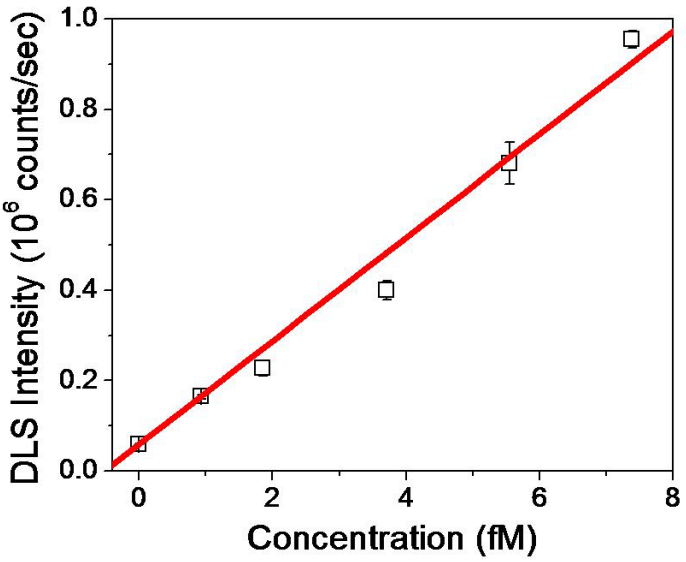

Figure 6- 1. Light scattering intensity of a 100 nm gold nanoparticle at different concentrations as determined from DLS measurement. (y=0.02758+119.47x, R^2=0.99212; LLOQ=0.7 fM according to 3σ, error bar: standard deviation; each data is the average result of three measurements) (Copyright ® 2009 Elsevier B.V.)

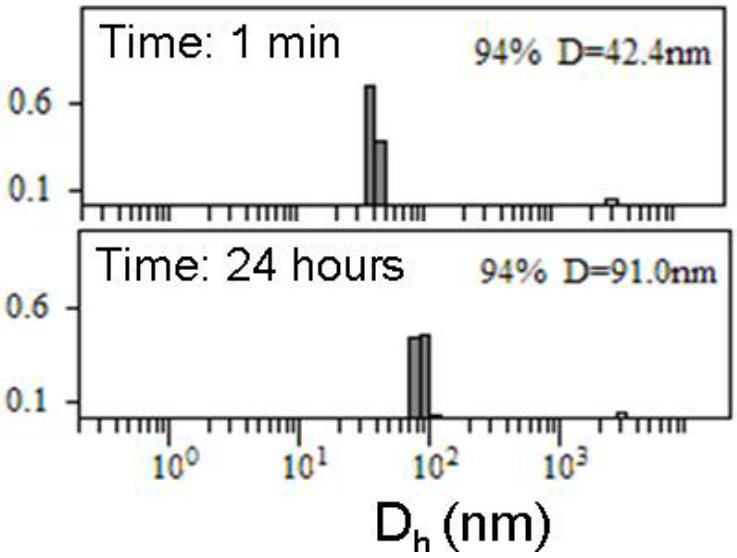

Figure 6- 2. Particle size and size distribution of a 1:1 mole ratio mixture of goat anti-mouse IgG conjugated GNPs (GNP-anti-IgG) and mouse IgG conjugated GNPs (GNP-IgG) measured immediately after mixing and after incubation at room temperature for 24 hours (the concentration of both GNP probes was 0.1 nM) (Copyright ® 2009 Elsevier B.V.)

6.3.2 Kinetics of nanoparticle aggregation between two complementary GNP immunoprobes

In particle agglutination immuoassays, a good understanding on the whole nanoparticle aggregation process is ultimately important for the assay development. Using a pair of primary and secondary antibody as model proteins, we first studied the aggregation kinetics of two GNP particles: one is GNPs conjugated with goat anti-mouse IgG (GNP-anti-IgG), and the other one is GNPs conjugated with mouse IgG (GNP-IgG). The GNP-IgG particles were prepared by conjugating biotinylated mouse IgG to a streptavidin-coated GNPs. The core diameter of the GNP probes is around 40 nm. When these two particles are mixed together, the binding between mouse IgG and goat anti-mouse IgG should cause nanoparticle aggregation. Shown in Figure 6-2 is a size distribution graph of the mixed particle solution as measured by DLS. With increased incubation time, the average size of the particle solution increased clearly. Figure 6-3 is the measured average particle size, expressed in hydrodynamic diameter D_h, of the solution recorded at different time. Over 24 hours, the average particle size increased almost linearly from 42 nm to 90 nm. In a control experiment, when GNP-anti-IgG was mixed with streptavidin-coated GNPs (GNP-STV) and incubated for the same amount of time, the average particle size of the solution remained the same as the initial solution through out the whole incubation period. This experiment demonstrates the capability of DLS to quantitatively detect and monitor the immunoaffinity interaction-induced nanoparticle aggregation process. We also examined the incubation temperature effect on this process. An equal amount of mixture of GNP-IgG and GNP-anti-IgG was incubated

at three temperatures: 4, 25, and 37 ^{o}C, respectively. At elevated temperature, the nanoparticles aggregated much faster than at lower temperatures (Figure 6-4).

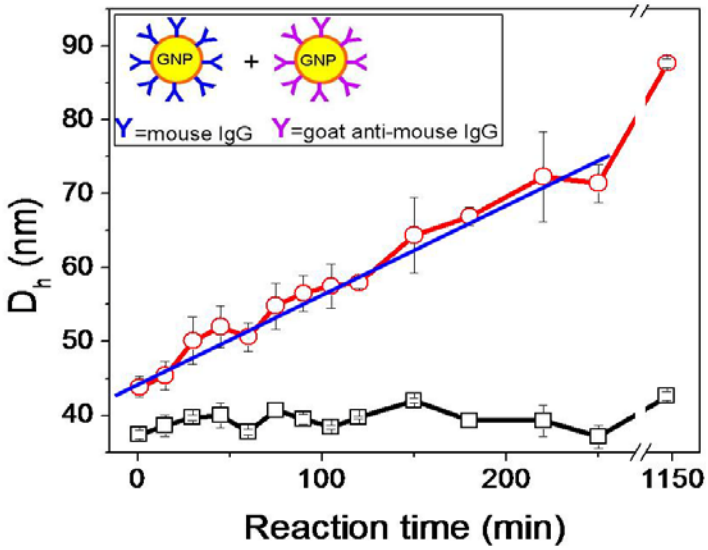

Figure 6- 3. The hydrodynamic diameter change of gold nanoparticle in two mixed nanoparticle probe solutions over 19 hours of incubation at ambient conditions. (-○-: mixture of GNP-anti-IgG and GNP-IgG; -□-: mixture of GNP-anti-IgG and GNP-STV. Linear fitting from 1 to 250 min: y=44.20632+0.11925x, R^2=0.98915; error bar: standard deviation; each data point is the average result of two experiments) (Copyright ® 2009 Elsevier B.V.)

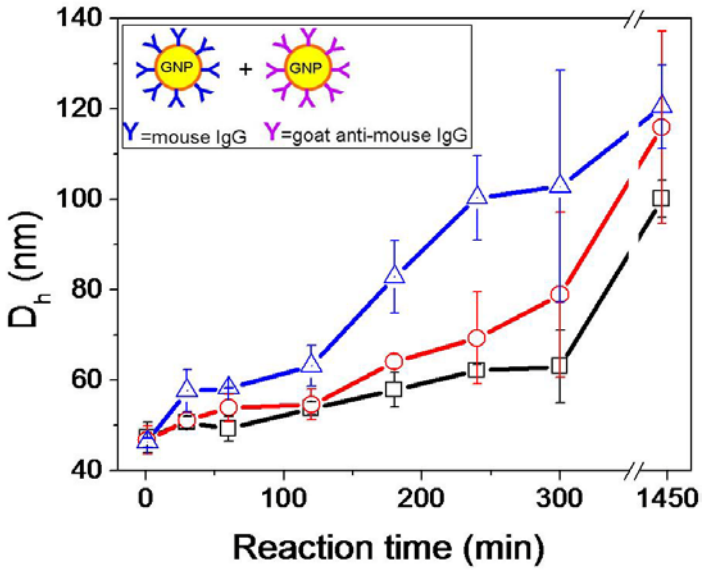

Figure 6- 4. The growth of nanoparticle size for an equal volume mixture of 0.1 nM GNP-anti-IgG and 0.1 nM GNP-IgG incubated at different temperatures for up to 24 hours. (-□-: 4 ^{o}C; -○-: 25 ^{o}C; -Δ-: 37 ^{o}C; error bar: standard deviation; each data is the average of three experiments) (Copyright ® 2009 Elsevier B.V.)

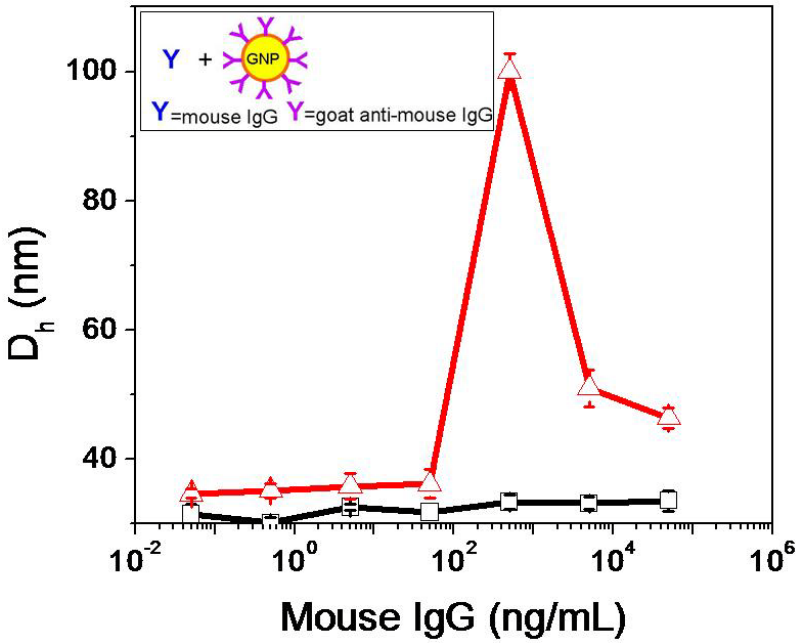

Figure 6- 5. The hydrodynamic diameter change of assay solutions of mouse IgG mixed with two different gold nanoparticle probes after incubating at 37 ^{o}C for 2 hours. (-□-: a control made of mouse IgG with 0.1 nM BSA conjugated GNPs; -Δ-: mouse IgG mixed with a 0.1 nM goat-anti mouse conjugated GNPs; rrror bar: standard deviation; each data is the average of two experiments) (Copyright ® 2009 Elsevier B.V.)

6.3.3 Detection of mouse IgG using goat anti-mouse IgG conjugated GNPs

Goat anti-mouse IgG, a secondary antibody, can bind with primary antibody mouse IgG on its Fab, Fab' or Fc region. Because of these multiple binding sites, mouse IgG can cross link nanoparticle probes into oligomers or larger aggregates. A homogeneous immunoassay for mouse IgG can be designed and developed using the secondary antibody conjugated GNPs. Mouse IgG solutions with concentrations covering a six-orders of magnitude range from 0 ng/mL to 50,000 ng/mL were assayed. The assay solution was incubated at room temperature for 2h. As shown in Figure 6-5, overall, the nanoparticle size increased with increasing mouse IgG concentration. From mouse IgG concentration 0.05 to 50 ng/mL, the particle size increase was rather limited, and between 50 to 500 ng/mL, the particle size increase became significant. When the concentration of

mouse IgG was further increased to 5,000 and 50,000 ng/mL, the particle size actually decreased, leading to an interesting bell-shaped curve. Such a response curve is similar to a well known immuno-precipitation assay curve from antigen-antibody binding and referred to as the Heidelberger-Kendall curve.[16] This phenomenon is also known as the "hook effect", which is commonly observed in particle agglutination immunoassays. The antibody-antigen binding-induced particle aggregation process can be divided into three different zones. At relatively low antigen concentrations (here is the mouse IgG), the particles will form relatively small oligomers/clusters due to the crosslinking effect of small amount of antigens. In this zone, the average particle size increases linearly or logarithmically with increased antigen concentration. At a certain antigen concentration, such nanoparticle size increase will reach a maximum, the so-called "hook point". Further increase of antigen concentration will lead to a decreased degree of particle aggregation, because there are enough antigens to bind with each antibody on the nanoparticle surface, therefore, less particle crosslinking will occur. The relative ratio of the nanoparticle probes versus antigen in an assay solution determines when the "hook point" shall occur.

For particle agglutination assays, the "hook point" is approximately the upper limit of the dynamic range of the assay. The "hook point" for the assay as shown in Figure 6-5 appeared at a mouse IgG concentration around 500 ng/mL. "Hook point" also affects the precision of an assay. When substantial nanoparticle aggregation starts to form, the precision of the analysis through particle size measurement will typically decrease. This was clearly noticed from the results as shown in both Figure 6-3 and 6-4. However, at relatively low antigen concentration, the particle size change of the assay solution was

not very significant, as the case shown in Figure 6-5, due to relatively high concentration of probe particles.

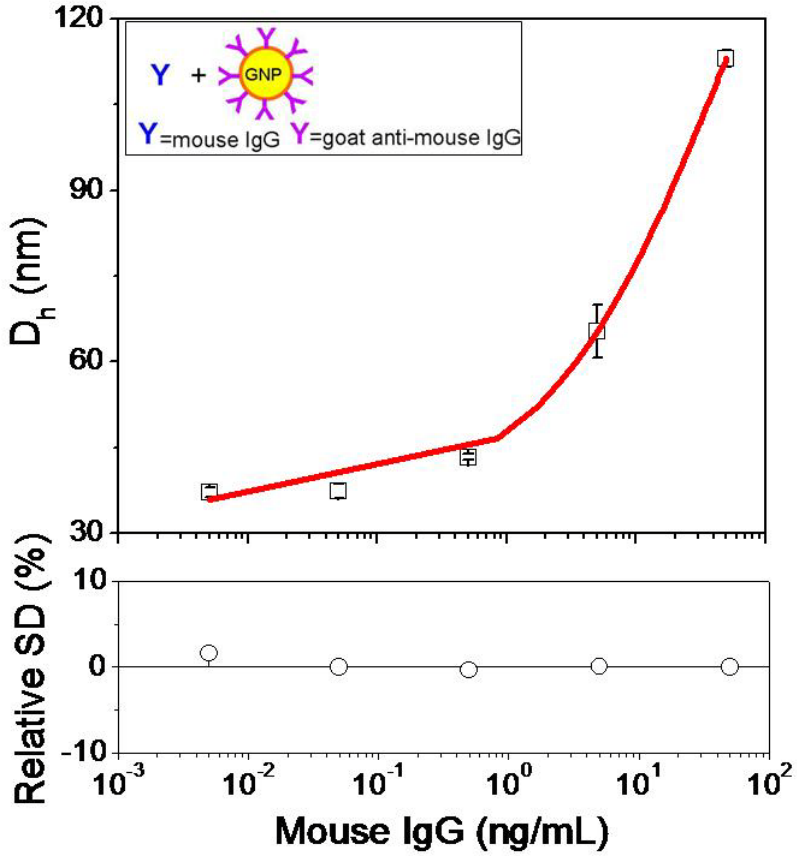

Figure 6- 6. A direct assay for mouse IgG detection using 0.01 nM goat anti-mouse IgG conjugated GNPs. Measured data was fitted into a logistic model using a four parameter Logistic fitting without weighting. (LLOD=0.0078 ng/mL, 3σ, R=2; $y=187.55435+(35.46758-187.55435)/(1+x/46.97037)^{0.6302}$, $R^2=0.9994$; error bar: standard deviation; each data is the average of two experiments) (Copyright ® 2009 Elsevier B.V.)

To improve the sensitivity of the assay at low analyte concentration range, we diluted the GNP probes 10 times from 0.1 nM to 0.01 nM and mouse IgG solutions with a concentration from 0 to 50 ng/mL were assayed. As shown in Figure 6-6, the particle size increase at low mouse IgG concentrations became much more obvious. At the same antigen concentration, the percentage of nanoparticle aggregation increases naturally with

a lower nanoparticle probe concentration, leading to improved sensitivity of the detection. The growth of the nanoparticle hydrodynamic diameter D_h can be fitted into a Logistic model, with a CV% of the fitting curve below 10% for all points.[18] The dynamic range of this assay for mouse IgG is estimated to cover four to five orders of magnitude from 0.0078 to 50 ng/mL. This dynamic range and the sensitivity are on par with or substantially better than ELISA and some other sandwich immunoassays. This example of study illustrates that by selecting the appropriate nanoparticle probe concentration, one can adjust the sensitivity and dynamic range of the assay rather conveniently.

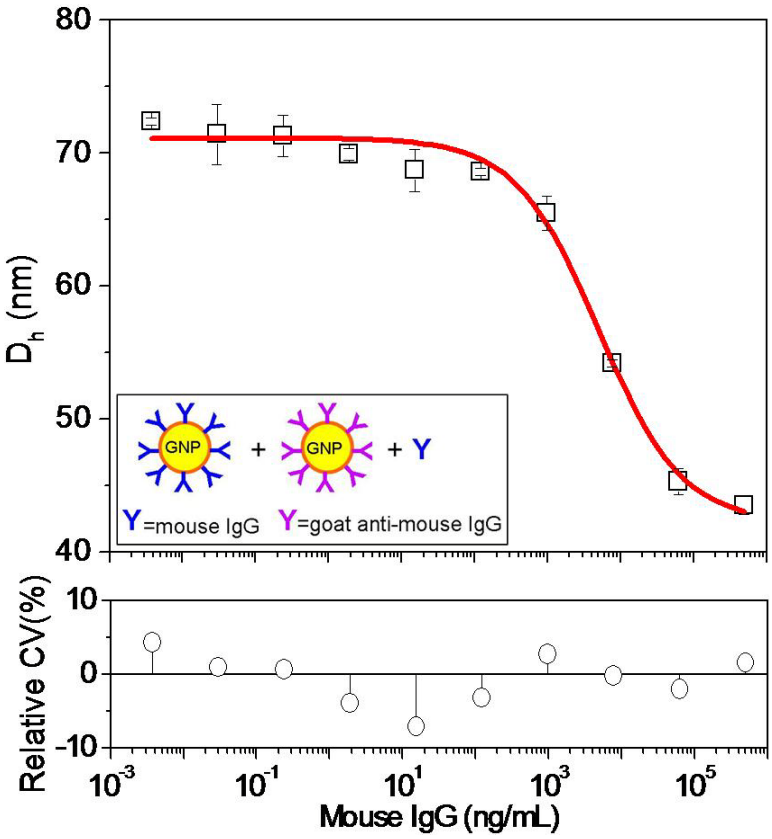

Figure 6- 7. A competitive assay for mouse IgG detection using two nanoparticle probes, GNP-IgG and GNP-anti-IgG. The concentration of both GNP probes was 0.1 nM. Each assay solution was incubated at room temperature for 4.5 hours. Measured data was fitted into a logistic model using a four parameter Logistic fitting without weighting. (LLOD=283.0036 ng/mL, 3σ, R=2; y=42.21247+(71.12096-

42.21247)/(1+x/5023.40461)$^{0.76428}$, R^2=0.9895, error bar: standard deviation; each data is the average of two experiments) (Copyright ® 2009 Elsevier B.V.)

6.3.4 A competitive immunoassay for mouse IgG using two nanoparticle probes

Other than adjusting the nanoparticle probe concentration and manipulating the assay conditions, an alternative approach to eliminate the problem of "hook effect" is to use a competitive assay format. Competitive assays have been reported previously for microparticle or nanoparticle-based assays.[4,9,12] In this study, a one step competitive homogenous assay for mouse IgG detection was performed by using two matching GNP probes, GNP-IgG and GNP-anti-IgG. Aggregation of these two GNP probes would reach the maximum when there is no mouse IgG in the sample solution, while no aggregation should be observed when there are excess amounts of mouse IgG in the sample solution. Indeed, as revealed from particle size measurement as shown in Figure 6-7, the average hydrodynamic diameter of the assay solution decreased with increased mouse IgG concentration. The particle size decrease versus analyte concentration curve may also be fitted into a logistic model, with a relative CV% less than 10% for all the data points.[18] Although the decrease of particle size at low analyte concentration is relatively small and the sensitivity of the assay is not as good as the sandwich-type assays, this approach avoided the "hook effect" encountered in the non-competitive assay. Another advantage of competitive assays is that the assay does not require at least two independent binding sites on the analyte molecules or two matched monoclonal antibodies. This advantage is especially useful when only one antibody is available for a target antigen. In principal, a secondary antibody-conjugated GNP and a primary antibody conjugated-GNP can be paired together to develop competitive assay for essentially any protein antigen

molecules. With these two important advantages, competitive assays are as promising as non-competitive assays and merit further investigation and development.

6.4 Conclusion

In summary, through this study, we demonstrate that gold nanoparticles with their strong light scattering property can be used as a highly sensitive optical probe to replace traditional polymer latex particles for laser light scattering immunoassay applications. The sensitivity and dynamic range of such assays can be adjusted very conveniently to the expected range by selecting appropriate nanoparticle probe concentrations and assay conditions. Both competitive and non-competitive assay formats may be considered in the actual assay development for each individual protein analyte. With the extremely high sensitivity of DLS for gold nanoparticle and nanoparticle aggregation detection, modernized DLS instruments and high throughput sample handling capability, we believe laser light scattering immunoassay can be re-vitalized into a very powerful bioanalytical technique for protein analysis.

References:

1 (a) Sahab, Z.J.; Semaan, S.M.; Sang, Q.-X. Biomarker Insights 2007, 2, 21-43. (b) Wu, J.; Fu, Z.; Yan, F.; Ju, H. Trends Anal. Chem. 2007, 26, 679-688. (c) Paliouras, M.; Borgono, C.; Diamandis, E.P. Cancer Lett. 2007, 249, 61-79.

2 (a) Alivisatos, P. Nat. Biotech. 2004, 22, 47-52. (b) M. C. Daniel and D. Astruc, Chem. Rev., 2004, 104, 293–346. (c) Rosi, N.L.; Mirkin, C.A. Chem. Rev. 2005, 105, 1547-1562. (d) Wilson, R. Chem. Soc. Rev. 2008, 37, 2028-2045.

3 (a) Diamandis, E.P.; Christopoulos, T.K. Immunoassay. San Diego: Academic Press, c1996. (b) Elshal, M.D.; McCoy Jr., J.P. Methods 2006, 38(4), 317-323.

4 Tsai, C.-S.; Yu, T.-B.; Chen, C.-T. Chem. Commun., 2005, 4273-4275.

5 Bonham, A.J.; Braun, G.; Pavel, I.; Moskovtis, M.; Reich, N.O. J. Am. Chem. Soc. 2006, 129, 14572-14573.

6 (a) Mirkin, C.A.; Letsinger, R.L.; Mucic, R.C.; Storhoff, J.J. Nature 1996, 382, 607-609. (b) Nam, J.M.; Thaxton, C.S.; Mirkin, C.A. Science 2003, 301, 1884-1886.

7 Pingarron, J.M.; Yanez-Sedeno, P.; Gonzalez-Cortes, A. Electrochimica Acta 2008, 53, 5846-5866. (b) Das, J.; Aziz, M.A.; Yang, H. J. Am. Chem. Soc. 2006, 128, 16022-16023. (c) Wu, J.; Yan, Y.; Yan, F.; Ju, H. Anal. Chem. 2008, 80, 6072-6077.

8 You, C.-C., Miranda, O.R.; Gider, B.; Ghosh, P.S.; Kim, I.-B., Erdogan, B.; Krovi, S.A.; Bunz, U.H.F.; Rotello, V.M. Nat. Nanotech. 2007, 2, 318-323.

9 Lee, J.-S.; Ulmann, P.A.; Han, M.S.; Mirkin, C.A. Nano Lett. 2008, 8, 529-533.

10 (a) Liu, X.; Dai, Q.; Austin, L.; Coutts, J.; Chen, H.; Zou, J. J. Am. Chem. Soc. 2008, 130, 2780-2782. (b) Dai, Q,; Liu, X.; Coutts, J.; Austin, L.; Huo, Q. J. Am. Chem. Soc. 2008, 130, 8138-8139.

11 Liu, X.; Atwater, M.; Wang, J.; Huo, Q. Coll. and Surf. B: Biointerfaces 2007, 58, 3-7.

12 Bangs, L.B. Pure & Appl. Chem. 1996, 68, 1873-1879.

13 (a) Berne, B.J.; Pecora, R. Dynamic ligh scattering: with applications to chemistry, biology, and physics; Wiley: New York, 1976. (b) Cohen, R.J.; Benedek, G.B. Immunochemistry 1975, 12, 963-966. (c) Antony, T.; Saxena, A.; Roy, K.B.; Bohidar, H.B. J. Biochem. Biophys. Methods 1998, 36, 75-85.

14 (a) Jain, P.K.; Lee, K.S.; El-Sayed, I.H.; El-Sayed, M.A. J. Phys. Chem. B 2006, 110, 7238-7248. (b) Link, S.; El-Sayed, M.A. J. Phys. Chem. B. 1999, 103, 8410-8426. (c) Pecora, R. J. of Nanoparticle Research 2000, 2, 123-131. (d) Xie, H.; Gill-Sharp, K.L; O'Neal, D.P. Nanomed.: Nanotech., Bio., and Med. 2007, 3, 89-94.

15 (a) Wang, H.; Brandle, D.W.; Nordlander, P.; Halas, N.J. Acc. Chem. Res. 2007, 40, 53-62. (b) Aslan, K.; Lakowicz, J.R.; Geddes, C.D. Curr. Opion. Chem. Biol. 2005, 9, 538-544. (c) Huang, X.; El-Sayed, I.; Qian, W.; El-Sayed, M.A. J. Am. Chem. Soc. 2006, 128, 2115-2120.

16 (a) Yguerabide, J.; Yguerabide, E.E. Anal. Biochem. 1998, 262, 137-156. (b) D.A. Schultz. Curr. Opin. Biotech. 2003, 14, 13-22. (b) Huo, Q. Colloid Surf. B. 2007, 59, 1-10. (c) Du, B-A.; Li, Z-P.; Liu, C-H. Angew. Chem. Int. Ed. 2006, 45, 8022-8025. (d) Russier-Antoine, I.; Huang, J.; Benichou, E.; Bachelier, G.; Jonin, C.; Brevet, P-F. Chem. Phys. Lett. 2008, 450, 345-349. (e) Ray, P.C. Angew. Chem.

Int. Ed. 2006, 45, 1151-1154. (f) Hirsch, L.R.; Jackson, J.B.; Halas, N.J.; West, J.L. Anal. Chem. 2003, 75, 2377-2381. (g) Xu, X.; Georganopoulou, D.G.; Hill, H.D.; Mirkin, C.A. Anal. Chem. 2007, 79, 6650-6654.

17 (a) Heidelberger, M.; Kendall, F.E. J. Exp. Med. 1929, 50(6), 809-823. (b) Heidelberger, M.; Kendall, F.E. Science 1930, 72, 252-253. (c) Heidelberger, M.; Kendall, F.E. J. Exp. Med. 1935, 61(4), 563-591. (d) Rappaport, I. J. Immunol. 1957, 78, 246-255.

18 (a) Lee, J.W.; Devanarayan, V.; Barrett, Y.C.; Weiner, R.; Allinson, J. ; Fontain S.; Keller, S.; Weinryb, I.; Green, M.; Duan, L.; Rogers, J.A.; Millham, R.; O'Brien, P.J.; Sailstad, J.; Khan, M.; Ray, C.; Wagner, J.A. Pharm. Res. 2006, 23, 312-328.

CHAPTER 7. A ONE-STEP HOMOEGENOUS IMMUNOASSAY FOR CANCER BIOMARKER DETECTION USING GOLD NANOPARTICLE PROBES COUPLED WITH DYNAMCI LIGHT SCATTERING

7.1 Introduction

Highly sensitive detection and accurate analysis of biomarker molecules in human fluid samples are essential for early detection, treatment and management of cancer. For a typical sandwich-type immunoassay which is routinely used for protein biomarker detection, a capture antibody against a specific biomarker protein is first immobilized on a microtiter plate. After the binding of antigen from a sample solution, a labeled detector antibody is allowed to bind with the immobilized antigen. The concentration of the antigen can then be determined by indirectly measuring the concentration of the probe attached to the detector antibody, which include enzymes, fluorescence tags, DNA-barcodes, etc.[1] A typical heterogeneous immunoassay involves antibody immobilization, multiple steps of incubation and washing cycles, followed by the signal amplification and reading step. From the initial antibody immobilization to the final reading of the assay results, the entire immunoassay can usually take hours to days to complete. A traditional immunoassay is rather time-consuming and labor-intensive. To overcome these problems, the development of single-step, washing-free homogeneous immunoassays has been of tremendous interest and value to the scientific community.[2]

GNPs, including spherical particles, nanorods and nanoshells with a size ranging from 10s to 100s nanometers, are known to have a large light absorption and scattering cross section in the surface plasmon resonance wavelength region.[3] The magnitude of light scattering by a gold nanoparticle can be orders of magnitude higher than light

emission from strongly fluorescing dyes. This unique property has enabled many important and promising applications of metal nanoparticles in biomedical field, such as molecular and cell imaging, biosensing, bioassays, and photothermal therapy.[4] However, the strong light scattering property of GNPs has been mainly applied to optical microscopic imaging of biological cells for qualitative evaluation, but much less frequently for quantitative analysis and assays.

Dynamic light scattering (DLS), also known as photon correlation spectroscopy or quasi elastic light scattering, is a technique used widely for particle size and size distribution studies. This technique is based on the Brownian motion of spherical particles which causes a Doppler shift of incident laser light. The diffusion constant of particles are measured and the size of the particles is calculated according to the Stokes-Einstein relation.[5] DLS is used routinely to analyze the size and size distribution of polymers, proteins, colloids and nanoparticles. Because of the strong light scattering property of GNPs, it is natural to hypothesize that DLS can be a very sensitive technique for quantitative detection and analysis of nanoparticle probes at low concentration.[6] Indeed, it has been demonstrated that DLS can be used to monitor the gold nanoshell concentration in whole blood samples after intravenous injection of nanoparticles in a murine tumor model[6a] and enzyme to quantum dots interactions.[6b] Although extensive studies have been reported on bioconjugation of GNPs and biomolecular interaction-directed nanoparticle assembling, to our surprise, DLS has not been used in conjunction with gold nanoparticle probes for homogeneous and quantitative immunoassay. DLS can distinguish individual nanoparticles versus nanoparticle dimers, oligomers or aggregates

because of their particle size differences, and this capability makes DLS a potential analytical tool for a quantitative immunoassay.

Scheme 7- 1. A schematic illustration of a homogeneous immunoassay using antibody-conjugated nanoparticles and nanorods coupled with dynamic light scattering measurement (GNP: citrate-protected GNPs, DAB: anti-f-PSA detector antibody, GNR: gold nanorods, CAB: anti-f-PSA capture antibody)

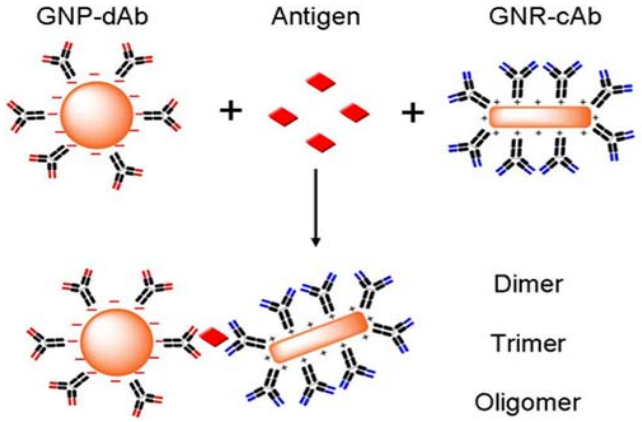

Prostate specific antigen (PSA), is an FDA-approved biomarker for prostate cancer diagnosis. The total PSA concentration of a healthy male is in the range of a few ng/mL and the free PSA (f-PSA) concentration is typically less than 1 ng/mL, in the range of 10% of the total PSA.[7] Free PSA is the unbound form of prostate specific antigen. Studies have shown that the percentage of f-PSA in total PSA is lower in patients with prostate cancer than those with benign prostate hyperplasia. The free to total PSA ratio is now being introduced and studied as an additional tool for prostate cancer diagnosis. We herein report the development of a highly sensitive one-step homogeneous immunoassay for free PSA detection using gold nanoparticle probes coupled with dynamic light scattering analysis. As illustrated in Scheme 7-1, two different types of GNPs (here one is a spherical nanoparticle and one is a nanorod), are to be conjugated with an anti-f-PSA antibody pair, one with a capture antibody and one with a detector

antibody. When these two bioconjugated nanoparticles are mixed in a sample solution that contains antigen f-PSA, the binding of f-PSA will cause nanoparticles to form dimers, oligomers, or aggregates, depending on the concentration of the antigen. Through DLS analysis, the relative ratio of nanoparticle dimers, oligomers, or aggregates versus individual nanoparticles can be measured quantitatively. This ratio should increase accordingly with increased amount of antigen in sample solution, and such a correlation will form the analytical basis of a homogeneous immunoassay.

7.2 Experimental

7.2.1 Chemicals and materials

Hydrogen tetrachloroaurate(III) hydrate ($HAuCl_4$) was purchased from Strem Chemicals (Newburyport, MA). Trisodium citrate, 0.01M phosphate buffer saline (NaCl 0.138 M; KCl 0.0027 M, pH 7.4), poly-L-lysine (M.W. 93,800), dialysis tubing cellulose membrane (MWCO 3,500) and 70% nitric acid (redistilled, 99.999+%) were purchased from Sigma-Aldrich (Milwaukee, WI). Goat anti-mouse IgG (H+L) (AH) conjugated 5 nm GNPs (product #: 15750) were purchased from Ted Pella Inc. (Redding, CA). Mouse anti-human PSA monoclonal antibody (capture antibody) (cat. # T40081A, clone # CHYH1), mouse anti-human PSA monoclonal antibody (detector antibody) (cat. # T40081B, clone # CHYH2), ELISA kits for human free-PSA (Cat.# 10050) and ELISA kits for CA125 were obtained from Anogen-YES Biotech Laboratories Ltd. (Mississauga, Canada). The 10 ng/mL free-PSA standard solution was used for preparation of free-PSA solutions with lower concentrations obtained using sample dilutant provided in the ELISA kit. The 10 ng/mL free-PSA standard solution was prepared in a protein matrix solution according to the WHO standard by the vendor. Free-PSA antigen standards,

CA125 antigen standards, and monoclonal antibodies were reconstituted with appropriate volumes of nanopure water according to the procedure provided by the vendor. Nanopure water was obtained from a Nanopure Diamond^{TM} system (Barnstead International, Dubuque, Iowa). Aqueous solutions of 1.0% magnesium nitrate and 0.2% palladium nitrate were purchased from Buck Scientific (East Norwalk, CT) and used for the preparation of matrix modifier solutions for graphite furnace atomic absorption spectroscopy (GFAAS) analysis of GNPs.

7.2.2 Instrumentation

A set of micropipettes (0.5-10 uL, 10-100 uL and 100-1000 uL) from Eppendorf International (Hamburg, Germany) was used for liquid transfer and dilution. A conductivity meter, TwinCond Conductivity Meter B-173 (Horiba, Japan), was used to monitor the purification of GNPs from residual ions in product solution. High resolution transmission electron microscopic study (HRTEM) was conducted on a FEI Tecnai F30 TEM (FEI Company) at an acceleration voltage of 200 keV. Samples for HRTEM analysis were prepared by pipeting 5 uL sample solution on a poly-L-lysine (0.0381 g/mL in 1:3 H_2O:MeOH mixture solvent) treated 400 mesh carbon/formvarcoated copper grids followed by vacuum drying for 30 min and put in room temperature for at least one overnight before HRTEM measurements. Average size and size distribution of GNPs and gold nanorods were analyzed by ImageJ software. A Cary 300 Bio UV-Visible spectrophotometer from Varian Inc. (Palo Alto, CA) was used for UV-Vis spectroscopic study. A PD2000DLS^{PLUS} Dynamic Light Scattering Detector and a PDDLS/CoolBatch 4oT Dynamic Light Scattering detector system from Precision Detectors Inc. (Bellingham, MA) were used for dynamic light scattering (DLS) measurement. The DLS

instrument was operated under the following conditions: temperature 20^{o}C, detector angle 90^{o}, incident laser wavelength 683 nm, laser power 100 mW. The DLS data without molecular normalization was processed using the Precision Deconvolve software. Samples for DLS analysis were diluted in 1.50 mL nanopure water to the appropriate concentration and mixed well and sit for 2 min before each measurement. The graphite furnace atomic absorption spectroscopy (GFAAS) analysis of gold nanoparticle and nanorod products was conducted using a Model 210-VGF Atomic Absorption Spectrometer from Buck Scientific (East Norwalk, CT). Matrix modifier for GFAAS analysis was prepared by mixing 1.00 mL of 1.0% magnesium nitrate solution, 1.00 mL of 0.2% palladium nitrate solution and 2.00 mL of wt.2% nitric acid solution (70%, redistilled, 99.999+%). The atomization temperature was set as 2300 ^{o}C for gold element analysis. For each measurement, 20.0 uL of samples solution was mixed with 5.0 uL of matrix modifier into the furnace tube to optimize atomic absorption intensities.

7.2.3 Gold nanoparticle (GNP) synthesis, purification and conjugation to antibodies

Citrate-stabilized GNPs with an average diameter 37 nm were synthesized according to Turkevich method (1, 2). Briefly, 6 mg of hydrogen tetrachloroaurate(III) hydrate was dissolved in 50 mL of nanopure water in a round bottom flask and boiled for 15 minutes, followed by addition of 0.5 mL 38 mM trisodium citrate solution in nanopure water. Boiling was extended for another 15 minutes and then the solution was cooled down to ambient temperature. Residual free ions in solution were removed by dialysis of the solution using a cellulose membrane (MWCO=3500) against nanopure water for 2 days and monitored with ionic conductivity measurement. Conductivity of the nanoparticle solution was measured to be 18 ms/cm before dialysis and below 1 μs/cm

after dialysis was completed. TEM and DLS analysis revealed an average diameter of 37 nm of the nanoparticle product.

To prepare nanoparticle-antibody conjugates, 500 uL of the citrate-stabilized nanoparticle solution was added dropwise into a 1.00 mL of diluted detector antibody (DAB) solution, which was prepared from dilution of 100 uL of rehydrolyzed DAB solution at 1.0 mg/mL with 900 uL of 0.01 M phosphate buffer saline (NaCl 0.138 M; KCl 0.0027 M, pH 7.4). After gentle shaking, the mixture solution was incubated at 37 ^{o}C for 30 min and then centrifuged for 10 min at 6000 rpm for 3 times (washing buffer: 1% BSA in 0.01M PBS at pH=7.4 after centrifugation 15 min at 8000 rpm).

The concentration of GNP and GNP-DAB conjugates was calculated according to the elemental gold content as determined by GFAAS. The average weight of each individual gold nanoparticle was first estimated from the following equation by assuming GNPs are in spherical shape and *fcc* crystal structure:

$$m = \rho \times V = \rho \times (\frac{4}{3}\pi R^3) = \rho \times (\frac{4}{3}\pi(\frac{D}{2})^3) = \frac{\pi}{6}\rho D^3 \qquad (7\text{-}1)$$

where m is the average weight of one gold nanoparticle, ρ is the density of GNPs (19.3 g/cm^3 for *fcc* structure), V is the average volume of GNPs, R is the average radius of nanoparticles, and D is the average diameter of nanoparticles. The average diameter of GNPs was calculated from the average of 200 GNPs on HRTEM micrographs using the ImageJ software (NIH). The average weight of one gold nanoparticle is thus calculated to be 5.12×10^{-7} ng for GNPs with average diameter of 37 nm. Then, the gold nanoparticle solution was diluted to an appropriate concentration (10-100 ppb) by 2% of nitric acid solution (70%, redistilled, 99.999+%) and the gold content in 20 μL of sample solution was analyzed by GFAAS. Each sample was repeated for three times and the average was

taken to calculate the gold content (in the unit of ppb) in diluted sample solution. The gold content in initial solution was calculated by multiplying the gold content in the diluted solution with the dilution factor. The concentration of GNPs in initial solution was then calculated by:

$$c = \frac{m'}{m \times N_A} \tag{7-2}$$

where c is the concentration of GNPs (mol/mL), m' is the gold content in the purified gold nanoparticle solution as determined by GFAAS (in the unit of ppb or ng/mL), m is 5.12×10^{-7} ng for 37 nm GNPs and N_A is 6.023×10^{23}.The concentration of GNP-dAb was determined in the same way as pure GNPs.

7.2.4 Gold nanorods (GNR) synthesis, purification and conjugation to antibodies

GNRs with a longitudinal length of 40 nm and an aspect ratio 4:1 were synthesized according to a literature report (3) and purified by the similar way as used for GNPs. Gold nanorod to capture antibody conjugate (GNR-CAB) solution was prepared by adding 200 uL of the as-prepared GNR solution dropwise to 1.00 mL of 0.1 mg/mL capture antibody solution (cAb) in 0.01 M phosphate buffer saline (NaCl 0.138 M; KCl 0.0027 M, pH 7.4) with gentle shaking. The GNR-cAb conjugates were purified by centrifugation 3 times at 6000 rpm for 10 min (washing buffer: 1% BSA in 0.01M PBS at pH=7.4 after centrifugation 15 min at 8000 rpm). The concentration of the GNR and GNR- CAB conjugates were determined using the similar method as used for GNP-DAB conjugates and described above, but the average volume of gold nanorods was calculated differently from GNPs:

$$V' = \pi R^2 \times (L - 2R) + 2 \times (\frac{1}{2} \times \frac{4}{3} \pi R^3)) \tag{7-3}$$

where *V'* is the average volume of one gold nanorod, *R* is the average transverse radius of the nanorods (10 nm), and *L* is the average longitude length of nanorods (40 nm). The average weight of one gold nanorod was calculated using equation (1) and (3). The concentrations of GNRs and GNR-CAB were determined in the same way as used for GNPs and GNP-DAB (2).

7.2.5 Immunoassay of free-PSA using GNP-DAB and GNR-CAB conjugates

A volume of 20 μL of 0.10 nM GNP-DAB conjugate solution and 20 μL of 0.25 nM GNR-CAB conjugates were added into a 1.5 mL sterilized polypropylene tube and mixed well. To each mixed nanoprobe solution, 20 μL solution of free-PSA antigen standard at different concentrations was added, mixed well and incubated for 30 min at 37 ^{o}C. Five free-PSA sample solutions at the following concentrations were tested: 0, 0.1, 0.5, 1.0, 10.0 ng/mL and an unknown concentration (0.5 ng/mL, prepared by a different researcher). All standards were prepared from diluting the thawed 10 ng/mL standards with sample dilutant solution provided in the ELISA kit. Each concentration was repeated three times. After incubation, sample solutions were analyzed by DLS. DLS samples were prepared by diluting 10 uL of the assay solution into 1.5 mL of nanopure water in a plastic curvette (c=0.5 cm). After standing for 2 min, the sample solution was analyzed twice by DLS. The numeric ratio of nanoparticle oligomers versus individual particles at each concentration was calculated according to size distribution curve. Each data was an average of total 6 data points (from two DLS measurements of three samples).

7.2.6 DLS data processing and calculation of numeric ratios of nanoprobe oligomers to individual nanoprobes

DLS measurements recorded the hydrodynamic diameters, size distributions, and relative scattering intensity percentages of particles in the analyzed sample solution. DLS data file for each sample was exported to ASCII file. The numeric ratios of nanoprobe oligomers versus individual nanoprobes were calculated by EXCEL software (Microsoft, Redmond, WA) or Origin (OriginLab Corp., Northampton, MA) from the exported ASCII file as following: (a) Particles were first classified into two groups according to their hydrodynamic diameter: individual nanoprobes (20-60 nm) and nanoprobe oligomers (60-500 nm). (b) For each group, the sum of multiples of 3rd order of each recorded hydrodynamic diameter and its corresponding relative light scattering intensity was calculated. (c) The numeric ratios of nanoprobe oligomers to individual nanoprobes were obtained by dividing the sum of multiples from the nanoprobe oligomer group by the sum of multiples from the individual nanoprobe group:

$$R = \frac{\sum_{m} I_m \times D_m^{\,3}}{\sum_{n} I_n \times D_n^{\,3}} \qquad (7\text{-}4)$$

where R is the numeric ratio of nanoprobe oligomers to individual nanoprobes, I_m is the intensity percentage of nanoprobe oligomers at each corresponding hydrodynamic diameter D_m, and I_n is the intensity percentage of individual nanoprobes at each corresponding hydrodynamic diameter D_m.

7.2.7 Comparative immunoassay of CA125 using GNP-DAB and GNR-CAB conjugates

The procedure of comparative assay of CA125 was the same as that of free-PSA immunoassay. 20 μL of 0.10 nM GNP-DAB conjugate solution and 20 μL of 0.25 nM GNR-CAB conjugates were added into a 1.5 mL sterilized polypropylene tube and mixed well. Four CA-125 antigen standards, 0 UmL, 15 U/mL, 100 U/mL and 400 U/mL, were reconstituted by nanopure water according to the provided procedure. To each mixed nanoprobe solution, 20 μL of CA125 antigen standard solution with different concentrations was added, mixed well and incubated for 30 min at 37 ^{o}C. Each concentration was repeated for three times. After incubation, DLS samples were prepared by diluting 10 uL of the assay solution into 1.5 mL of nanopure water in a plastic curvette (c=0.5 cm). After standing for 2 min, the sample solution was analyzed twice by DLS. The numeric ratio at each concentration was calculated as the average of the 3 repeating samples (each sample was analyzed twice by DLS) using the same protocol as described above.

7.2.8 Conjugation of 5 nm GNPs onto nanoprobe oligomers

10 μL goat anti-mouse IgG (H+L) (AH) 5 nm gold conjugates were added into 20 μL nanoprobe oligomers solution and incubated for 1 h at 37^{o}C. Nanoprobe oligomers solutions were prepared at four f-PSA antigen concentrations: 0.1 ng/mL, 0.5 ng/mL, 1 ng/mL and 2 ng/mL. Solutions after incubation were centrifuged 3 times at 6000rpm for 10 min, washed by the washing buffer (1% BSA in 0.01M PBS at pH=7.4) and recovered back to 0.01M PBS buffer. Solution was further diluted and ~5 μL of diluted solution were casted on a poly-L-lysine (0.0381 g/mL in 1:3 H_2O:MeOH mixture solvent) treated

400 mesh carbon/formvar coated copper grid. After vacuum drying for 30 min and standing in ambient conditions for at least 12 hours, the sample was analyzed under HRTEM.

7.3 Results and Discussions

7.3.1 Sensitivity of GNPs by DLS measurements

To demonstrate the feasibility and sensitivity of DLS for immunoassay using gold nanoparticle probes, we first conducted a DLS analysis of nanoparticle materials used in this study. Two types of GNPs, a citrate-stabilized gold nanoparticle (GNP) and a cetyltrimethyl ammonium bromide (CTAB)-protected gold nanorod (GNR), were synthesized following the literature procedures.[8] The GNPs have an average core diameter of 37 nm, and the nanorods have a dimension of 10 by 40 nm, as determined from TEM analysis (Figure 7-1*a* and *b*). The actual concentrations of the as-synthesized GNPs and nanorods were determined by a graphite furnace atomic absorption spectroscopy, combined with UV-Vis absorption spectroscopy. The nanoparticle and nanorod solutions were then diluted to appropriate concentrations for DLS analysis. Figure 7-1*c* is the plots of the average scattered light intensity versus nanoparticle and nanorod concentration as measured by DLS. Both GNPs and nanorods demonstrate a linear increase of scattered light intensity versus concentration in the picomolar range. A detection limit of 0.02 pM (low fM range) for GNPs and 0.4 pM for gold nanorods was established, which is similar to the reported result of gold nanoshell.[6a] These detection limits are nine magnitudes lower than protein or DNA molecules and four magnitude lower than sensors based on light absorption.[9] By attaching a metal nanoparticle probe to

biomacromolecules such as antibody, it is possible to develop a highly sensitive immunoassay using the DLS technique.

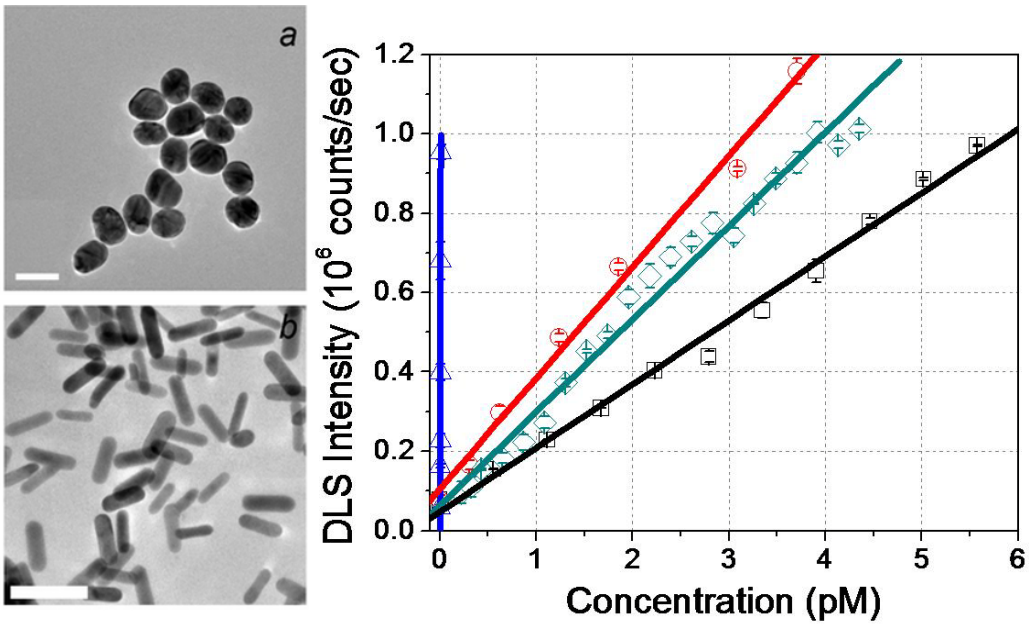

Figure 7- 1. TEM micrographs of (a) GNPs (scale bar: 50 nm), (b) gold nanorods (scale bar: 60 nm), and (c) DLS intensity responses and detection limits for different nanoparticles (-□-: 40 nm×10 nm gold nanorods, LLOQ=0.4 pM, y=0.04717+0.16099x, R^2=0.99559; -○-: 37 nm GNPs, LLOQ=0.02 pM, y=0.10525+0.28012x, R^2=0.99564; -◊-: 40 nm silver nanoparticles, LLOQ=0.21 pM, y=0.06337+0.23509x, R^2=0.99061; -Δ-: 98 nm GNPs, LLOQ=0.7 fM, y=0.02758+119.47x, R^2=0.99212). (Linear fitting, 3σ, R=5 for all groups) (Copyright ® 2008 American Chemical Society)

7.3.2 Conjugation of antibodies to GNP probes

For the immunoassay development, the citrate-protected spherical nanoparticles were conjugated with a detector antibody (GNP-DAB), while the CTAB-protected gold nanorods were conjugated with the capture antibody (GNR-CAB).[10] Through our study, it was found that because of the surface positive charge of the CTAB-stabilized gold nanorods, the capture antibody can be conjugated more effectively to nanorods than the citrate-stabilized nanoparticles, while the detector antibody can be conjugated more

effectively to the negatively charged citrate-stabilized GNPs. The successful conjugation of nanoparticles with detector antibody and nanorods with capture antibody was first confirmed by DLS measurement and UV-Vis spectral analysis (Figure 7-2 and Figure 7-3). After conjugation with the primary antibodies, the average diameter of GNPs increased from 37 to 57 nm, while the hydrodynamic dimension of nanorods increased from 30 to 37 nm. The UV-Vis spectra revealed a slight shift of the surface plasmon resonance in both intensity and wavelength. For GNPs, the SPR band shifted from 535 nm to 541 nm upon antibody conjugation. This shift is most likely caused by the surface chemistry change of the nanoparticles from a citrate-ligand layer to an antibody layer. For the gold nanorods, changes in the SPR band peak wavelengths as well as relative ratio of the two SPR bands were observed. The longitudinal SPR band at 733 nm blue shifted to 725 nm and the transverse SPR band at 516 nm red shifted to 518 nm. The relative intensity of the longitudinal versus the transverse band decreased from 2.7 to 1.6, corresponding to what has been observed previously from a gold nanorod bioconjugate reported by Rayavarpu et al.[11]

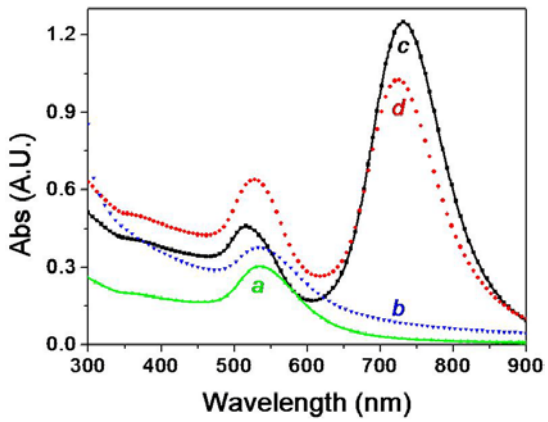

Figure 7- 2. UV-Vis spectra of GNPs and gold nanorods and their conjugates with primary antibodies: (*a*) citrate-protected GNPs (GNP); (*b*) f-PSA detector antibody conjugated GNPs (GNP-DAB); (*c*) CTAB-protected gold nanorods (GNR); and (*d*) f-PSA capture antibody conjugated gold nanorods (GNR-CAB) (Copyright ® 2008 American Chemical Society)

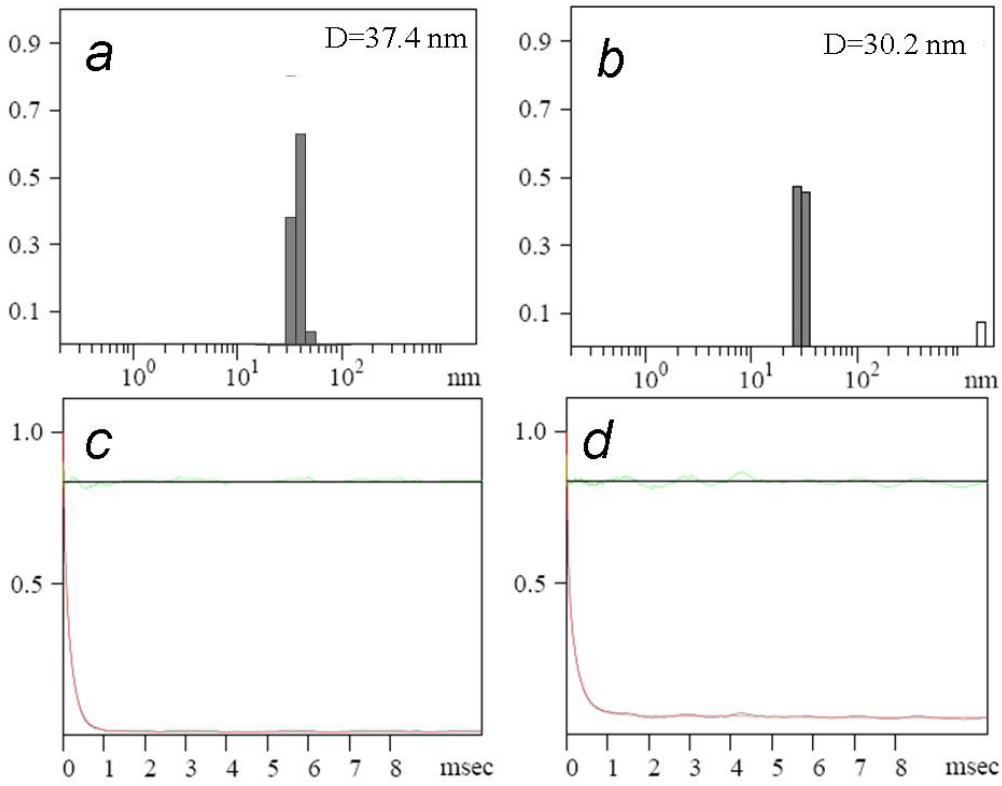

Figure 7- 3. Sizes and size distributions of nanoprobes measured by DLS: (a) 5 pM citrate-protected GNPs (GNP), (b) 5 pM gold nanorods (GNR), and their corresponding correlation functions for (c) GNPs and (d) gold nanorods. (Copyright ® 2008 American Chemical Society)

To further confirm the successful conjugation of the two antibodies to the nanoparticles and nanorods, we analyzed the coupling product of the nanoparticle probes with antigen f-PSA in solution using TEM. A 1:2.5 mixture solution of the two nanoprobes, GNP-DAB:GNR-CAB, was added to a buffer solution of f-PSA with a concentration of 2 ng/mL. The mixed solution was incubated for 30 min at 37 ^{o}C, and then drop cast on a copper grid and examined by TEM. During the imaging, we observed a large amount of nanoparticle-nanorod dimers as shown in Figure 7-4*a*. These nanoparticle dimer and oligomers are believed to be formed through antigen binding with capture antibodies from the nanorods and detector antibodies from the spherical

nanoparticles. With increased f-PSA concentration, the amount of such nanoparticle-nanorod pairs and aggregates increased accordingly. To further verify that the nanoparticle-nanorod pairs and oligomers were formed from the binding between antigen f-PSA and the primary antibodies attached to nanoprobes, we added a secondary anti-mouse IgG-labeled gold nanoparticle (5 nm) into the mixed nanoparticle, nanorods and f-PSA solution. After incubation for 60 min, the solution was cast on a copper grid and examined by TEM. The TEM micrographs as shown in Figure 7-4*d* revealed that most 5 nm GNPs appeared on the surface or vicinity of large nanoparticles and nanorods, due to the binding of secondary antibody from the 5 nm nanoparticles to the primary antibodies on the surface of large nanoparticles and nanorods.

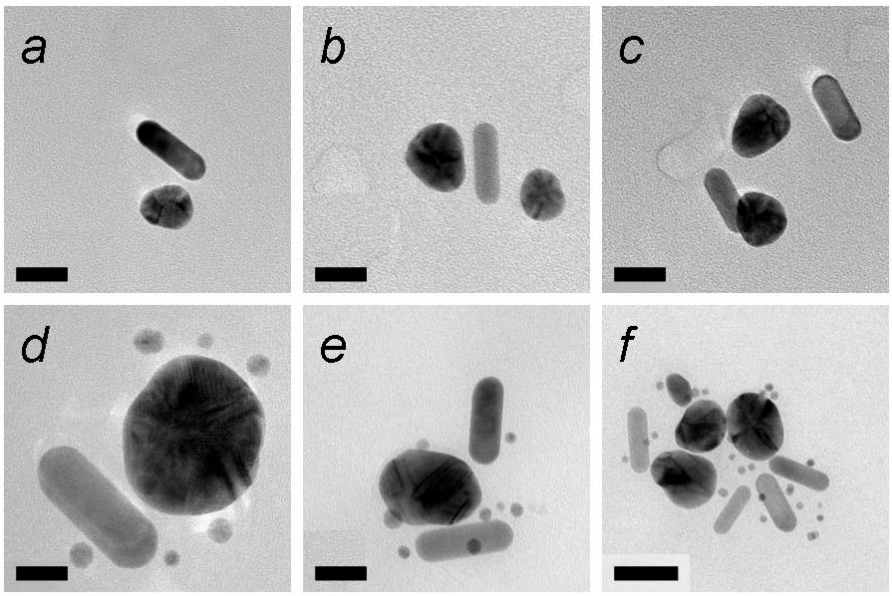

Figure 7- 4. TEM micrographs of: (*a-c*) nanoparticle oligomers formed from a mixture of primary antibodies conjugated GNPs and gold nanorods with the addition of f-PSA antigens (2 ng/mL) in the mixed nanoprobe solution; and (*d-f*) same nanoparticle oligomers, but with additional conjugations of 2nd antibody-coated 5 nm GNPs to the oligomers (Scale bar: 20 nm, except for *d*, which is 10 nm). (Copyright ® 2008 American Chemical Society)

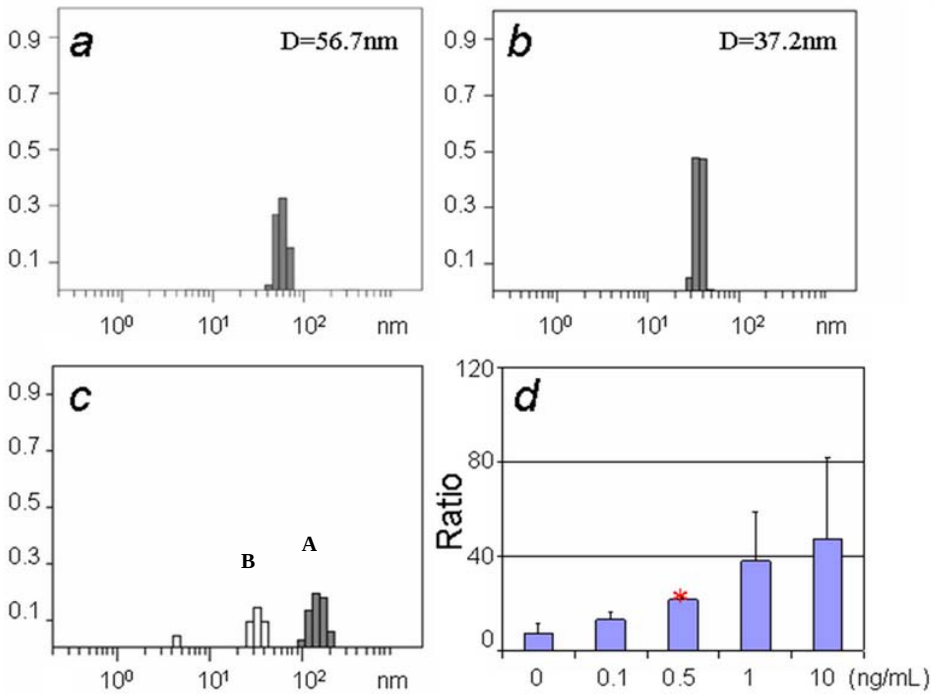

Figure 7- 5. Hydrodynamic diameter distribution plots as determined by DLS measurements: (a) nanoparticle-detector antibody conjugates (GNP-DAB, 5 pM); (b) nanorod-capture antibody conjugates (GNR-CAB, 5 pM); (c) a 1:2.5 mixture of GNP-DAB:GNR-CAB in the presence of f-PSA (1.0 ng/mL); and (d) the calculated numerical ratio of nanoparticle oligomers in the size range of 60-500 nm (peak area A) versus individual particles in the size range of 20-60 nm (peak area B) according to DLS measurement at different f-PSA level (the unknown sample has a concentration of 0.5 ng/ml, data labeled with an asterisk). (Copyright ® 2008 American Chemical Society)

7.3.3 Immunoassay for f-PSA using antibody coated GNP probes

The homogeneous immunoassay of f-PSA was then conducted in solution using the conjugated nanoparticles and nanorods coupled with dynamic light scattering measurement. The two nanoprobes were mixed in 1:2.5 (GNP-DAB:GNR-CAB) ratio and then added to the standard f-PSA solutions with different concentrations. After incubating for 30 min, the solutions were diluted to appropriate concentrations for DLS analysis. Figure 7-5 *a* and *b* are the size distribution of pure conjugated nanoparticles and nanorods, respectively, while Figure 7-5 *c* is the size distribution of mixed nanoprobe solution in the presence of 1 ng/mL of f-PSA. For the pure nanoparticle and nanorod

conjugates, only one size of particles was observed from the distribution. With f-PSA added to the nanoprobe solution, DLS measurement detected two particle sizes (peak area A and B), one is centered at below 60 nm representing individual nanoparticles and nanorods, and one above 100 nm corresponding to nanoparticle-nanorod oligomers. The relative ratio of nanoparticle oligomers in the size range of 60-500 nm versus individual nanoparticles in the size range of 20-60 nm range can be numerically calculated from the size distribution curve. Figure 7-5 *d* is the plot of this numerical ratio versus f-PSA concentration. With increased concentration of f-PSA, the relative percentage of nanoparticle oligomers increased while the percentage of individual nanoprobes decreased. Using the same nanoprobes in buffer solution, we conducted the analysis of an unknown sample solution (f-PSA concentration at 0.5 ng/mL). The determined concentration corresponds very well to the true concentration of the sample (Figure 7-5 *d*, data indicated with an asterisk). It is very important to mention here that the standard f-PSA solutions, including the control solution, were actually prepared in a protein matrix solution to simulate the protein content of human serum samples. It was noticeable that when the two nanoprobes were added to the control solution with 0 ng/mL f-PSA, a certain level of nanoparticle oligomer formation was observed, according to DLS analysis. The aggregation is most likely caused by the high content of proteins and high ionic strength of the matrix solution. However, our study demonstrated that even with a small level of nanoparticle instability and aggregation, a quantitative immunoassay is still possible in complex biological fluids using our developed approach. Recently, it was reported by Liu C.-H. et al.[2e] that the light scattering by metal nanoparticles can be detected directly by a fluorescence spectrometer and further used for quantitative DNA

detection. In this study, we obtained the average scattered light intensity of each assay solution from DLS measurement; however, we did not find a clear correlation between the average scattered light intensity versus antigen concentration in solution. The comparative ratio of nanoparticle oligomers versus individual particles as determined by DLS measurement appears to provide a more accurate bioassay.

We also conducted a control experiment to demonstrate the selectivity of the assay. The mixed nanoprobe solution was added to solutions that contain a different cancer biomarker, CA125. The oligomer versus individual nanoparticle ratio remained unchanged at different concentrations of CA125 (Figure 7-6). This comparison study revealed a good selectivity of the nanoprobe immunoassay.

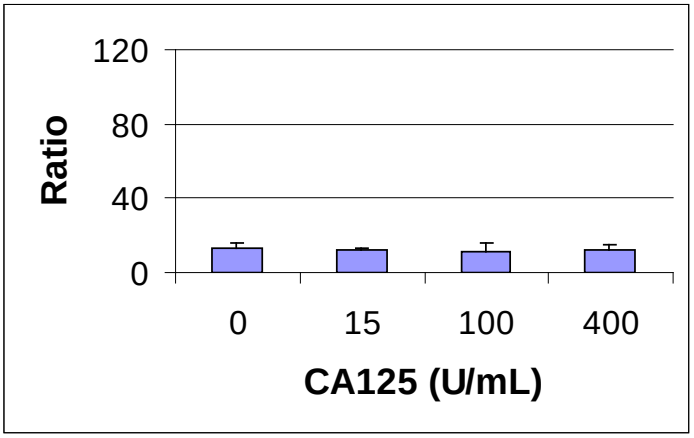

Figure 7- 6. A comparative immunoassay of biomarker CA125 using GNP-DAB and GNR-CAB (the DAB and CAB are anti f-PSA primary antibodies): the calculated numerical ratio of nanoprobe oligomers in the size range of 60-500 nm versus individual nanoprobes in the size range of 20-60 nm according to DLS measurements. Three sample solutions were prepared for each antigen concentration, and each sample solution was measurement twice by DLS. Each data presented here is the average of six data points. (Copyright ® 2008 American Chemical Society)

7.4 Conclusion

In summary, we demonstrated here a promising one-step homogeneous immunoassay. By taking advantage of the large scattering cross section of GNPs and the high sensitivity of DLS measurement, biomarker proteins or other biotargets can be detected at very low concentration using gold nanoparticle probes. As opposed to the traditional plate-based immunoassay, our assay is conducted in solution, which allows a much better mixing and antibody-antigen interaction. The assay does not involve any washing cycle and the assay result can be read as soon as the nanoprobe-sample incubation is completed. Moreover, extremely small amount of samples are needed for the assay. With further improvement on the stability of nanoparticle bioconjugates and the light scattering intensity of nanoparticle probes, the accuracy and detection limit of the assay can be further improved. The research on cancer biomarker detection directly from human serum samples using the method reported here is currently underway.

References:

1 (a) Yu, F.; Persson, B.; Lofas, S.; Knoll, W. Anal. Chem. 2004, 76, 6765-6770. (b) Healy, D.A.; Hayes, C.J.; Leonard, P.; McKenna, L.; O'Kennedy, R. TRENDS in Biotech. 2007, 25, 125-131. (c) Das, J.; Aziz, M.A.; Yang, H. J. Am. Chem. Soc. 2006, 128, 16022-16023.

2 (a) Warnick, G.R.; Nauck, M.; Rifai, N. Clin. Chem. 2001, 47, 1579-1596. (b) Weigum, S.E.; Floriano, P.N.; Christodoulides, N.; McDevitt, J.T. Lab on a Chip 2007, 7, 995-1003. (c) Kokko, T.; Kokko, L.; Soukka, T.; Lovgren, T. Anal. Chim. Acta 2007, 585, 120-125. (d) Xu, X.; Georganopoulou, D.G.; Hill, H.D.; Mirkin, C.A. Anal. Chem. 2007, 79, 6650-6654. (e) Du, B.-A.; Li, Z.-P.; Liu C-H. Angew. Chem. Int. Ed. 2006, 45, 8022-8025.

3 (a) Nikoobakht, B.; El-Sayed, M. Chem. Mater. 2003, 15, 1957-1962. (b) Link, S.; El-Sayed, M.A. J. Phys. Chem. B. 1999, 103, 8410-8426. (c) Sun, Y.; Xia, Y. Science 2002, 298, 2176-2179.

4 (a) Katz, E.; Willner, I. Angew. Chem. Int. Ed. 2004, 43, 6042-6108. (b) El-sayed, I.H.; Huang, X.; El-Sayed, M.A. Nano Lett. 2005, 5, 829-834. (c) Huang, X.; El-sayed. I.H.; Qian, W.; and El-sayed M.A. J. Am. Chem. Soc. 2006, 128, 2115-2120.

5 Berne, B.J.; Pecora, R. Dynamic ligh scattering: with applications to chemistry, biology, and physics; Wiley: New York, 1976.

6 (a) Xie, H.; Gill-Sharp, K.L; O'Neal, D.P. Nanomedicine: Nanotechnology, Biology, and Medicine 2007, 3, 89-94. (b) Ipe, B.I.; Shukla, A.; Lu, H.; Zou, B.; Rehage, H.; Niemeyer, C.M. ChemPhysChem 2006, 7, 1112-1118.

7 Sahab, Z.J.; Semaan, S.M.; Sang Q.-X.A. Biomarker Insights 2007, 2, 21-43.

8 (a) Frens, G. Nat. Phys. Sci. 1971, 241, 20-22. (b) Nikoobakht, B.; El-Sayed, M.A. Chem. Mater. 2003, 15, 1957-1962.

9 (a) Pecora, R. J. of Nanoparticle Research 2000, 2, 123-131. (b) Sorlie, S.S.; Pecora, R. Macromolecules 1998, 21, 1437-1449. (c) Hirsch, L.R.; Jackson, J.B.; Lee. A.; Halas, N.J.; West, J.L. Anal. Chem. 2003, 75, 2377-2381.

10 (a) Roe, C.D.; Courtoy, P.J.; Baudhuin, P. J. of Hisochem. and Cytochem. 1987, 35, 1191-1198. (b) Brewer, S.H.; Glomm, W.R.; Johnson, M.C.; Knag, M.K.; Franzen, S. Langmuir 2005, 21, 9303-9307. (c) Ackerson, C.J.; Jadzinsky, P.D.; Jensen, G.J.; Kornberg, R.D. J. Am. Chem. Soc. 2006, 128, 2635-2640.

11 Rayavarpu, R.G.; Petersen, W.; Ungureanu, C.; Post, J.N.; Leeuwen, T.G.; Manohar, S. Int. J. of Biomedical Imaging 2007, 29817.

CHAPTER 8. SURFACE MODIFICATION OF GOLD NANOPARTICLES BY POLY(ETHYLENE GLYCOL) POLYMERS AND APPLICATIONS IN BIOMOLECULAR DETECTION

8.1 Introduction

GNPs are a class of plasmonic materials under intense research and development for broad biological applications, especially in ultrasensitive biomolecular detection.[1] Since 1990s, investigations on controlled synthesis and functionalization of GNPs have grown exponentially.[2] GNPs can be synthesized with strictly controlled geometries and sizes, ranging from a few to several hundreds of nanometers in both aqueous solution as well as in organic solvents.[3] GNPs after synthesis are normally protected by a shell of stabilizing molecules, through either physical adsorptions or chemical interactions to GNP surface. For example, GNPs prepared by the well-known citrate reduction method are protected with physically adsorbed citrate ions.[4] These surface molecules are crucial to keep GNPs dispersed in solution. The success in synthetic preparation and stabilization by surface ligands provides essential colloidal GNP probes for applications.

To apply GNPs for biological applications, GNPs need to be conjugated with biomolecules. A type of commonly used methods to conjugate biomolecules with GNPs is through physical adsorption. For example, proteins, with charges on their surface, can be adsorbed onto GNP surface through electrostatic interactions.[5] This method is widely used due to the easy procedure. Commercially available antibody-conjugated GNP probes (referred as “immunogold”) are prepared through physical adsorption methods and have been applied for cell imaging and flow cytometry applications.[6] Substantial studies using GNP probes prepared by physical adsorption methods were reported for the

detection of proteins, DNA, aptamers, etc.[7] In Chapter 6 and Chapter 7, we have used the physical adsorption method in the preparation of antibody-conjugated spherical 40 nm GNPs and 40 nm by 10 nm gold nanorods and applied these GNP probes in sensitive detection of mouse IgG and PSA antigens.

While physical adsorption methods possess the advantage of procedure simplicity, there are several limitations existing for these methods. Protein-GNP conjugates prepared by these adsorption methods rely on the equilibrium between GNP-conjugated antibodies and free antibodies in the solution. These GNP probes have low protein repellency and are susceptible to dissociation of original proteins from the GNP surface. This can result to diminished labeling efficiency. GNP probes tend to aggregate out from the solution due to non-specific interactions of proteins or dissociation of proteins.[8] Moreover, because these conjugates are based on non-specific electrostatic interactions, they are not resistant to high ionic strength or extreme pH conditions in solution thus lack the long term stability. Such prepared GNP probes are then not very stable in buffer solutions or biological fluids. As a consequence, these limitations on stability and biomolecular conjugation for physically adsorbed GNP probes will inevitably cause serious problems in biomolecular assays.

To improve the stability and bio-specific functionality of biomolecules-conjugated GNP probes, surface modification on GNPs is necessary.[9] Surface modifications generally result to a dense layer of molecules on the GNP surface with higher binding affinity between the GNP surface and surface ligands. In one approach, original stabilizing molecules on GNPs can be place exchanged by polymers.[10] For example, thiolated polymers can be anchored onto GNPs, by replacing original citrate

molecules on GNPs due to the strong binding affinity between gold surface and thiol groups. Polymers can thus form a protecting layer on GNP surface and contribute to improve colloidal stability of GNPs probes.[10]

In addition to surface modification of GNP surface, covalently conjugate proteins to GNPs can help in preparing stable and biospecific GNP probes with resistance to nonspecific interactions or aggregations.[9] In a comparison to nonspecific interactions in physiadsorption methods, covalent bondings between GNPs and biomolecules are much less susceptive to solution condition variations, such as other proteins, solution ionic strength or pH values. These covalently conjugated GNP probes can maintain high stability as well as bio-specificity. Surface biomolecules are not in equilibrium with free biomolecules in solution. GNP probes prepared through such a covalent coupling methods have been demonstrated to be more stable and robust in biological applications.[10b]

The combination of surface modifications and covalent coupling of biomolecules to GNPs has been proven to be effective in using robust GNP probes for biological applications. However, yet there is no systematic and quantitative study on the effects of surface modification to the stability of GNPs with respects to GNP sizes and solution conditions. Motivated by this, in this study we prepared polymer modified GNPs and investigated their stabilities at different GNP core sizes and solution conditions. Through this study, we aimed to reveal the effects of different solution conditions to the stability of GNP probes and to provide pratical guides in the preparation of robust GNP probes. Thiolated bi-functional poly(ethylene glycol) (PEG) polymers were chosen as polymeric supports due to their proven effectiveness to render nonspecific interactions between

biomolecules and to improve bio-compatibility and stability of GNPs in biological environment.[10b] The stability of all tested PEG-GNPs showed substantial increases over unmodified citrate-stabilized GNPs.

To further investigate the performance of these PEG-GNP probes and to apply them in biological detection applications, we conjugated these PEG-GNPs with antibodies through covalent coupling reactions and applied them in the detection of f-PSA antigens. The covalent conjugation of antibodies to PEG-GNP was verified in a simple and effective aggregation assay. We then applied the 100 nm PEG-GNPs as immunoassay probes for the detection of f-PSA antigens, with a one-step immunoassay format similar to these demonstrated in Chapter 6 and Chapter 7. Sensitivity and reproducibility of the immunoassay using PEG-GNPs were improved significantly.

8.2 Experimental

8.2.1 Chemicals, materials and instruments

Citrate-protected GNPs ($_{Ci}$GNPs) in a range of core sizes and 40 nm goat anti-mouse IgG conjugated GNPs (GNP-anti-IgG) were purchased from Ted-Pella. Thiolated and carboxylated poly(ethylene glycol) polymer (COOH-PEG-SH) (M.W.=3000) were obtained from RAPP Polymere. The ELISA kit and antibodies for PSA or f-PSA were from Anogen Inc. All other materials were from Aldrich.

8.2.2 Preparation and purification of poly(ethylene glycol) coated GNPs

Poly(ethylene glycol) polymer coated GNPs (PEG-GNPs) were prepared by adding 1.5 mL COOH-PEG-SH solution (0.6 mg/mL) into 10 mL intact $_{Ci}$GNPs solution and keeping in gentle shaking for one week.

In stability tests, the as-prepared PEG-GNPs were purified by centrifugation and washed by DI water for three times. Different centrifugation conditions were used for PEG-GNPs at different sizes (20 and 40 nm: 13.4k rpm for 6 min; 60 and 80 nm: 13k rpm for 3 min; 100, 150, 200, and 250 nm: 8k rpm for 2 min).

In biomolecular conjugation and immunoassays, the crude 40 nm or 100 nm PEG-GNPs were purified by column chromatography instead of centrifugation. A volume of 400 μL PEG-GNP solution was passed through a Sepharose CL-2B column, with a gel height of ~10 cm and PBS buffer (PBS 10 mM; NaCl 0.138 M; KCl 0.0027 M, pH 7.4) as the mobile phase. The collected PEG-GNPs were filtered by a membrane (hole size: 200 nm) to exclude large aggregates. UV-Vis and DLS were used in the purification and antibody conjugation process to monitor the size and stability of PEG-GNPs probes.

8.2.3 Stability tests for PEG-GNPs at various NaCl concentrations

NaCl solutions at concentrations 0, 0.2, 0.3, 0.4, 0.8 M were prepared. The stability test was performed as following: 100 μL centrifugation purified PEG-GNP solution and 100 μL NaCl solution were mixed in a well and the absorbance of each mixed solution at corresponding SPR peak wavelength (according to Table 5-1) was measured, respectively at each GNP size and each NaCl concentration. Each sample was duplicated and the average hydrodynamic diameter was calculated.

8.2.4 Stability tests for PEG-GNPs at various pH values or buffer conditions

The pH values of centrifugation purified PEG-GNP solutions were adjusted from 4 to 10 using 1 M HCl or 1 M NaOH solutions (Table 8-2). For buffer solutions, equal volume of purified PEG-GNP solution and the buffer solution (PBS or Tris buffer) were

mixed. The absorbance of each sample at the corresponding SPR peak wavelength was monitored, respectively.

8.2.5 Biomolecular conjugation and aggregation assay of 40 nm PEG-GNPs

The 40 nm -COOH functionalized PEG-GNPs were conjugated to two PSA antibodies (PSA-CAB and PSA-DAB, respectively), with the use of covalent coupling reagents EDC (Ethyl-3-[3-dimethylaminopropyl]carbodiimide hydrochloride) and sulfo-NHS (N-hydroxysulfosuccinimide). The purified PEG-GNP probe solution 450 μL was added by 5 μL EDC/sulfo-NHS mixture solution (25.7 mM/51 mM) and gently shaked for 30 min, then passed through a Sephadex G-25 column. Solutions were equally divided into two portions, with each portion added by 5 μL of PSA antibody solutions, respectively for PSA-CAB and PSA-DAB. Solutions were gently shaked for 3 hours at RT and purified using a Sepharose 4B column.

The aggregation assay was performed by mixing 100 μL of 40 nm GNP-anti-IgG solution (0.1 nM) with 100 μL PEG-GNP probes (respectively for PEG-GNP-CAB and PEG-GNP-DAB). Mixture solutions were incubated at 37 ^{o}C and the average size of the GNP probes in each mixture solution was monitored by DLS along time. All measurements were performed at a detection angle of 90^{o}.

8.2.6 Immunoassay of for f-PSA detection using 100 nm PEG-GNPs

The purified 100 nm PEG-GNP solution 450 μL was covalently conjugated with two paired anti-f-PSA antibodies, denoted as CAB and DAB respectively. The procedure of conjugation and purification was similar to the one in section 8.2.5. These two PEG-GNP probes were then used in the immunoassay for the detection of f-PSA antigens. The procedure was similar to that in section 7.2.5. The f-PSA antigen solutions with f-PSA

levels lower than 0.1 ng/mL were prepared from serial dilutions of 10 ng/mL f-PSA stock solution. After the anti-f-PSA conjugated PEG-GNP probes and f-PSA antigen solutions were prepared, the one-step immunoassay was performed. At each f-PSA concentration, 30 μL of each of the two PEG-GNP probe solutions were mixed and added by 10 μL of antigen solution to a total volume of 70 μL. Samples were incubated at 37 ^{o}C for 1 hour and read out by DLS at a measurement angle of 13^{o}. The test was triplicated at each f-PSA concentration.

8.3 Results and Discussions

8.3.1 Improved stability of PEG-GNPs

Citrate-protected GNPs are known to form irreversible aggregates upon addition of salts into the solution. The aggregation process results to a decrease in the SPR absorbance intensity and also a broadening of the SPR band.[11] For example, the SPR peak absorbance of 40 nm $_{Ci}$GNPs shows a significant drop within minutes when the NaCl concentration in the $_{Ci}$GNP solution is above 20 mM. Meanwhile, an observable color change for the GNP solution from purplish to blue can be seen. However, covering the surface of GNPs with thiol molecules, polymers or biomolecules could improve the GNP stability significantly. Applications based on this property have been investigated for the detection of metal ions, thiol molecules such as cystein, or biomolecules.[7,12] The monitoring, or the detection, in these early studies relied on visible color changes as a qualitative standard or quantitative measurement with UV-Vis spectrometers. These detection assays showed easiness in material preparation and procedure, but lack the ultra-high sensitivity and detection reproducibility. They also implied that ultrahigh sensitivity is possible with better prepared GNP probes. In this study, we measured the

UV-Vis spectra of surface-modified PEG-GNPs at various GNP sizes and solution to study the stability of these PEG-GNPs.

Table 8- 1. Relative absorbance of 100 nm PEG-GNPs in NaCl solutions

Relative Absorbance (%)	[NaCl] in mixture solution (mM)				
	0	100	150	200	400
20 min	100%	96%	98%	98%	98%
30 min	96%	94%	95%	94%	95%
40 min	98%	93%	94%	95%	96%
60 min	99%	93%	95%	95%	96%
120 min	97%	91%	93%	94%	94%
180 min	95%	91%	92%	92%	92%
19 hours	100%	86%	87%	89%	91%

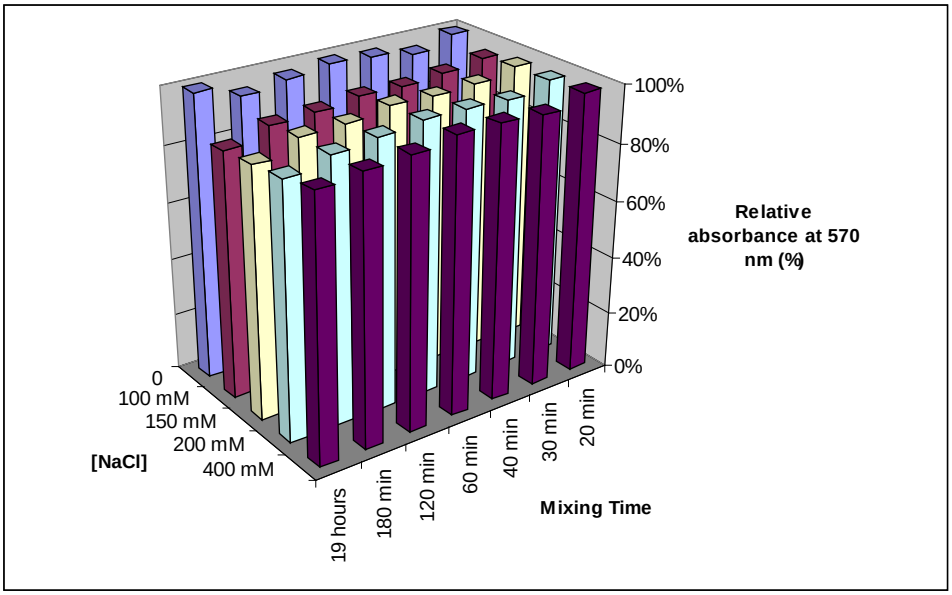

Figure 8- 1. Relative absorbance of 100 nm PEG-GNPs in NaCl solutions along mixing time

8.3.1.1 Stability of 100 nm PEG-GNPs in NaCl solutions

We first tested the stability of 100 nm PEG-GNPs along time in various NaCl solutions. From Table 8-1 and Figure 8-1, we can see that the 100 nm PEG-GNPs pertained >90% of their original absorbances at all four tested NaCl concentrations up to 3 hours. At the time 19 hours, the absorbances decreased more but were still at least 86% to the control. These results were in a sharp comparison to that of bare $_{Ci}$GNPs in NaCl

solutions and revealed out the excellent salt resistance and colloidal stability of 100 nm PEG-GNPs. Furthermore, there were no significant differences in the stability of 100 nm PEG-GNPs at [NaCl] from 100 mM to 400 mM. Considering that biological fluids have NaCl concentrations within the tested range, such robust PEG-GNPs are promising to have excellent colloidal stability in biological fluids.

8.3.1.2 Stability of different size PEG-GNPs in NaCl solutions

The high stability of 100 nm PEG-GNPs in NaCl solutions indicated that surface modification by PEG polymers to $_{Ci}$GNPs is very useful in the preparation for robust GNP probes. Following this, we extended the investigation to differently sized PEG-GNPs. Table 8-2 and Figure 8-2 summarize the relative absorbance of different size PEG-GNPs at their corresponding SPR peak wavelengths when mixed with NaCl solutions. PEG-GNPs with sizes up to 100 nm were shown to be stable at all tested NaCl concentrations. However, for large size PEG-GNPs (core diameter >100 nm), significant decreases in their SPR peak absorbances were observed, indicating that 150, 200 and 250 nm PEG-GNPs did not have as good stability as smaller size PEG-GNPs. These results imply that thiolated PEG polymers with a molecular weight of 3000 can effectively protect GNPs in high NaCl concentration solutions for GNPs with sizes up to 100 nm. The reduced stability for larger size PEG-GNPs is possibly related to the surface coverage percentage and the packing density of PEG polymers on the GNP surface. Because larger size GNPs have larger surface areas which are proportional to the square of the GNP diameter, it would become more difficult for PEG polymers to fully shield the surface of larger size GNPs and to protect them from attacks by salt ions in solution. Due to this, the packing density of PEG polymers on larger PEG-GNP surface and results

to higher susceptibility to salt attacks. These observations and analyses can be helpful in the selections of GNP core size and PEG polymer length during robust PEG-GNP preparations.

Table 8- 2. Relative absorbance of PEG-GNPs at various NaCl concentrations

PEG-GNP size (nm)	Abs wavelength	[NaCl] (mM)				
		0	100	150	200	400
20	525 nm	100%	97%	95%	95%	98%
60	533 nm	100%	96%	98%	97%	95%
40	535 nm	100%	99%	97%	99%	98%
80	549 nm	100%	97%	99%	93%	92%
100	570 nm	100%	97%	94%	95%	91%
150	639 nm	100%	67%	76%	77%	76%
200	572 nm	100%	73%	71%	69%	69%
250	608 nm	100%	80%	80%	84%	83%

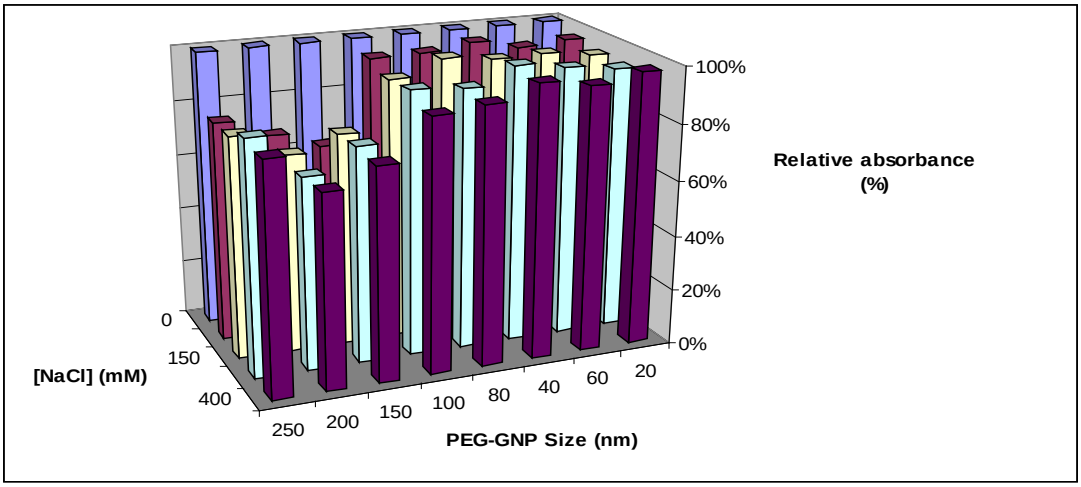

Figure 8- 2. Relative absorbance of PEG-GNPs in solutions at different NaCl concentrations measured by UV-Vis

8.3.1.3 Stability of PEG-GNPs in solutions at different pH values or buffer conditions

After examining the stability of PEG-GNPs in NaCl solutions, we evaluated the stability of PEG-GNPs in solution at different pH or buffer conditions. Table 8-3 and Figure 8-3 show the relative absorbance of PEG-GNPs in pH 4-10 solutions and two buffer solutions. PEG-GNPs solutions at pH=7 were used as controls. From these results,

it can be seen that PEG-GNPs at all tested sizes were stable in solutions with pH values 6-10. However, in pH 4 or 5 solutions, PEG-GNPs were not very stable and showed large decreases in the absorbance. This indicated that these carboxylic group functionalized PEG-GNPs did not prefer acidic conditions. In the pH range 6-10, the stability of PEG-GNPs was found to be related to the GNP size. PEG-GNPs with sizes from 20 to 150 nm are stable in this pH range, but larger size 200 nm and 250 nm PEG-GNPs were not as stable as smaller size PEG-GNPs. These results revealed that PEG polymers used in this study can stabilize GNPs with sizes up to 150 nm in pH 6-10 solutions.

The stability of PEG-GNPs in buffer solutions was exemplified by testing them in two of the most common buffers, PBS and Tris buffers (Table 8-3 and Figure 8-3). Note that the 100 nm PEG-GNP showed the highest stability in these two buffers, while all other size PEG-GNPs had obvious stability decreases in either one or both buffers. Such superior stability of 100 nm PEG-GNPs in all these tested ionic strength, pH and buffer conditions suggests that the 100 nm PEG-GNPs as prepared here are very promising to be used as robust GNP probes in biological applications.

Table 8- 3. Relative absorbance of PEG-GNPs in solutions at different pH or buffer condition after mixed for 4 h

	pH								
Size (nm)	4	5	6	7	8	9	10	PBS	Tris
20	69.2%	84.6%	101.3%	100.0%	101.3%	98.7%	100.0%	76.9%	79.5%
40	60.7%	66.4%	100.9%	100.0%	100.9%	101.9%	100.9%	72.0%	65.4%
60	93.4%	-	105.5%	100.0%	101.6%	100.5%	101.6%	88.5%	94.0%
80	72.9%	83.7%	100.0%	100.0%	99.2%	102.3%	101.6%	89.9%	97.7%
100	67.1%	82.0%	103.0%	100.0%	103.0%	102.4%	100.0%	94.0%	94.0%
150	93.2%	83.1%	89.8%	100.0%	101.7%	101.7%	98.3%	89.8%	89.8%
200	77.5%	70.0%	67.5%	100.0%	92.5%	85.0%	72.5%	55.0%	50.0%
250	94.6%	70.3%	91.9%	100.0%	102.7%	97.3%	83.8%	73.0%	94.6%

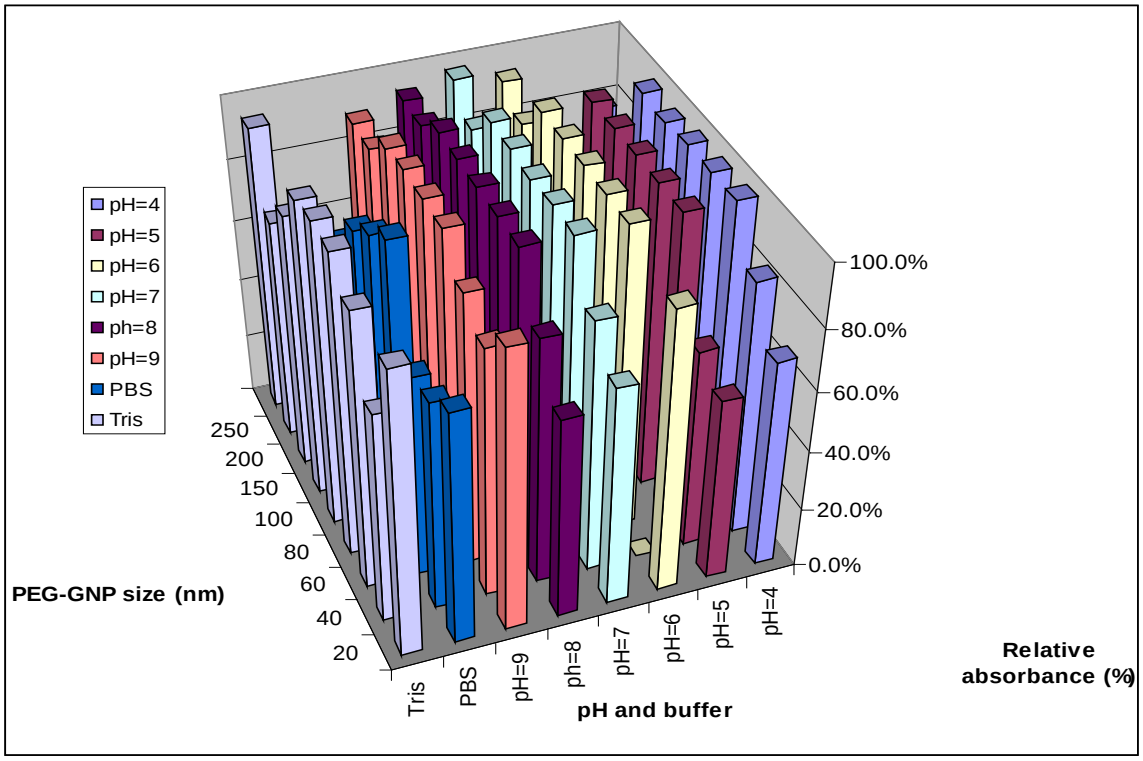

Figure 8- 3. Relative absorbance of PEG-GNPs in solutions at different pH or buffer condition after mixed for 4 h

We interpret the substantial stability improvement of PEG-GNPs due to four main reasons. First, the strong gold-thiol binding can protect the GNP core from outside ion attack. Second, the thiol end group on the PEG polymer can anchor the polymer molecule to the GNP surface firmly.[2,5] Third, PEG polymers on PEG-GNPs can form a steric layer to prevent PEG-GNPs from ion attacks and thus render PEG-GNPs more difficult to aggregate out.[13] Fourth, the backbone of PEG polymers is neutral in charge, which makes PEG-GNPs less sensitive to salt concentrations or pH value changes. Due to the combination of these four effects, the stability of PEG-GNPs showed significant improvements. In addition, these PEG polymers have another advantage in minimizing non-specific interactions for biomolecules. These excellent properties, including robust

colloidal stability and low non-specific bimolecular interactions, motivated us to use PEG-GNPs probes in biological detection applications.

8.3.2 Covalent conjugation of antibodies to PEG-GNPs

Antibodies conjugated PEG-GNPs probes were prepared through a simple covalent conjugation procedure, by an amide reaction between the carboxyl groups on the PEG ligands and the amino groups on antibodies through the EDC/sulfo-NHS protocol. To verify that antibodies can preserve their bioactivity and bio-specificity after covalently conjugated to PEG-GNPs, two GNP aggregation reactions were designed. 40 nm PEG-GNPs were conjugated with a pair of mouse anti-human PSA antibodies, CAB and DAB respectively. The two kinds of PEG-GNP probes were named as PEG-GNP-CAB and PEG-GNP-DAB (Figure 8-4). The size of 40 nm was chosen to match the size of the other GNP probe, whish was the goat anti-mouse IgG antibody conjugated 40 nm GNPs (GNP-anti-IgG) purchased from Ted Pella. Note that these GNP-anti-IgG probes were prepared through physical adsorption methods but not surface modified with PEG polymers.

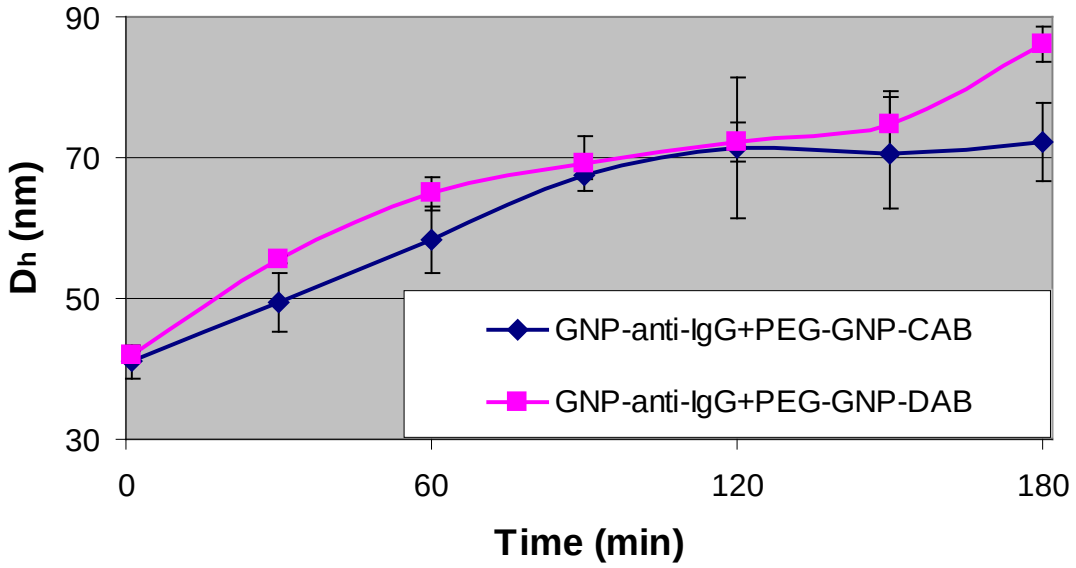

Figure 8- 4. The aggregation assay between 40 nm goat anti-mouse IgG conjugated GNPs (anti-mouse-GNP) and 40 nm mouse anti-human PSA antibody conjugated PEG-GNPs (CAB and DAB are matched pair antibodies for human PSA)

If the covalent conjugation was successful, the PEG-GNP-CAB (or the PEG-GNP-DAB) should form aggregates when mixing with GNP-anti-IgG probes. The aggregation reactions are through the specific bio-recognition reactions between the mouse IgG antibody on the PEG-GNP-CAB surface (or the PEG-GNP-DAB surface) and the goat anti-mouse IgG antibody on the GNP-anti-IgG surface. The aggregation reaction will result to size increases of GNP probes. Such size changes of GNP probes can be sensitively monitored by DLS. The results shown in Figure 8-4 revealed out the kinetic growth of the GNP aggregates in two probe solutions up to 3 h, respectively for PEG-GNP-CAB and PEG-GNP-DAB. The average hydrodynamic diameters of GNP probes increased continuously from the original ~40 nm to ~80 nm during 3 h. We conclude such size increases were due to the oligomer formation of PEG-GNP probes. These oligomers were dimmers, trimers, and higher order aggregates and they grew along time

to larger sizes. Through these results, we confirmed that the bioactivity and specificity of antibodies on PEG-GNPs were preserved. In a closer comparison for PEG-GNP-CAB and PEG-GNP-DAB probes solutions, we can also see that these two kinds of antibody-conjugated GNP probes had similar size increasing rates, while PEG-GNP-DAB showed slightly faster size increasing rate. This indicated that PEG-GNP-DAB had slight higher activity than PEG-GNP-CAB to goat anti-mouse IgG antibodies. These two aggregation reactions may be used in applications of fast antibody activity studies.

8.3.3 Immunoassay application of 100 nm PEG-GNPs for free-PSA (f-PSA) detection

From the above results in 8.3.1 and 8.3.2, we have showed that the improved stability of PEG-GNPs and successful covalent antibody conjugation to PEG-GNPs. We then applied these PEG-GNPs in bimolecular detection applications. We used the 100 nm PEG-GNPs for the detection of f-PSA antigen using a one-step amplification-free and washing-free assay format.

The core size of 100 nm was selected due to a balance between the colloidal stability and sensitivity of the immunoassay. From results in section 8.3.2, the 100 nm PEG-GNPs have the highest stability in NaCl solutions, acidic or basic solutions or buffer solutions. Such excellent colloidal stability is essential in using PEG-GNPs for biological applications. In the other side, DLS detection prefers larger size GNPs. Larger size GNPs can scatter light stronger so have better sensitivity in DLS detection. This is beneficial to improve the sensitivity of GNP-based immunoassays. The three larger size 150, 200 or 250 nm are better for this purpose but they had lower colloidal stability in tested salt and pH conditions so were not used in the immunoassay applications in this study.

Table 8- 4. Immunoassay for f-PSA using 100 nm PEG-GNP probes

f-PSA (ng/mL)	D (nm)	Stdev (nm)
0.000	171.8	8.7
0.001	173.9	18.9
0.010	186.3	21.1
0.100	206.4	37.4
1.000	245.1	34.5
2.000	280.7	60.5
5.000	337.5	26.3
10.000	339.6	156.6

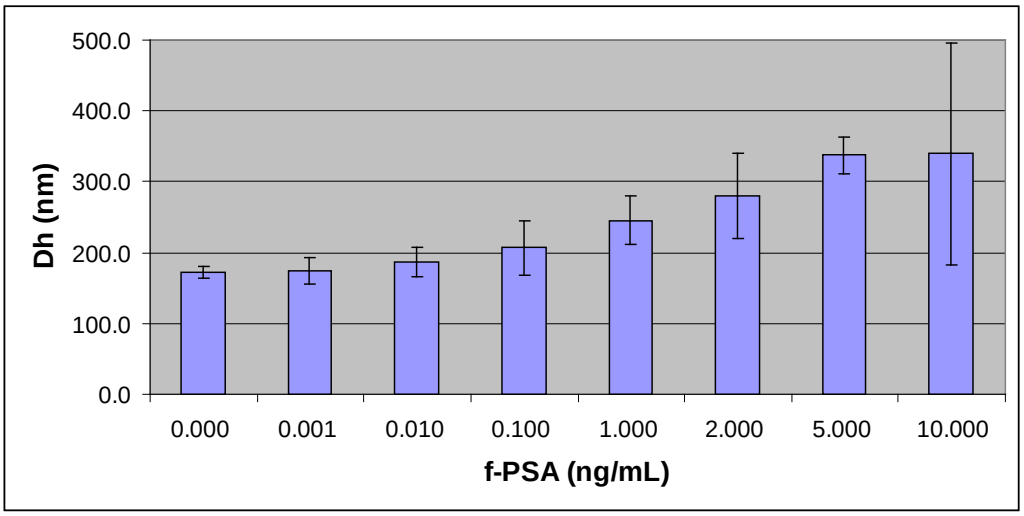

Figure 8- 5. Immunoassay for f-PSA detection using 100 nm PEG-GNP probes (second order exponential decay fitting: y = -168.858*exp(-x/3.00203) + -27.5137*exp(-x/0.01413) + 368.1954; R^2= 0.99933; LLOD: 0.046 ng/mL)

As already discussed in section 7.1, f-PSA is the unbound form of PSA. While the PSA level for normal male is <4 ng/mL, the f-PSA level is typical lower than PSA and in the range of 10% of the PSA level.[14] It is thus more difficult to precisely measure the f-PSA level in biofluids than to measure the PSA level. Due to this, we focused on the challenges to use 100 nm PEG-GNPs for the detection of f-PSA antigens and demonstrate the superior stability, bioactivity and specificity of PEG-GNP probes. The principle of the immunoassay was based on a sandwich type reaction between f-PSA antigens and the two mouse anti-f-PSA antibodies-conjugated PEG-GNP probes, similar

to the reaction as illustrated in Scheme 7-1. Because all PEG-GNPs were multi-covalent, the addition of f-PSA solution into the mixture of the two probe solution can introduce the aggregation of PEG-GNPs. The extent of the aggregation reaction was correlated with the concentration of the f-PSA and the size changes of these PEG-GNPs were shown in Table 8-4 and Figure 8-5.

By increasing the level of f-PSA in the solution from 0 to 10 ng/mL, the average size of the PEG-GNP probes in solution increased from 171 nm to 340 nm. The correlation between the size and the f-PSA level can be best fitted with a second order exponential decay (Figure 8-5, caption). Ultrahigh sensitivity as well as a good dynamic range for f-PSA detection were demonstrated in this simple and fast immunoassay. Using the standard 3σ method, the lower limit of detection (LLOD) of the immunoassay was determined to be 0.046 ng/mL. The immunoassay showed a dynamic range from 0.046 ng/mL to 5 ng/mL. To our best knowledge, such sensitivity has not been reported in an amplification-free and washing-free assay. In fact, such sensitivity and dynamic range are close to those of currently commonly used methods, such as ELISA. For example, the ELISA kit from Anogen for f-PSA measurements has a claimed sensitivity of 0.022 ng/mL and a dynamic range up to 10 ng/mL. However, such sensitivity and dynamic range are achieved with multiple sample washing and signal amplification steps. The new immunoassay in our study showed comparable sensitivity and dynamic range but had much simplified procedure as well as much reduced sample volume (from 50 μL to 10 μL). Thus the new PEG-GNP based immunoassay is very promising for fast and simple detection of f-PSA antigens.

In the current study, we only exemplified the biological detection applications of PEG-GNP probes in f-PSA detection. However, with slightly modified protocols, the immunoassay should fit for the detection of other biomolecules as well. The general and simple biomolecular conjugation protocol for PSA and f-PSA antibodies can be applied easily to other biomolecules. For immunoassays, the simple one-step assay would also dramatically shorten the assay development time because it avoids many issues in traditional heterogeneous immunoassay development, such as substrate selection, enzyme selection and conjugation. Considering that these selection and optimization steps typically will take 4-6 months, the new immunoassay in this work would greatly save the assay development time and cost, while also providing better reliability due to less parameters to be optimized.[15] In addition, the sensitivity of the new immunoassay can fulfill the requirements in bimolecular detection. In fact, the diagnostic ranges of many clinical important protein biomarkers identified yet fall into the pg/mL-ng/mL range. Such sensitivity and dynamic range were demonstrated to be achievable in the new immunoassay. We believe these advantages would make the new immunoassay to be very competitive to traditional assays in biomolecular detection and other biological applications.

8.4 Conclusions

In this contribution, we reported the stability improvements of GNPs after surface modification by thiolated PEG polymer and exemplified biomolecular detection applications of these PEG-GNP probes using f-PSA as an example target analyte. It was found that PEGlylation significantly improved the stability of GNPs in NaCl solutions (with [NaCl] up to 400mM), acidic or basic solutions (pH from 6 to 10) and buffer

solutions. The 100 nm PEG-GNPs were found to have the best stability in all tested conditions. After PEGlylation, we demonstrated that antibodies could be conjugated with PEG-GNPs through a simple covalent coupling reaction. The 100 nm PEG-GNPs conjugated with anti-f-PSA antibodies were then used in a one-step washing-free and amplification-free immunoassay for the detection of f-PSA antigens. The immunoassay showed an ultra sensitivity to as low as 0.046 ng/mL, which is comparable with the sensitivity of commercial products but with a much simplified procedure and reduced sample volume. This new immunoassay shows promises in meeting the highly desired demand for a simple, fast, small sample consumption, and cost-effective in situ immunoassay.

References:

[1] (a) Daniel, M.C.; Astruc, D. Chem. Rev. 2004, 104, 293-346. (b) Hutchings, G.J.; Brust, M.; Schmidbaur, H. Chem. Soc. Rev. 2008, 37, 1759-1765. (c) Anker, J.N.; Hall, W.P.; Lyandres, O.; Shah, N.C.; Zhao, J.; Van Duyne, R.P.; Nat. Mater. 2008, 7, 442-453.

[2] (a) Schmid, G. Chem. Soc. Rev. 2008, 37, 1909-1930. (b) Hostetler, M. J.; Wingate, J. E.; Zhong, C.-J.; Harris, J. E.; Vachet, R. W.; Clark, M. R.; Londono, J. D.; Green, S. J.; Stokes, J. J.; Wignall, G. D.; Glish, G. L.; Porter, M. D.; Evans, N. D.; Murray, R. W. Langmuir 1998, 14, 17-30.

[3] (a) Turkevich J.; Hillier, J.; Stevenson, P.C. Discuss. Faraday Soc. 1951, 11, 55-74. (b) Turkevich, J. Gold Bull. 1985, 18, 125-131. (b) Templeton, A.C.; Wuelfing, W.P.; Murray, R.W. Acc. Chem. Res. 2000, 33, 27-36.

[4] (a) Turkvich, J. Gold Bull. 1985, 18, 86-91. (b) Turkevich, J. Gold Bull. 1985, 18, 125-131.

[5] (a) Elghanian, R.; Storhoff, J.J.; Mucic, R.C.; Letsinger, R.L.; Mirkin, C.A. Science 1997, 277, 1078-1081. (b) Pissuwan, D.; Cortie, C.H.; Calenzuela, S.M.; Cortie, M.B. Gold Bulletin 2007, 40, 121-130. (c) He, W.; Huang, C.Z.; Li, Y.F.; Xie, J.P.; Yang, R.G.; Zhou, P.F.; Wang, J. Anal. Chem. 2008, 80, 8434-8430.

[6] http://www.britishbiocell.co.uk/

[7] (a) Sperling, R.A.; Gil, P.R.; Zhang, F.; Zanella, M.; Parak, W.J. Chem. Soc. Rev. 2008, 37, 1896-1908. (b) Wilson, R. Chem. Soc. Rev. 2008, 37, 2028-2045.

[8] Zhao, W.; Brook, M.A.; Li, Y. ChemBioChem 2008, 9, 2363-2371.

[9] Chapman, A.P. Adv. Drug Delivery Rev. 2002, 54, 531-545.

[10] (a) Miyamoto, D.; Ioshi, M.; Kojima, K.; Yoshimoto, K.; Nagasaki, Y. Langmuir 2008, 24, 5010-5017. (b) Eck, W.; Craig, G.; Sigdel, A.; Ritter, Gerd, Old, L.J.; Tang, L.; Brennan, M.F.; Allen, P.J.; Mason, M.D. ACS Nano 2008, , 2, 1639-1644.

[11] (a) Link, S.; El-Sayed, M.A. J. Phys. Chem. B 1999, 103, 4212-4217. (b) Link, S.; El-Sayed, M.A. J. Phys. Chem. B 1999, 103, 8410.

[12] (a) Du, B.-A.; Li, Z.-P.; Liu, C.-H. Angew. Chem. Int. Ed. 2006, 45, 8022-8025. (b) Jiang, Z.; Sun, S.; Liang, A.; Huang, W.; Qin, A. Clin. Chem. 2006, 52, 1389-1394. (c) Xie, H.; Gill-Sharp, K.L.; O'Neal, D.P. Nanomedicine: Nanotech. Bio., Medi. 2007, 3. 89-94.

[13] (a) Ishii, T.; Ostuka, H.; Kataoka, K.; Nagasaki, Y. Langmuir 2004, 20, 561-564. (b) Takae, S.; Akiyama, Y.; Ostuka, H.; Nakamura, T.; Nagasaki, Y.; Kataoka, K. BIomarcromolecules 2005, 6, 818-824. (c) Jang, Z.; Sun, S.; Liang, A.; Huang, W.; Qin, A. Clin. Chem. 2006, 52, 1389-1394. (d) Niidome, T.; Yamagata, M.; Akiyama, Y.; Takahashi, H.; Kawano, T.; Katayama, Y.; Niidome, Y. J. Controlled Release 2006, 114, 343-347. (e) Pissuwan, D. Valenzuela, S.M.; Cortie, M.B. Trends in Biotech. 2006, 24, 62-67. (f) Storhoff, J.J.; Lucas, A.D.; Garimella, V.; Bao, Y.P.; Muller, U.R. Nat. Biotech. 2004, 22, 883-887. (g) Otsuka, H.; Nagasaki, Y.; kataoka, K. Adv. Drug Del. Rev. 2003, 55, 403-419.

[14] Sahab, Z.J.; Semaan, S.M.; Sang Q.-X.A. Biomarker Insights 2007, 2, 21-43.

[15] Diamandis, E.P.; Christopoulos, T.K. Immunoassay. San Diego: Academic Press, c1996.

CHAPTER 9. ENHANCED IMAGING AND ACCELERATED PHOTOTHERMALYSIS OF A540 HUMAN LUNG CANCER CELLS BY GOLD NANOSPHERES UNDER LASER IRRADIATION

9.1 Introduction

Since 1999, cancer has surpassed heart disease and become the number one cause of mortality for people younger than 85 years old in US.[1, 2] In 2008, it is estimated that 1.2 million people will be diagnosed with cancer. By far, lung and bronchus cancer represents about 29% of all cancer cases, and lung cancer has the highest death rate among cancer patients in both men (31%) and women (26%).[3] The early detection and effective treatment of lung cancer has remained as a significant challenge. New imaging techniques and therapeutic methods/agents, including nanomaterials and nanotechnology, are being explored extensively for cancer study and treatment.[4-10]

GNPs, including nanospheres, nanorods and nanoshells with a size ranging from 1 to 100 nanometers, are known to have large light absorption and scattering cross sections in the surface plasmon resonance (SPR) wavelength region.[11] The light absorption and scattering cross sections around the SPR band of a gold nanoparticle can be a few orders of magnitude higher than the fluorescence emission of traditional organic dyes. The strong absorption of GNPs, and nanoparticle aggregation-induced SPR wavelength shift, has been studied extensively for biosensor and immunoassay applications.[12,13] As a strong light scatterer, GNPs are being used effectively for optoacoustic imaging and dark field imaging of biological cells.[14, 15] Recently, the light scattering property of GNPs has been reported for the development of a homogeneous immunoassay using dynamic light scattering (DLS).[16] In addition to elastic scattering, inelastic scattering such as surface-

enhanced Raman scattering is another area of strong interest.[13,17] Relatively large GNPs with a diameter above 10 nm, are not photo luminescent. Therefore, GNPs are excellent photothermal energy converters and have been explored for photothermal therapy of tumor cells and for controlled destruction of bacteria and protein aggregates.[18-21] The dual function of GNPs, namely, the strong light scattering property for dark field optical imaging and the highly efficient photothermal energy conversion for photothermalysis of cancer cells, make GNPs particularly attractive for cancer research.

In this study, we investigated the use of a gold nanoparticle probe for optical imaging and accelerated photothermalysis of the human lung cancer cell A549. A549 cells are derived from lung carcinoma with properties of type II alveolar epithelial cells, and may serve as well established cell model in the studies of lung cancer biomarkers.[21,22] GNPs used in this study were conjugated with a layer of anti-human IgG on the surface. After incubating the cells with the GNPs, the loading of GNPs by tumor cells was imaged using a dark field optical microscope. The photothermalysis of tumor cells with and without the loading of GNPs was studied using a viability test kit under a confocal microscope.

9.2 Materials and Methods

9.2.1 GNPs and characterizations

Goat anti-human IgG conjugated GNPs (Prod # 15775D-4G) were purchased from Ted Pella (Redding, CA). The nanoparticle concentration was adjusted to 5 fM in a pH=7.4 PBS saline solution (NaCl 0.138 M; KCl 0.0027 M) by the vendor. High resolution transmission electron microscopic study (HRTEM) of the nanoparticles was conducted on a FEI Tecnai F30 TEM (FEI Company) at an acceleration voltage of 200

keV. Samples for HRTEM analysis were prepared by pipeting 5 uL of sample solution to the surface of a poly-L-lysine (0.0381 g/mL in 1:3 H_2O:MeOH mixture solvent) treated 400 mesh carbon/formvar coated copper grid. Following vacuum drying for 30 min, the grid was placed in a desiccator at room temperature for at least overnight before conducting HRTEM analysis. A Cary 300 Bio UV-Visible spectrophotometer from Varian Inc. (Palo Alto, CA) was used for UV-Vis spectroscopic study. A PD2000DLS^{PLUS} Dynamic Light Scattering Detector and a PDDLS/CoolBatch 40T Dynamic Light Scattering detector system from Precision Detectors Inc. (Bellingham, MA) were used for the particle size measurement. The DLS instrument was operated under the following conditions: temperature 20^{o}C, detector angle 90^{o}, incident laser wavelength 683 nm, laser power 100 mW. The DLS data was processed using the Precision Deconvolve software. Samples for DLS analysis were diluted in 1.50 mL nanopure water to appropriate concentrations, mixed well and stabilized before measurement.[16]

9.2.2 Cell line culture

A549 (ATCC. No. CCL-185) human lung cancer cell line, derived from adenocarcinoma of the male lung, was cultured in a Roswell Park Memorial Institute (RPMI) media with 10% Fetal Bovine Serum, 1% L-Glutamine, 1% Hepes, and 1% penicillin-streptomycin. All cultures were maintained in humidified incubators at 37 °C in an atmosphere of 5.0% CO_2. 24 Hours prior to laser irradiation treatments, the cells were plated on round cover slips (Bioptechs, 40 mm, Butler, PA) in culture plates (60 mm × 15 mm Fisherbrand, Pittsburgh, PA) and treated with GNPs for each treatment regimen. The controls were untreated A549 cells, incubated in culture media without

GNPs. The cell concentration was 10 million cells per ml of the media for all cell study experiments. In the regimen with gold nanoparticle treatment, A549 cells were incubated in the same amount of culture media as the controls, with the addition of GNPs to a final concentration of 0.25 pM. The plated cells were incubated in humidified incubators at 37 °C in atmosphere of 5.0% CO_2 for 24 hours.

9.2.3 Dark field imaging

The cells on plates were washed with PBS saline 5 times and dried in ambient condition before being mounted on a glass slide. Dark field images were obtained using an Olympus U-DCW condenser and an UPlanFL N 100x/1.30 oil iris with an Olympus BX51 microscope. All dark field images were taken by the Analysis Imager 5.0 software at the exactly same imaging conditions (incident light intensity, gain, exposure time, etc.).

9.2.4 Laser irradiation condition and viability assay

A549 cells, after being exposed in the cell culture with GNPs for 24 hours, were stained using a Violet Live/Dead Viability Fixable Assay Kit (Invitrogen, Carlsbad, CA Cat# 34955) for half an hour. According to the protocol, 1 uL of dilutant with violet dye was added to 1 mL of media in plates containing cover slips seeded with live cells and incubated for 30 minutes. Cover slips with cells on them were transferred to a Live Cell Microscopy Environmental Control System from Bioptechs (Butler PA). Viability tests for both control cells and samples cells after gold nanoparticle exposure were monitored with a DMI6000 inverted Leica TCS AOBS SP5 tandem scanning confocal microscope with a 63x/1.40NA oil immersion objective. A 52.5 mW 405 nm diode laser (Lasos, San Jose, CA) tuned to a 1% output power (0.525 mW) was used to excite the violet viability stain, and the fluorescence emission at 450 nm was collected. A Helium-Neon 5 mW

diode laser at 633 nm (Lasos, San Jose, CA) (1.0 W/cm^2) was used for irradiation of the cells. Images, Z-stacks and time lapse experiments were performed with dual photomultiplier detectors and the LAS AF version 1.5.1.889 software suite. Cell death was assessed in real time by imaging the cells constantly at a 400Hz rate of one 1024x1024 frame, which refreshes a newly scanned image every 5.179 seconds for the length of the time lapse. Images over time were converted to .avi files for ease of comparison and viewing. Image Pro Plus V6.2.0 (Media Cybernetics, Bethesda, MD) was used to quantify the intensity of individual cells in every fifth frame of the time lapse. Total cellular intensity was determined by the average of dynamic range values for each pixel within individual cells. Viability tests for both control and sample cells were studied at different power levels of 633 nm laser (0.50 mW, 1.25 mW, 2.50 mW, 3.75 mW and 5.00 mW).

9.2.5 Relative viability drop curves and normalized relative viability drop rate curves

Relative viability of cells at each imaging time was computed as the relative percentage of fluorescence intensity at specified irradiation time over the initial fluorescence intensity by the Microsoft® Office EXCEL 2003 SP3 and the OriginPro SR1 v7.5776 (B776) software. Relative viability drop curves for both control cells and sample cells after gold nanoparticle exposure were plotted along the irradiation time of 633 nm laser. For each different power level irradiation, the corresponding curve was established. The relative viability drop curves at 0 mW for both control cells and samples cells were taken as baselines for the following calculations of normalized viability drop rate curves, respectively. The relative viability drop rate curves were constructed by

calculating the slopes of each relative viability drop at corresponding irradiation time and plotted over irradiation time up to 58 seconds. The normalized viability drop rate curves were obtained after subtracting corresponding baselines, for control cells and sample cells after gold nanoparticle exposure, respectively.

9.3 Results and Discussions

In this work, gold nanospheres were chosen for the dark field imaging and photothermalysis study of cancer cells. Compared to many other types of nanoparticles such as quantum dots, gold nanorods and nanoshells etc., gold nanospheres are more stable, easy to make, and have low cytotoxicity.[10,17,18] Although the SPR of individual gold nanospheres is in the visible light region, 520-530 nm, this band can red-shift to near infrared region upon nanoparticle aggregation. Spherical GNPs therefore are still very attractive optical probes for cell imaging and photothermalysis study.[22,23] Gold nanospheres with a core diameter of 40 nm were chosen for this study. This size was previously reported as the optimum size for photothermalysis of cancer cells.[23,25] The gold nanospheres were prepared by coating a layer of goat anti-human IgG antibody on the surface of a citrate-protected gold nanoparticle (from the Vendor's product information). The citrate-protected gold nanospheres are not stable in high salt content buffer solutions such as cell culture media, and quickly precipitate out of the solution at salt concentration above 30 mM. The anti-human IgG layer makes the nanospheres stable in the cell culture media. Furthermore, the anti-human IgG from the nanoparticles can bind with the human IgG molecules on the surface or inside the tumor cells, allowing gold nanospheres to be loaded to the lung tumor cells.

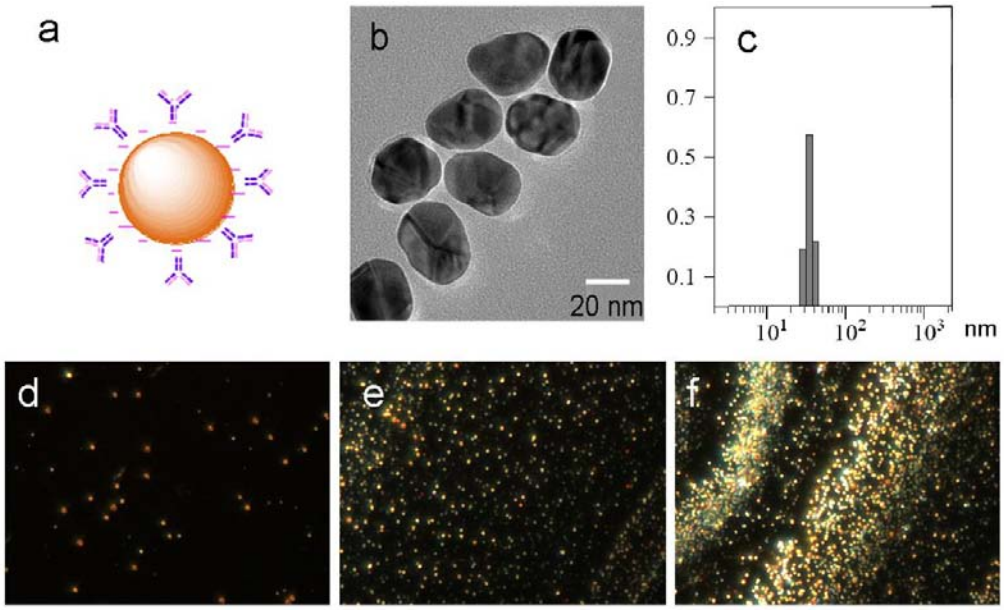

Figure 9- 1. Goat anti-human IgG conjugated gold nanospheres and their dark field images. (A) Schematic illustration, (B) HRTEM micrograph, (C) size and size distribution measured by DLS, (D)-(F) dark field images at incremental concentrations from 1, 10 to 100 fM, respectively. (Copyright ® 2008 Future Medicine Ltd.)

A HRTEM image and UV-Vis absorption spectrum of gold nanoparticle conjugates are shown in Figure 9-1 and Figure 9-2, respectively. The gold nanospheres exhibit an SPR band centered at 530 nm. DLS measurement confirmed the narrow size distribution of gold nanospheres used in the study (Figure 9-1c). The gold nanoparticle solution was drop cast on a glass slide and then visualized under a dark field optical microscope. The micrographs revealed bright nanoparticle dots on the glass slide.[16] With increased nanoparticle concentration, from Figure 9-1d to f, the number and the scattering intensity of gold nanospheres increased significantly due to nanoparticle aggregation.

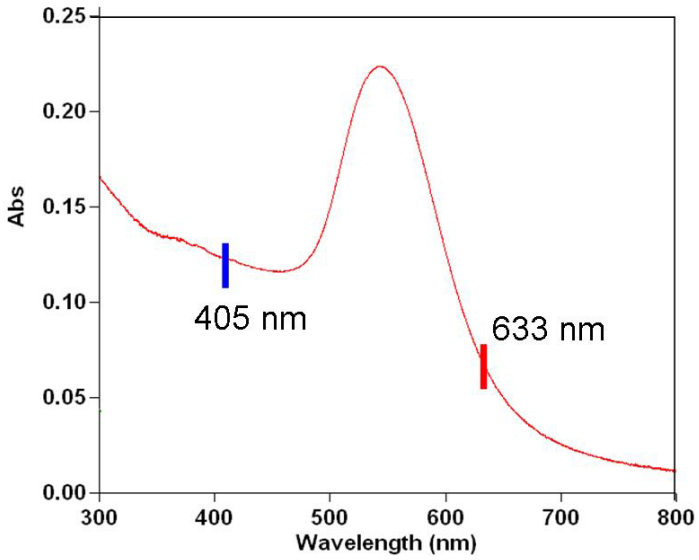

Figure 9- 2. UV-Vis spectrum of well dispersed gold nanoparticle probes. UV-Vis spectrum of 40 nm goat anti-human IgG conjugated gold nanospheres with a SPR band peaked at 530 nm (irradiation laser wavelength at 633 nm, imaging laser wavelength at 405 nm). (Copyright ® 2008 Future Medicine Ltd.)

Dark field optical microscopy was then used to examine the loading of gold nanospheres by cancer cells. Without incubation with gold nanospheres, it was found that the cancer cells were weak light scatterers and could be visualized under the dark field microscope (Figure 9-3a-c). However, the contrast of the images was rather poor. After incubation with gold nanospheres in the cell culture media, the contrast of the images was enhanced significantly when compared with images of cancer cells that were not exposed to gold nanospheres in the cell culture media (Figure 9-3d-f). It needs to be noted here that all images were taken under exactly the same conditions including incident light intensity, gain, exposure time, etc. This enhancement effect is a strong indication of an effective loading of gold nanospheres to the cancer cells. From these dark field images, it is not discernable whether the gold nanospheres were mainly located on the surface or inside the tumor cells. However, previous reports support that nanospheres are mainly

located on the cell surface, with a small amount found inside the cells through endocytosis.[8,25] Because the gold nanospheres used in this study are coated with a layer of anti-human IgG on the particle surface, gold nanospheres can be effectively loaded to the tumor cells. The dark field images revealed that the uptake of gold nanospheres by the nuclei was none or extremely low.

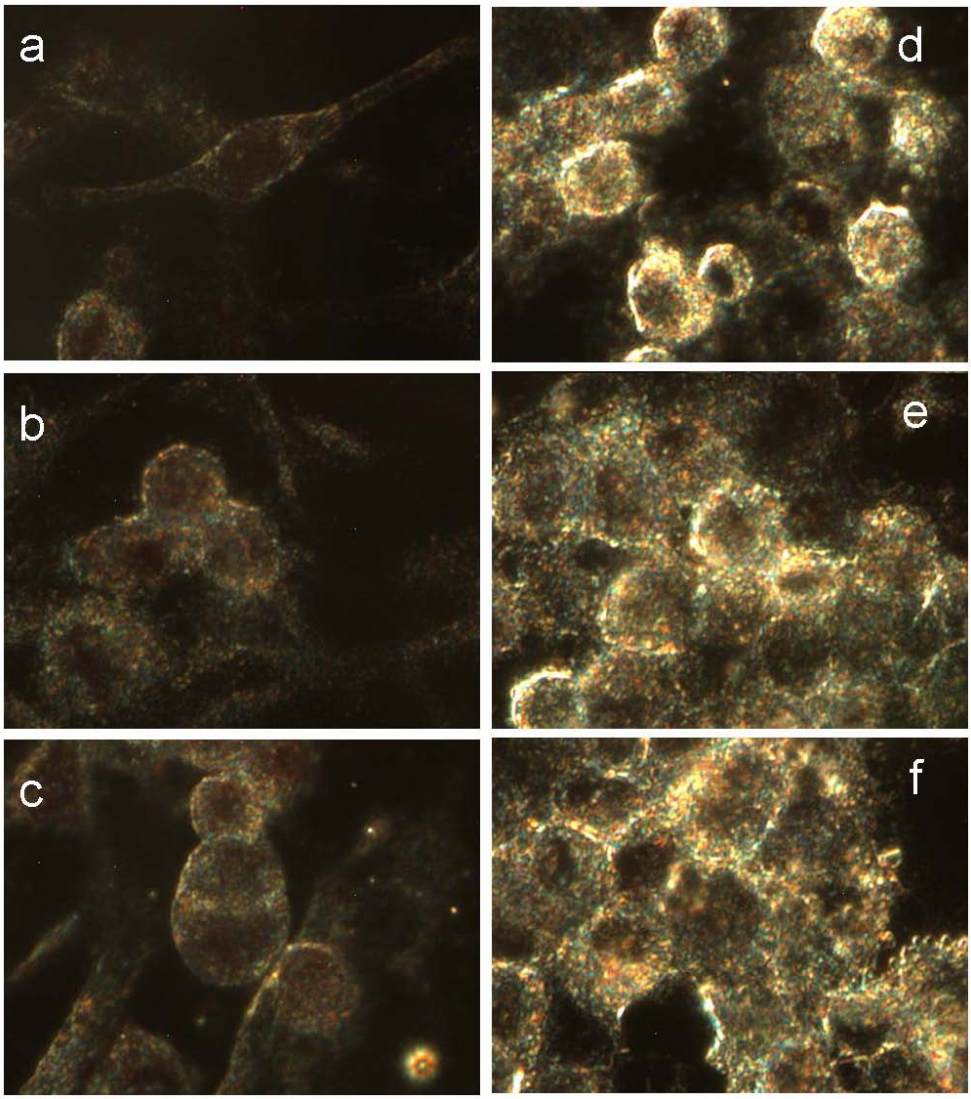

Figure 9- 3. Dark field images of lung tumor cell A549 without (a-c) and with (d-f) gold nanospheres loaded to the cells. All images were obtained using exactly the same imaging setup. The final concentration of gold nanospheres added to the lung tumor cell culture was 0.25 pM for all three samples. (Copyright ® 2008 Future Medicine Ltd.)

After verifying the effective loading of gold nanospheres by the A549 lung cancer cells, confocal microscopy was used to study the photothermalysis of cancer cells under the irradiation of a 5 mW 633 nm laser beam. The power of the laser was adjusted from 0 to 0.5, 1.25, 2.5, 3.75 and 5 mW to optimize the photothermalysis condition, respectively. The viability drop of cells upon laser irradiation was monitored by a Violet Live/Dead Viability Fixable Assay Kit with a 0.5 mW 405 nm laser for fluorescence excitation and followed by emission detection at 450 nm. The assay used a fluorescent dye that is reactive towards cellular amines. The dye can binds only to the surface amines of viable cells, but react with free amines in both interior and cell surface of necrotic cells (product description). When cell membrane destruction occurs, the accumulated dyes on the cellular membrane will be dissociated and consequently result in a decrease of fluorescence intensity on cell membrane. The decrease of fluorescence intensity, which was monitored by imaging at each 5.179 seconds interval for up to 58 seconds, was interpreted and assessed as the viability drop of cells in this study. Fluorescence emission intensity information from such obtained images were extracted and plotted versus irradiation time to give the relative viability drop curves.

As revealed from the UV-Vis spectrum of the gold nanospheres solution (Figure 9-2), gold nanospheres exhibited SPR band peaked around 530 nm and absorptions at both 405 nm and 633 nm. During our initial study, it was found that a significant interference to cell viability was arisen from the irradiation of the imaging laser (405 nm). Therefore, the imaging laser was operated at a significantly decreased power level (0.525 mW). The viability drop curves for both control cells and nanoparticle-loaded cancer cells caused by imaging laser irradiation at 405 nm were used as baselines and

subtracted from viability drop curves under the 633 nm laser irradiations respectively to give the normalized relative viability drop curves. Normalized relative viability drop rates of cancer cells were then calculated according to the slopes of the normalized relative viability drop curves.

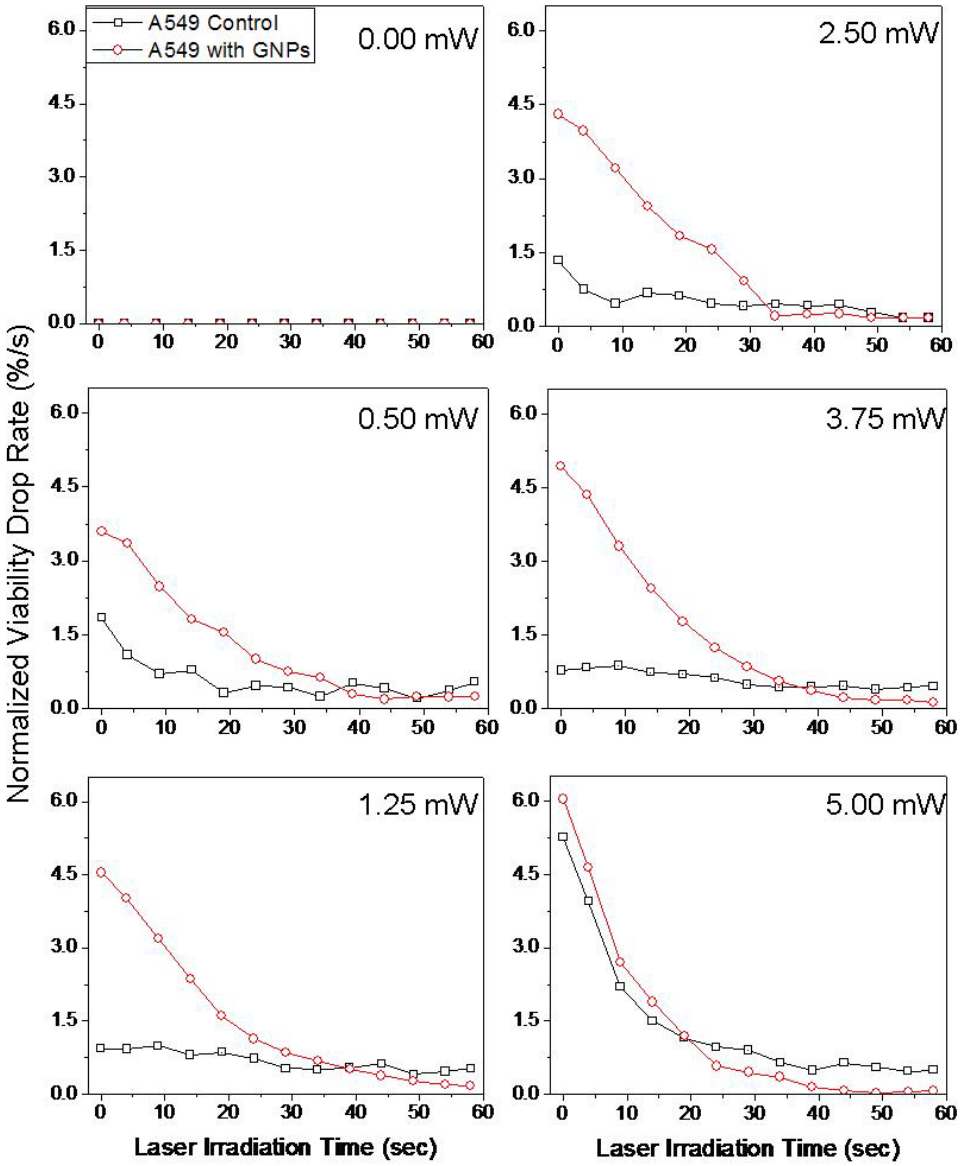

Figure 9- 4. Effect of 633 nm laser irradiation on A549 tumor cells at different power levels. Normalized relative viability drop rate of lung A549 cells during the irradiation (square: control cells without gold nanopsphere incubation; circle: sample cells with gold nanosphere incubation) (Copyright ® 2008 Future Medicine Ltd.)

Although nanoparticle-enhanced photothermalysis effects for tumor cells were reported previously, the kinetic characteristic behavior of the viability changes during irradiation has not been examined closely.[6-8,18] In this study, a real time monitoring of cancer cell viability was performed. In Figure 9-4, normalized relative viability drop rates versus irradiation time were summarized for both control cells and nanosphere-loaded cells at different laser power levels. For control cells (black curves), the laser irradiation at 633 nm caused a roughly constant small viability drop rate around 0.75 %/s during the whole 58 seconds irradiation period for power levels from 0.5 mW to 3.75 mW. The small viability drop rate was most probably coming from the photobleaching effect of viability dyes under the 633 nm laser irradiation. At the power level of 5 mW, a large viability drop rate was observed for control cells. This large viability drop rate could due to an enhanced photobleaching of the viability dyes by 633 nm laser irradiation, or from laser induced photothermalysis of cells. For gold nanosphere-loaded A549 cancer cells, viability drop rates (red curves) were significantly higher than the rates of control cells, especially within the first 30 seconds of irradiation. The initial relative viability drop rates at zero seconds were observed to increase from 3.72 %/s to the maximum of 5.00 %/s when the power of the laser was increased from 0.5 to 3.75 mW. In contrast, the relative viability drop rates of control cells remained at ~0.75 %/s for power levels from 0.5 mW to 3.75 mW. The photothermalysis of gold nanosphere-loaded cancer cells was accelerated significantly due to the enhancement effect of gold nanospheres. Comparing the relative viability drop rates for both control and nanospheres-loaded cells at different power levels, the optimum power level for gold nanospheres accelerated photothermalysis of A549 human cancer cells was found to be 3.75 mW, at which level

the initial relative viability drop rate was 5.00 %/s for nanoparticle-loaded cells and only 0.75 %/s for control cells. At this power level, the initial relative viability drop rate of nanosphere-loaded tumor cells was accelerated by a factor of 6.6.

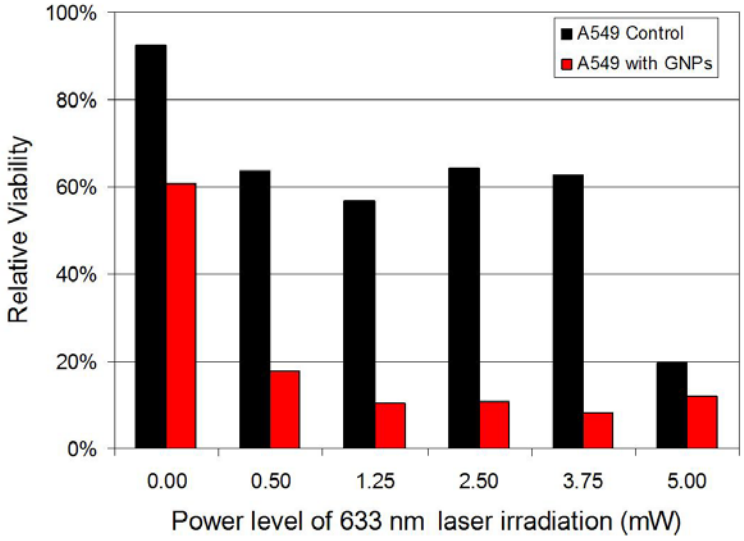

Figure 9- 5. Viability drop of tumor cells after irradiation for 58 seconds using a 633 nm continuous wave laser under different power levels. (Copyright ® 2008 Future Medicine Ltd.)

After irradiation by the 633 nm laser for 58 seconds, the accumulated relative viability drops at different power levels for both control cells and gold nanospheres-loaded cells are presented in Figure 9-5. The nanospheres-induced hyperthermia effect and thus the accumulated destruction effect on cancer cells can be verified by comparing the viabilities of control cells and sample cells. The relative viabilities of nanospheres-loaded cells dropped to be around ~8-18% after irradiation for 58 seconds at laser power between 0.5-3.75 mW, while the viabilities of control cells remained at 60% or above after equivalent dose of irradiation. A minimum viability of 8% was observed from nanosphere-loaded cells after irradiation at a laser power of 3.75 mW.

Upon closer examination, it is noticed that at zero power of the irradiation laser (633 nm), the viability of nanospheres-loaded cells decreased to 60% while the control cells remained almost intact. It is believed that this difference is due to the nanosphere-accelerated photothermalysis of tumor cells under the irradiation of imaging laser at 405 nm. Although the maximum absorption of the SPR of gold nanospheres is centered at 520-530 nm, the nanospheres exhibit significant absorption at 405 nm as well, as revealed from the UV-Vis spectrum of 40 nm gold nanospheres in Figure 9-2. This absorption caused the accelerated death rate of the nanosphere-loaded cells.

When the power level of the irradiation laser was increased to 5 mW, it was found that the relative viability drop rate was almost the same for control and nanoparticle-loaded cells (Figure 9-4). At this power level, the viability of control cells decreased to 20%, close to what was observed from the nanosphere-loaded cells, 12% (Figure 9-5). Two possible reasons may account for the observed large viability drop of the control sample: one possibility is that the relatively high power of the 633 nm laser irradiation induced a significant photobleaching to the fluorescence dye used for viability study, which makes the cells appear to be dead. On the other hand, it is also possible that under high power laser irradiation, photothermalysis of control cells has occurred. For photothemal therapy, it is important to use a laser with a power level as low as possible to avoid unexpected damages to healthy and normal tissues and cells. Based on our current study, it can be seen that the photothemalysis of nanosphere-loaded tumor cells has reached its maximum effect with a laser power level between 1.25-3.75 mW. There is no need to further increase the power of the irradiation laser to beyond 3.75 mW. Our conclusion is that by carefully controlling the power of the laser during photoirradiation,

it is possible to selectively increase the photothermalysis of gold nanoparticle-loaded tumor cells while minimize the photothermalysis of normal cells without or with less nanospheres.

The mechanism of gold nanosphere-accelerated photothermalysis of tumor cells was reported to start from the photon energy absorption from laser beam irradiation by gold nanospheres and their aggregates.[23, 26] The conversion of the photon energy to thermal energy by gold nanospheres and their clusters introduced a hyperthermia effect around the local cell membrane. This effect resulted in the formation of micrometer sized cavities on the cell membrane. A recent study revealed that extracellular calcium cations played a critical role in cavity formation during gold nanorods-assisted photothermalysis of tumor cells.[10] The growing of these cavities was found to be the main cause for lysis of cells, besides the hyperthermia effect. For individual gold nanospheres, irradiation at the SPR band peak wavelength should have the highest photothermal conversion efficiency. In this study, the wavelength of laser irradiation beam for viability tests was at 633 nm instead of 530 nm. However, the accelerated photothermalysis of A549 tumor cells by gold nanospheres was still significant. We believe this effect is a result of the formation of nanosphere aggregates around the cell membranes, as supported by the dark field imaging study. Upon aggregation, the SPR band of nanoparticles can red-shift significantly to higher wavelength.[23,24]

9.4 Conclusion

In conclusion, 40 nm gold nanospheres were used to accelerate the cell death of A549 human lung cancer cells by laser irradiation at 633 nm. The loading of gold nanospheres to tumor cells on cell membrane and partial internalization was observed

under a dark field optical microscope. Viability tests of tumor cells under the irradiation of a 633 nm laser showed that gold nanospheres could significantly accelerate the cell death rates of tumor cells up to a factor of 6.6 compared to control cells. The kinetic characteristics of the viability drop of tumor cells caused by gold nanoparticle-enhanced photothermalysis were examined closely. The optimized laser power for photothermalysis of A549 human cancer cells was found to be 1.25-3.75 mW. After 58 seconds of irradiation, the viability of gold nanoparticle-loaded tumor cells decreased to only 8% of their original viability, while the majority of control cells were still alive.

We demonstrated here a potential application of gold nanospheres for the imaging and treatment of human lung cancer cells. The stability and surface functionality of gold nanospheres used in this study make them as suitable candidates for future *in vivo* investigations. The strong scattering property of gold nanospheres enables their use as optical probes for dark field microscopy imaging of tumor cells with much improved contrast. Compared to fluorescence probes, the light scattering of GNPs are not subjected to photobleaching and many other interfering factors. The strong absorption properties of nanospheres and aggregated clusters can significantly accelerate the photothermalysis of tumor cells upon laser irradiation. Our next step is to prepare gold nanosphere-antibody conjugates which can specifically target the A549 lung cancer cells and further increase the efficiency and specificity of the photothermal therapy process. The ultimate goal of this research is the development of a dual imaging/therapy method which can allow a one-step imaging and eradication of lung tumor tissue through photoirradiation using a single laser source with adjustable power.

References:

1 Jemal, A.J.; Murray, T.; Ward, E.; Samuels, A.; Tiwari, R.C.;, Ghafoor, A. Cancer Statistics, 2005. CA Cancer. J. Clin. 2005, 55, 10-30.

2 Kawasaki, E.S.; Player, A. Nanomedicine: Nanotechnology, Biology, and Medicine 2005, 1, 101-109.

3 Jemal, A.; Siegel, R.; Ward, E. Cancer Statistics, 2008. CA Cancer J. Clin 2008, 58, 71-96.

4 Han, M.; Gao, X.; Su, J.Z.; Nie, S. Nat. Biotech. 2001, 19, 631-635.

5 Hirsch, L.R.; Stafford, R.J.; Bankson, J.A. Proc. Natl. Acad. Sci. USA 2003, 100, 13549-13554.

6 O'Neal, D.P.; Hirsch, L.R.; Halas, N.J.; Payne, J.D.; West, J.L. Cancer Lett. 2004, 209,171-176.

7 Kukowska-Latallo, J.F.; Candido, K.A.; Cao, Z. Cancer Res. 2005, 65, 5317-5324.

8 Huang, X.; El-Sayed, I.H.; Qian, W.; El-Sayed, M.A. J. Am. Chem. Soc. 2006, 128, 2115-2120.

9 Shi, X.; Wang, S.; Meshinchi, S. Small 2007, 3, 1245-1252.

10 Tong, L.; Zhao, Y.; Huff, T.B.; Hansen, M.N.; Wei, A.; Cheng, J.X. Adv. Mater. 2007, 19, 3136-3141.

11 Danieal, M.C.; Astruc, D. Chem. Rev. 2004, 104, 293-346.

12 Park, S.J.; Taton, T.A.; Mirkin, C.A. Science 2002, 295, 1503-1506.

13 Qian, X.; Peng, X.H.; Ansari, D.O. Nat. Nanotech. 2008, 26, 83-90.

14 Mallidi, S.; Larson, T.; Aaron, J.; Sokolov, K.; Emelianov, S. Optics Express 2007, 15, 6583-6588.

15 Skrabalak, S.E.; Au, L.; Lu, X.; Li, X.; Xia, Y. Nanomedicine 2007, 2, 657-668.

16 Liu, X.; Dai, Q.; Austin, L. J. Am. Chem. Soc. 2008, 130, 2780-2782.

17 Qian, X.; Peng, X.H.; Ansari, D.O.; Yin-Goen, Q.; Chen, G.Z.; Shin, D.M. Nat. Biotech. 2007, 26, 83-90.

18 Letfullin, R.R.; Joenathan, C.; George, T.F.; Zharov, V.P. Nanomedicine 2006, 1, 473-480.

19 Pissuwan, D.; Cortie, C.H.; Valenzuela, S.M.; Cortie, M.B. Gold Bulletin 2007, 40,121-129.

20 Niidome, T.; Yamagate, M.;, Okamoto, Y. J. Control Release 2006, 114, 343-347.

21 Lieber, M.; Smith, B.; Szakal, A.; Nelson-Rees, W.; Todaro, G. Int. J. Cancer 1976, 17, 62-70.

22 Zajac, A.; Song, D.S.; Qian, W.; Zhukov, T.A. Colloids and Surfaces B: Biointerfaces 2007, 58, 309-314.

23 Zharov, V.P.; Galitovskaya, E.N.; Johnson, C.; Kelly, T. Lasers in Surgery and Medicine 2005, 37, 219-226.

24 Huang, X.; Qian, W.; El-Sayed, I.H.; El-Sayed, M.A. Lasers in surgery and medicine 2007, 39, 747-753.

25 Popov, A.P.; Priezzev, A.V.; Myllyla, R. Proc. of SPIE 2007, 6534, 65343K.

26 Lapotko, D.O. Lasers in Surgery and Medicine 2006, 38, 240-248.